LA-13695-MS

Issued: May 2000

Computer-Optimized Design of Polyethylene-Moderated ^{3}He Counters for Fast Neutrons

R. C. Byrd

Los Alamos
NATIONAL LABORATORY
Los Alamos, New Mexico 87545

DISCLAIMER

CONTENTS

COMPUTER-OPTIMIZED DESIGN OF POLYETHYLENE-MODERATED ^{3}He COUNTERS FOR FAST NEUTRONS

by

R. C. Byrd

ABSTRACT

Because polyethylene-moderated ^{3}He counters are rugged and reliable, they are generally the instruments of choice for field detection of fast neutrons in gamma-ray backgrounds. Their main drawback is the bulky, massive moderator needed to reduce the incident neutron energies to the sensitive range of the ^{3}He+n capture reaction. This report discusses an optimization approach that provides a detector with uniform angular response and the maximum detection efficiency per unit mass. The key assumption is that each parameter has a geometrical interpretation and its effect on the response can be evaluated independently from that of the others. Specifically, the detection efficiency can be written as a product of separate functions for the moderator mass, gas pressure, tube position, etc., and the uniformity of the angular response is determined by the symmetry of the moderator dimensions. This analytical model was tested by compiling a comprehensive database of detector efficiencies as functions of the different parameters, including one- versus two-tube detectors, moderator masses from 1 to 6 kg, gas pressures from 1 to 20 atm, etc. In general, the model reproduced both the magnitude and angular dependence of the efficiency to within about 10%. To a high degree, the most important parameters are polyethylene mass and the quantity of ^{3}He gas; because of neutron diffusion out of the moderator, the optimum tube positions are near the center of the detector. The highest value of the efficiency per unit mass occurs near 3 kg, a result that requires the most compact detectors to use more than a single ^{3}He tube. In our case, the optimum detector has two tubes and a total mass of 3.0 kg. Although we use 4-atm tubes with 2.54-cm diameters, increasing the gas volume could easily provide a 20% increase in efficiency with no changes in other parameters.

---

1. OBJECTIVES

Problem Statement. Neutron detectors for field measurements must meet two almost contradictory requirements: they must be reliable, and they must be lightweight. Because

neutrons are uncharged and therefore not directly observable, all neutron detectors must use a conversion process to transform the unobservable radiation field into a measurable charged-particle signal. One class of detectors uses plastic scintillators, which convert the recoil energy of the protons produced in n-p elastic scattering into detectable light output. Although such scintillators might seem to be the logical choice for detecting neutrons at MeV-range energies, they have the serious disadvantage of a gamma-ray sensitivity that often exceeds their neutron response. At modest count rates this problem can be overcome by pulse-shape discrimination, but such techniques are usually regarded as too complex for field use. In contrast, the other major class of detectors uses low-energy neutron-capture reactions on ^{3}He, ^{7}Li, or ^{10}B, whose outgoing charged particles produce a detectable signal in standard ionization detectors. Because these capture reactions have high Q values, the resulting output pulses are usually large compared with those for the electrons from gamma-ray interactions, which allows a simple pulse-height threshold to provide excellent gamma-ray rejection. The major drawback of capture reactions is their low cross section at high neutron energies, which requires the use of heavy and bulky hydrogenous moderators in order to reduce the neutron energies to the more sensitive range at low energies. In general, any attempt to reduce the detector mass also reduces the detection efficiency, but the tradeoff may not be directly proportional, especially when variations in other parameters are considered. A major goal of this report is to explore this relationship in order to determine the maximum detection efficiency per unit mass. This optimization is obviously important for field instruments such as the ground-based, man-portable detectors used in health physics or arms control, although our literature survey located few examples of such efforts.[1,2,3] Relatively few parameters were varied in those studies, so it is difficult to relate the results to other detector geometries. In particular, our area of interest is space-based instruments for treaty verification and planetary physics, where the size and weight constraints are especially severe. Accordingly, this report presents a comprehensive optimization study for one such instrument, a polyethylene-moderated ^{3}He detector, but the results should be appropriate for a wide range of similar neutron counters.

Contents. In Chap. 2 we review the results from two previous reports[4,5] that describe an existing space-based neutron detector system. Included are geometry descriptions and calculations of the energy and angle dependences of the neutron-detection efficiencies. The focus of these earlier reports was on determining the existing performance level and on increasing the efficiency by varying a few of the design parameters. In Chap. 3 we explain the basic techniques for the present calculations, which are arranged as complete energy- and angle-dependent surveys of the effects of all the important detector variables. These parameters include the moderator dimensions; the number, radius, and pressure of the counter tubes; and the location of tubes within the moderator. Because it is very difficult to separate the effects of so many parameters, in Chap. 4 we describe a model that represents the detection efficiency and its angular dependence as simple product and sum functions of the individual parameters. The results of this modeling are presented in two parts, in Chap. 5 for two-tube detectors that are similar to the existing design, and in Chap. 6 for a one-tube version that might be a simpler alternative. Chapter 7 summarizes the results for both versions of the detector and predicts the performance of a "generic" design that represents a wide range of moderated ^{3}He counters. Chapter 8 then shows how this design can be optimized to provide a candidate spaced-based detector, and Chap. 9 provides a summary of the entire report and some comments about the gamma-ray response of the final instrument.[6]

2. PREVIOUS WORK

Overview. The foundations for the analyses discussed in this report are laid out in two previous reports. First, Ref. 4 describes the characteristics of the existing space-based neutron detector and our basic Monte Carlo detector-modeling techniques. These initial modeling attempts included both (1) high-energy LCS calculations[7] for estimating the production of neutrons from cosmic-ray backgrounds and (2) low-energy MCNP calculations[8] for determining the existing instrument's neutron-detection efficiency. The application of these models is focused primarily on evaluations of measured and calculated detection efficiencies and the effect of variations in the detector geometry. The subsequent discussion in Ref. 5 summarizes the earlier results, corrects an error in the model geometry, and investigates the possibility of increasing the efficiency per unit mass at higher energies by changing the moderator material. As an introduction to the present discussion, the current chapter presents a brief summary of the important results from this earlier work.

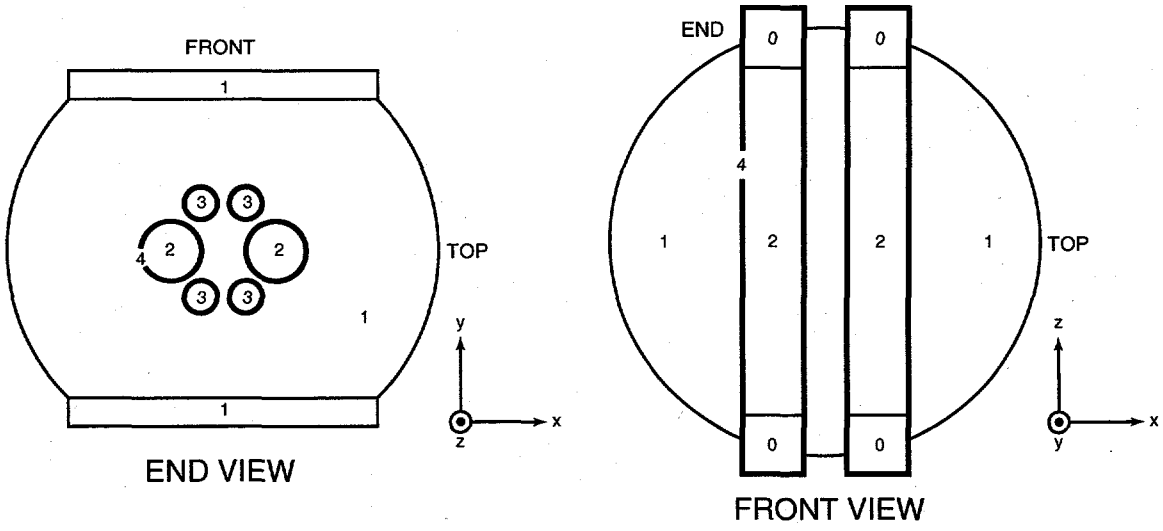

Figure 2.1. MCNP layout of the existing moderated ^{3}He counter.

2.1. Existing Instrument

Geometry. In **Figure 2.1** we show end and front views of the existing instrument[4,5] as generated by the MCNP plotting program. The small numbers refer to different materials: 1 is high-density polyethylene (ρ=0.96 g/cm^3); 2 is ^{3}He gas, 3 is BF_3 gas, and 4 is stainless steel. The gas pressures are all 4 atm, where 1 atm for ^{3}He at standard temperature and pressure (STP) is assumed to be 1.3×10^{-4} g/cm^3. As a scale for the figure, the diameter of the moderator sphere is 18.3 cm (7.2″), and the diameters of the counter tubes are 2.54 and 1.27 cm (1″ and 0.5″). The tube outputs are ganged together in pairs to provide redundancy, with the two large ^{3}He tubes providing the high-sensitivity channel and the two pairs of BF_3 tubes giving the medium- and low-sensitivity channels. To cover the necessary dynamic range, the low-range tubes also have reduced partial pressures and shorter lengths, 15.2 cm (6″) instead of 20.3 cm (8″). There are also 2.54-cm (1″) dead spaces at the ends of each tube, which are represented by voids in the original MCNP model. The inset axes in the figure show the coordinates used for the calculations, with the *x*-, *y*-, and *z*-axes corresponding to in-

cident neutron directions across, normal, and along the counter axes. As indicated in the figure, in the present calculations these orientations are referred to as the top, front, and end of the detector.

Efficiency Behavior. The geometry of the detector has a direct effect on the neutron-detection efficiency. In **Figure 2.2** we show the results of some of our first calculations,[4] which were made to normalize and interpolate within a set of existing measurements for a previous set of detectors. The three curves are detection efficiencies for polyethylene spheres with increasing radii, and the results are expressed in terms of the measured quantity, counts per source neutron. Because the purpose of the polyethylene is to slow down the incident neutrons in order to take advantage of the large low-energy ^{3}He capture cross section, adding moderator shifts the maximum efficiency toward higher energies. According to the figure, a detector optimized for MeV-range neutrons requires moderator dimensions consistent with our nominal detector diameter of 18.3 cm. These results are similar to the measurements and calculations shown in Ref. 9.

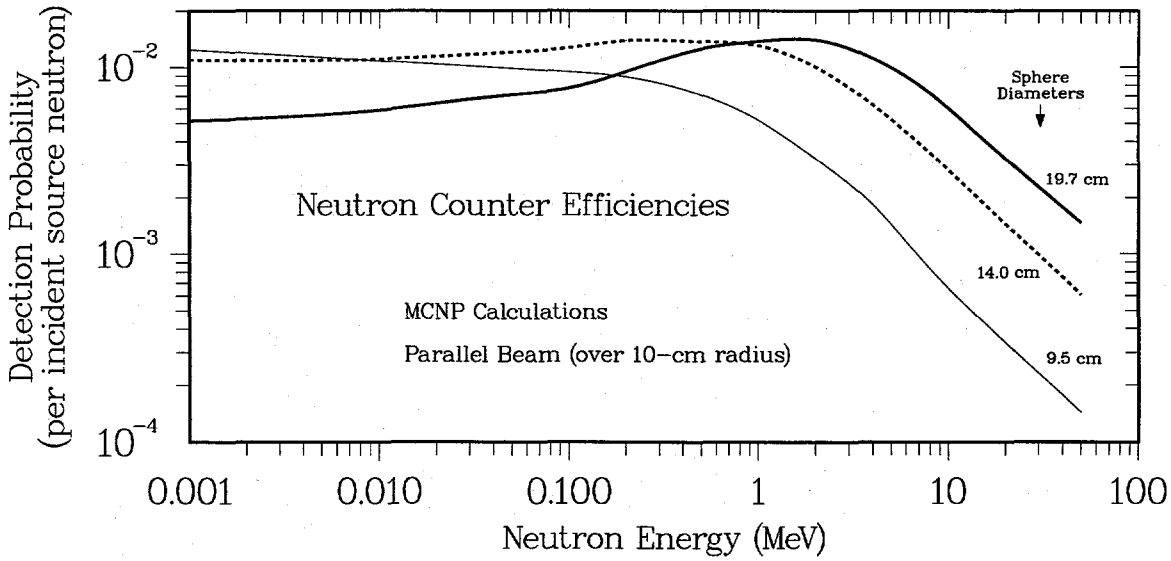

Figure 2.2. Calculations of the energy-dependent detection efficiency for polyethylene moderators of three different sizes.

2.2. Parameter Variations

Detector Modifications. Much of our previous work explores the possibility of varying the existing parameters in order to increase the detection efficiency. The results of the first study[4] are summarized in the next three figures. First, **Figure 2.3** shows the simplest example, a study of varying the gas pressure P for the high-sensitivity ^{3}He tubes. At the nominal 4-atm value, the efficiency for an incident parallel beam reaches about 7% at 1 MeV. Changes in pressure affect the magnitude but not the shape of the curve, although the rate of increase drops gradually with increasing pressure. A more detailed analysis[4] indicates that the overall efficiency scales approximately as $P^{1/4}$, that is, doubling the pressure gives an increase of about 20%. Next, **Figure 2.4** shows results from a more complicated study, which varies the amount of polyethylene moderator to provide a comparison with the results in Figure 2.2. As before, decreasing the moderation reduces the attenuation and improves the low-energy efficiency, but the high-energy efficiency

decreases rapidly. Note, however, that reducing the moderator also reduces the detector mass, an offsetting advantage not included in the analysis. Finally, **Figure 2.5** shows the effect of increasing the diameter of the counter tubes. To avoid interference between adjacent tubes, the center-to-center separations were also increased by the same factors. At low energies, the effect is clearly different from that for the gas pressure in Figure 2.3. Because the probability of capture in the gas is already very high at these energies, increases in efficiency come mainly from increasing the counter area, not from raising the pressure. In contrast, at high energies the effect of increasing the counter volume is almost cancelled by the resulting decrease in the polyethylene and the displacement of the counters away from the center of the detector. Unfortunately, in these calculations it is impossible to separate these two effects.

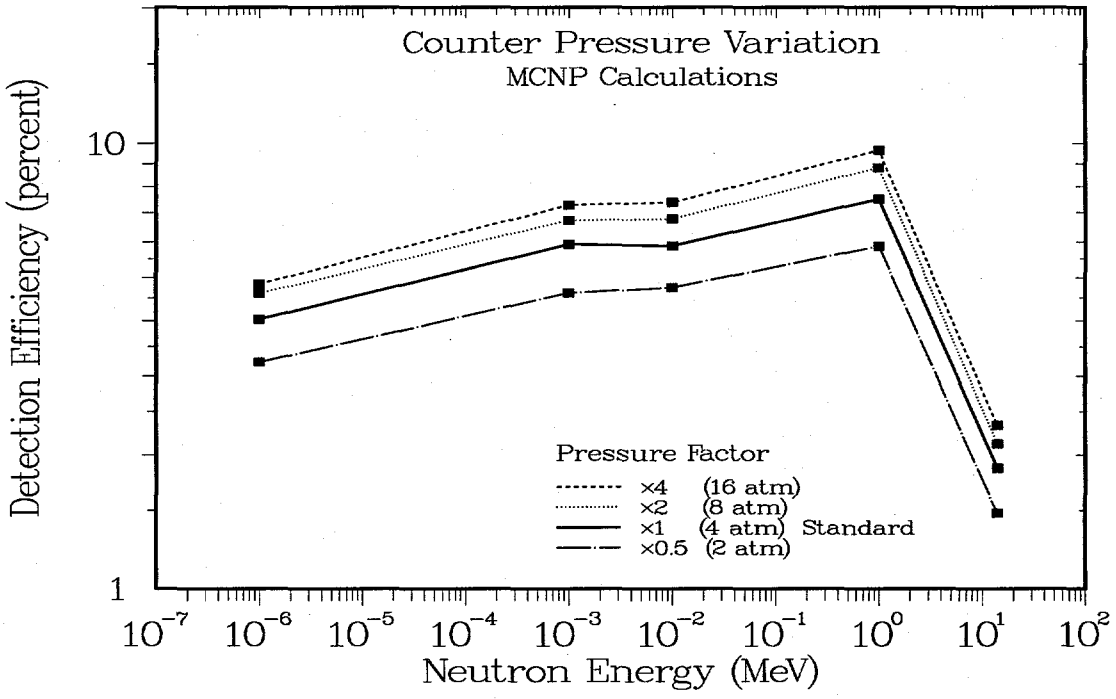

Figure 2.3. Effect of changes in gas pressure on detection efficiency.

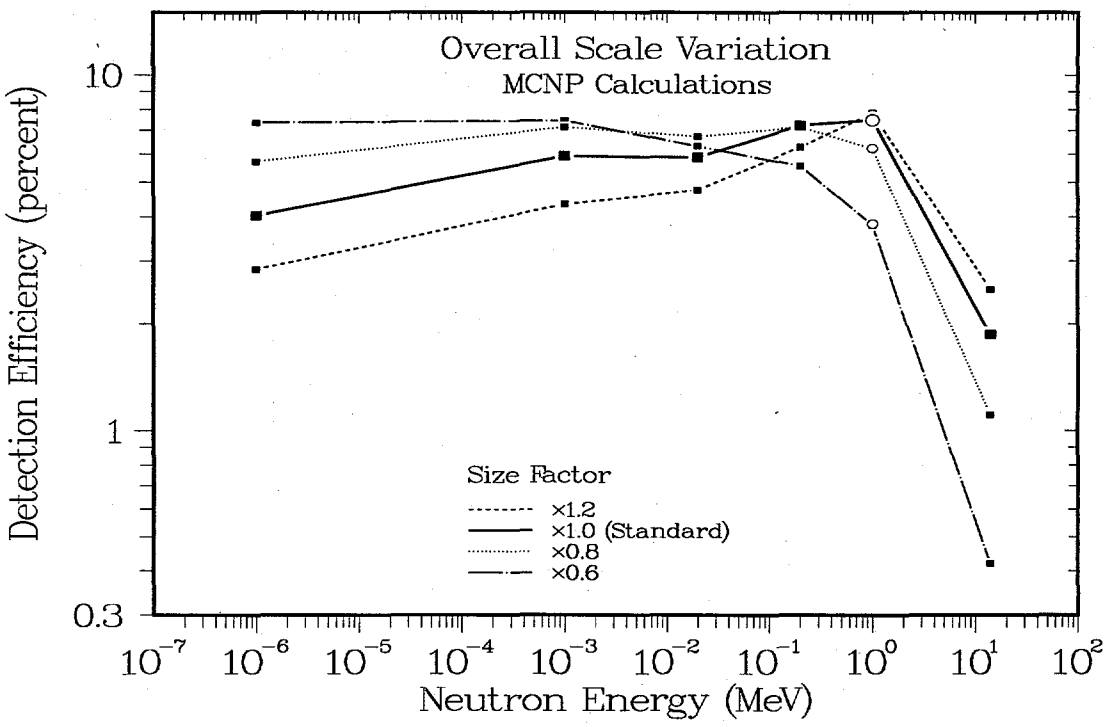

Figure 2.4. Effect of changes in moderator size on efficiency.

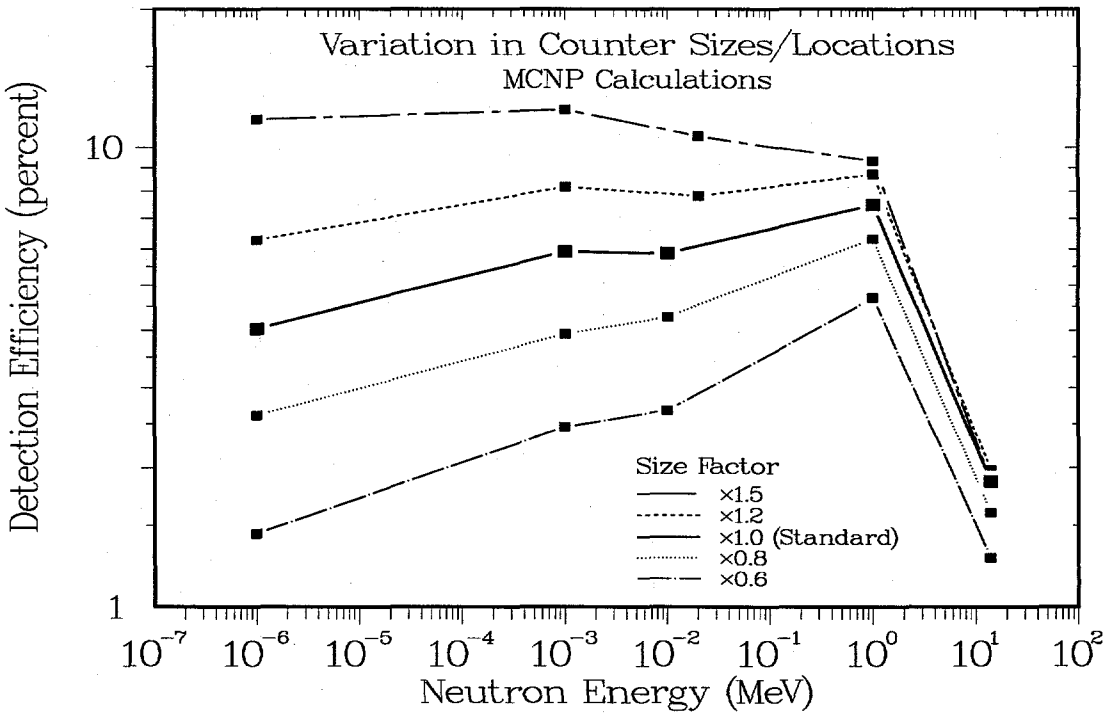

Figure 2.5. Effect of changing counter diameter and position.

2.3. Performance Measures

Effective Area. The analyses presented in Ref. 5 expand the focus by including the angular dependence of the detector's efficiency. In the process, the idea of efficiency, the av-

erage probability of detecting a neutron that strikes the detector, is replaced by the concept of "effective area" A_{eff}, the product of the efficiency and projected area. This new quantity can be interpreted conveniently as the physical area of an equivalent detector with 100% detection efficiency, which immediately leads to the neutron count rate for a unit incident flux of 1 n per cm^2/s. As we shall see throughout our discussions, this simple connection between incident fluence and neutron count rate makes it much easier to evaluate changes in the detector geometry or orientation. In practice, the value of A_{eff} is most simply obtained by dividing the observed number of neutron captures by the incident neutron fluence in n/cm^2, which is a quantity that can easily be measured or calculated. An example is given by **Figure 2.6**, which shows the effect of changing the moderator* diameter by 5%. Although this change affects both the intercepted fluence and the detection efficiency, the A_{eff} combination properly includes the effects of both factors. As in Figure 2.4, decreasing the amount of moderator increases the count rate at low energies and decreases the rate at high energies, with the crossover point in this example occurring near 50 keV.

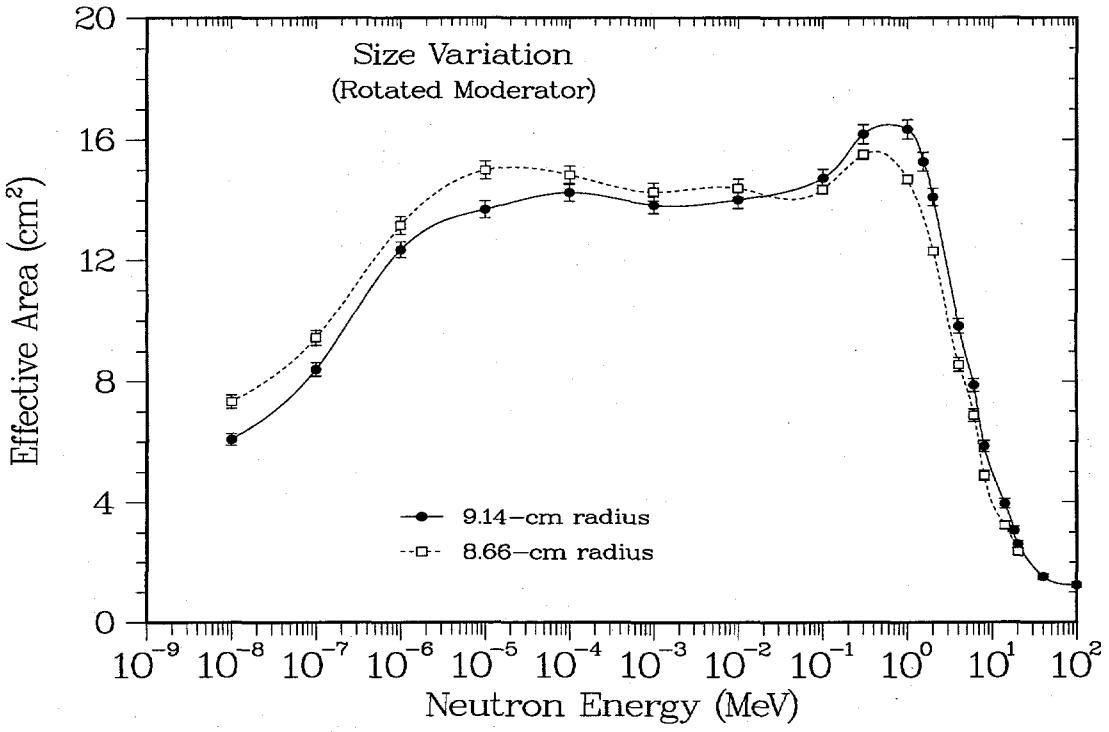

Figure 2.6. Effect on the efficiency of reducing the moderator size by 5%.

Directionality. Another application of effective areas is illustrated by **Figure 2.7** and **Figure 2.8**, which compare the energy distributions of the detection efficiencies for parallel beams of neutrons incident across, normal, and along the counter tubes. Because of the irregular outline of the detector, such calculations would be very difficult to compare using conventional efficiencies. In this case, the z-axis (end or along orientation) values at low energies show the effect of reducing attenuation through the polyethylene, and the mid-energy

* As discussed in Ref. 5, the calculations for all figures shown thus far inadvertently used a detector geometry in which the counter tubes in Figure 2.1 were rotated in the moderator by 90° about the z-axis. This rotation has little effect on our discussion and is corrected in the calculations for the remaining figures.

values for the *y*-axis (front or across orientation) show the shielding of one counter by the other. As indicated in Figure 2.8, however, all results converge at high energies, which indicates that the mean free paths in the moderator become large enough to average over any details of the geometry. At high energies we therefore expect the detector's performance to depend mainly on the amount of polyethylene present, not on its exact configuration. This point is further emphasized by **Figure 2.9**, which plots the differences between the counting rates for the two high-sensitivity tubes as a function of detector orientation. The asymmetry in count rates is expressed as the "analyzing power" *A*, which is calculated by dividing the count-rate difference by its sum. The maximum *A* value is 1.0, which is approached for the data in the *x*-axis (across) orientation at low energies. The results for the normal and along orientations give $A = 0$ because of detector symmetry. Significantly, the A_x values at the highest energies also approach zero because of the large mean free path. Note the single measurement for a Pu-Be neutron source, which is in good agreement with the calculations. Finally, we point out that directionality can refer to either angle measurements or angular dependence. Angular dependence refers to differences between the effective areas A_{eff} for the *x*-, *y*-, and *z*-axes, where a difference indicates undesirable nonuniformity in the detector response as a function of incident direction. In contrast, the angle measurements provided by a nonzero analyzing power *A* rely on an internal difference between the count rates for different tubes, which depends on the source direction. At least in principle, a rotationally symmetric detector with two carefully spaced counter tubes can have both good angular uniformity and a nonzero analyzing power.

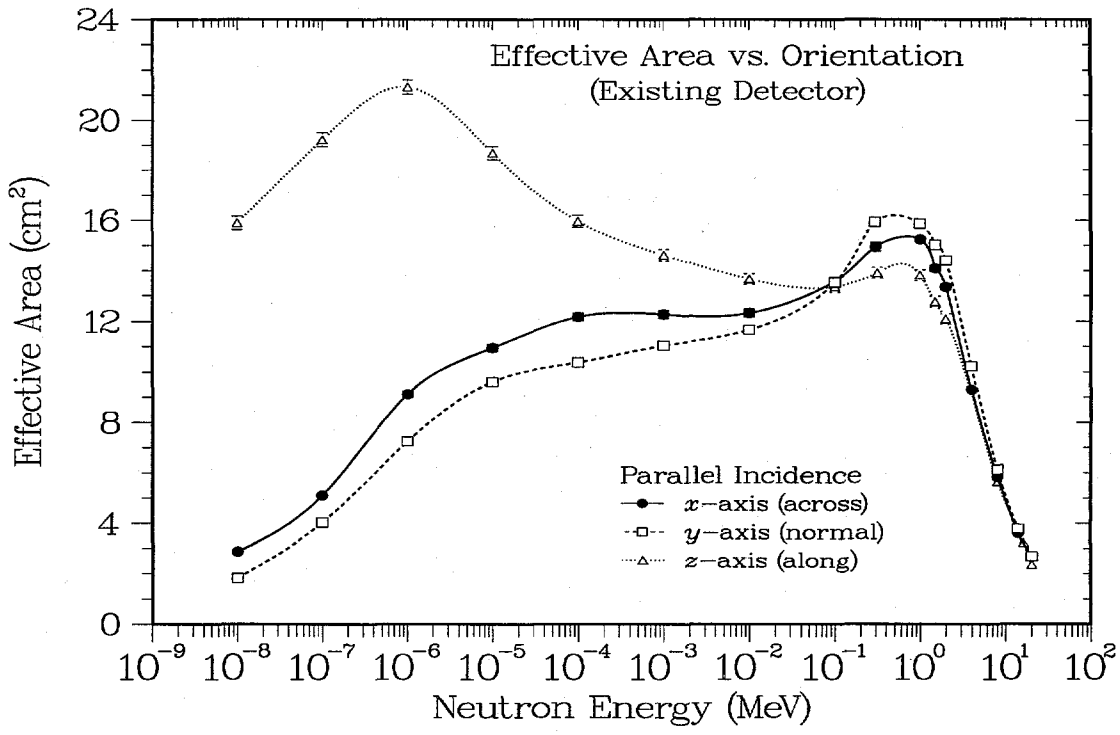

Figure 2.7. Energy distributions of the detection efficiency for neutron beams incident from three different directions.

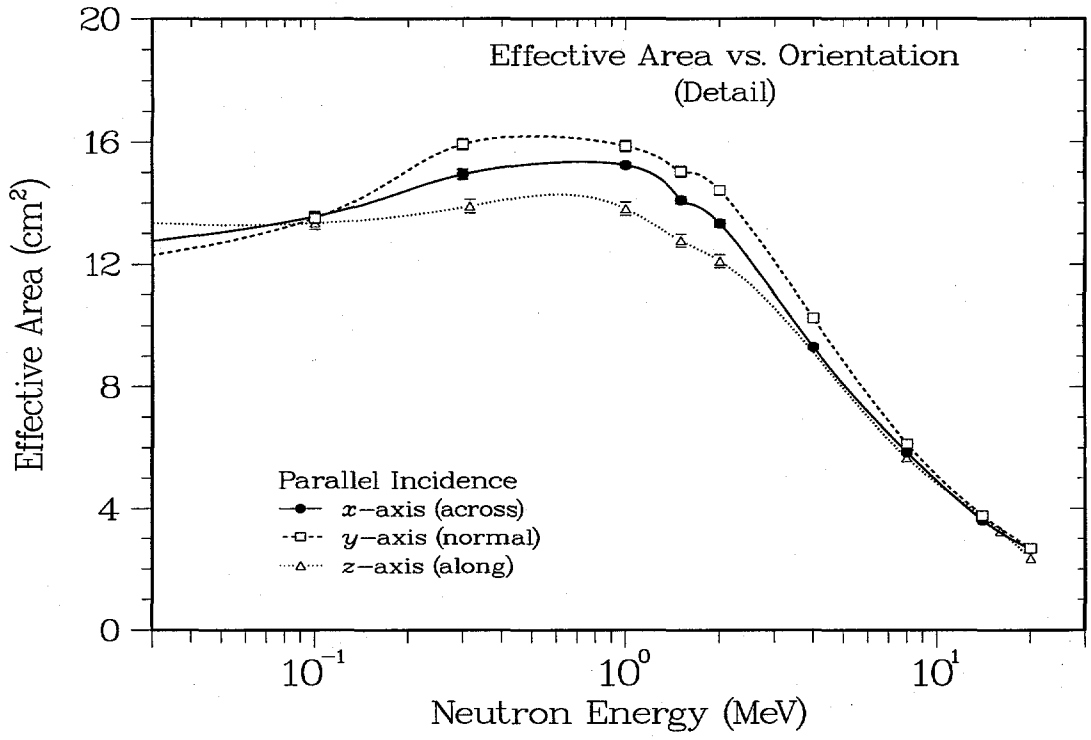

Figure 2.8. Detailed view of the high-energy efficiencies from Figure 2.7.

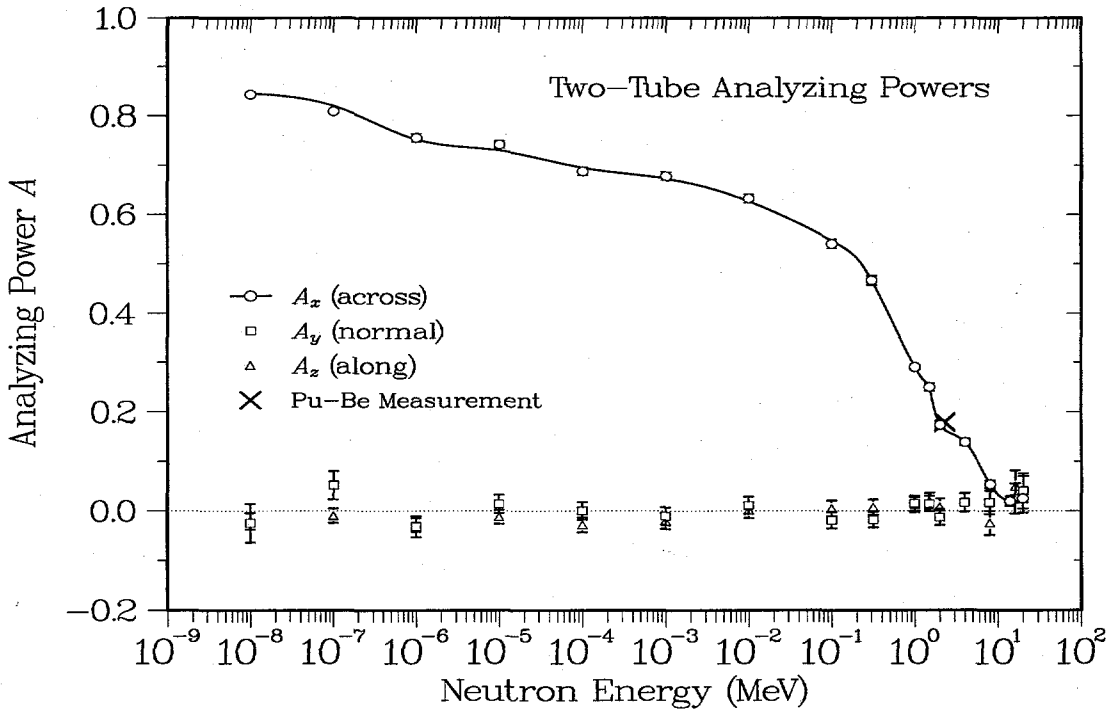

Figure 2.9. Fractional count-rate differences between the two high-sensitivity counters for neutrons incident with different energies and directions.

Numerical Results. Our earlier studies provide a good starting point for the present work, and it is important that the performance of any new design be competitive with that of the existing design. Accordingly, in **Table 2.1** we reproduce the numerical values for the three-axis effective areas (Figure 2.7) and the nonzero x-axis analyzing powers (Figure 2.9) for the existing detector.[5] These calculations use parallel beams of essentially monoenergetic neutrons; for example, the 1-MeV range was 0.95–1.05 MeV. As stated previously, detector directionality occurs both as differences in the A_{eff} values and as the size of the A_x values. This directionality is largest at low energies and almost disappears above 10 MeV because of increases in the neutron mean free path.

Table 2.1. Calculated Effective Areas and Analyzing Powers

Energy (MeV)	A_{eff} x-axis (cm^2)	A_{eff} y-axis (cm^2)	A_{eff} z-axis (cm^2)	Analyzing Power (x-axis)
1E–8	2.87 ± 0.02	1.81 ± 0.02	15.89 ±0.26	0.84
1E–7	5.10 ± 0.04	4.03 ± 0.07	19.22 ± 0.28	0.81
1E–6	9.10 ± 0.11	7.24 ± 0.10	21.30 ± 0.29	0.76
1E–5	10.94 ± 0.13	9.61 ± 0.12	18.67 ± 0.26	0.74
1E–4	12.17 ± 0.14	10.37 ± 0.12	15.94 ± 0.23	0.69
1E–3	12.28 ± 0.14	11.03 ± 0.13	14.62 ± 0.22	0.68
1E–2	12.32 ± 0.14	11.66 ± 0.13	13.65 ± 0.21	0.63
1E–1	13.56 ± 0.15	13.51 ± 0.15	13.34 ± 0.21	0.54
0.3	14.94 ± 0.16	15.92 ± 0.16	13.90 ± 0.21	0.47
1.0	15.23 ± 0.07	15.86 ± 0.16	13.81 ± 0.21	0.29
1.5	14.09 ± 0.11	15.02 ± 0.16	12.76 ± 0.20	0.25
2	13.33 ± 0.11	14.41 ± 0.11	12.09 ± 0.20	0.17
4	9.29 ± 0.06	10.23 ± 0.08	13.9	
8	5.84 ± 0.04	6.13 ± 0.05	5.65 ± 0.13	0.05
14	3.61 ± 0.03	3.78 ± 0.03	2.0	
16	3.23 ± 0.10			
20	2.65 ± 0.02	2.68 ± 0.02	2.34 ± 0.08	0.03

2.4. Summary

Discussion. Our earlier studies focused on determining the performance of a particular existing instrument and on understanding the effect of relatively small changes in its basic design. For example, increasing the amount of polyethylene moderator or ^{3}He gas, either by increasing the gas pressure or the size of the tubes, is expected to increase the detection efficiency for neutrons at high energies. The amount of this increase is limited, however, and the effects at high energies are often very different from those at low energies. Furthermore, the improvements in efficiency may be different for neutrons incident from different directions, so it is important to consider the effect of several detector orientations. In all cases, the use of effective areas makes it much easier to understand how changes in geometry or orientation affect the final counting rate. Unfortunately, it is usually difficult to extrapolate the results of these studies to other instruments with considerably different geometries, which is the problem addressed in the present study.

3. MONTE CARLO TECHNIQUES

Overview. As discussed in Chap. 2, the design of the existing detector was developed largely empirically, using experimental measurements with nearly monoenergetic neutron beams from low-energy particle accelerators. Such facilities are no longer commonly available, so the design for the replacement system is being developed using computer simulations. This chapter explains the basic assumptions about the configuration of the proposed SABRS Advanced Neutron (SAN) Detector. We also discuss the techniques for carrying out the simulations, and we present some representative results as functions of angle and energy. Comparisons are also made to the earlier calculations for the existing detector. In the process, we establish the necessity for developing an analytical model that relates the values of the individual detector parameters to the performance of the overall instrument. Such a model is important for understanding the operation of the detector and especially for optimizing its performance.

3.1. Basic Geometry

Detector Assumptions. Although our overall goal is to provide a detector with as large a detection efficiency as possible for a given size and weight, in practice the proposed design is bounded by the following constraints:

- The dimensions should be approximately 8″×6″×5″ (20.3×15.2×12.7 cm), but larger and certainly smaller detectors should also be explored.
- The effective areas at 1.5 MeV and 14 MeV should be at least as large as those for the existing system, about 14 cm^2 and 3.6 cm^2 (see Table 2.1).
- The ^3He tube selection should favor the existing case of an 8″ total length with a 4-atm pressure and a 1″ diameter, but changes in the latter two parameters should be investigated.
- The BF_3 gas used for the reduced-sensitivity tubes should be avoided, because this compound must now be handled as a hazardous material.
- Four shielded scintillator assemblies for a related gamma-ray detection system are to be embedded lengthwise in the corners of the moderator (see Ref. 6).

Although these requirements do not place very strong limits on the detector's design space, two simplifications are readily apparent. First, because BF_3 has a lower neutron-capture cross section than the ^3He alternative, it is unlikely that ^3He counters can be used for the low-sensitivity channels even at greatly reduced size and pressure. The present analysis therefore includes no comprehensive studies of the low-sensitivity channels, although some recommendations are included in the conclusions. Second, because the two high-sensitivity tubes in the existing design are ganged together, it is unlikely that the existing efficiency can be matched by any reasonable design using only a single tube of the same type. Instead, alternative designs could

- increase the polyethylene dimensions,
- use higher gas pressures,
- use larger tube radii,
- move the tube(s) back and forth relative to the front of the detector, or
- move the tubes closer together or farther apart.

Note that the overall tube lengths are constrained to 8″ by the proposed application. Our analyses consider variations in essentially all other parameters.

Detailed Specifications. As a starting point, the MCNP input file for a "reference" detector with two 1″ high-sensitivity tubes and a single 0.5″ low-sensitivity tube is reproduced in **Table 3.1**. End and top views of the resulting geometry are shown in **Figure 3.1** and **Figure 3.2**. The basic 8″ long by 6″ high by 5″ thick block of high-density polyethylene is cell 1. The top (t) and bottom (b) high-sensitivity tubes (cells 8 and 9 in the first section of Table 3.1) are placed one above the other, in this case with a front/back offset of zero (see cylindrical surfaces 18 and 19 in the second section of the table). A center low-sensitivity (l) tube (cell 10) is offset 2″ toward the front of the detector, almost between the front two scintillators. The 4-atm active regions of the tubes are 6″ long for the high-sensitivity tubes and 4″ long for the low-sensitivity tube; the active ^{3}He gas is material 2. (Note that 1 atm is assumed to be defined at STP.) There are 1″ dead regions at the ends of each tube (cells 11–16); these regions also contain 4-atm ^{3}He, but they are distinguished by labeling them as material 3 and using a slightly different density. Any spaces between the ends of the tubes and the outer boundaries of the detector are filled with polyethylene plugs (cells 2–7). The tube walls (cells 17–19) are made of 0.051-cm (20-mil) stainless steel (material 4). The scintillators (cells 45–48) are rods of BC400 plastic scintillator (material 6), which are 6″ long and 1″ in diameter. The rods are surrounded by 20 mils of Ta shielding (material 5, cells 49–52) and are inserted into cavities that are 1.25″ in diameter and located along the four corners of the polyethylene block. At the ends of each scintillator are 0.165″ lead-glass light guides (cells 37–44, material 9), and voids are used to represent the photomultipliers (cells 29–36). The remainder of the file is either simple voids or the complex structures needed to provide the angular distributions discussed later in this chapter.

Table 3.1. Sample MCNP Input File

```
8"x6"x5" 2 tubes 1" 4-atm 0" offset 2" sep
C    CELL CARDS
 1    1  -0.96 11 -10 2 -5 8 -9 21 23 22 36 37 38 39  IMP:N=1 $POLY
 2    1  -0.96    +11 -25                      -22     IMP:N=2 $L UP POLY PLUG
 3    1  -0.96    +24 -10                      -22     IMP:N=2 $R UP POLY PLUG
 4    1  -0.96    +11 -25                      -21     IMP:N=2 $L LO POLY PLUG
 5    1  -0.96    +24 -10                      -21     IMP:N=2 $R LO POLY PLUG
 6    1  -0.96    +11 -13                      -23     IMP:N=2 $L CE POLY PLUG
 7    1  -0.96    +12 -10                      -23     IMP:N=2 $R CE POLY PLUG
 8    2  -5.34e-4 +13 -12                      -19     IMP:N=4 $UP 3HE ACTIVE
 9    2  -5.34e-4 +13 -12                      -18     IMP:N=4 $LO 3HE ACTIVE
10    2  -5.35e-4 +27 -26                      -20     IMP:N=4 $CE 3HE ACTIVE
11    3  -5.34e-4 +25 -13                      -19     IMP:N=3 $UP 3HE LEFT DEAD
12    3  -5.34e-4 +25 -13                      -18     IMP:N=3 $LO 3HE LEFT DEAD
13    3  -5.35e-4 +13 -27                      -20     IMP:N=3 $CE 3HE LEFT DEAD
14    3  -5.34e-4 -24 +12                      -19     IMP:N=3 $UP 3HE RGHT DEAD
15    3  -5.34e-4 -24 +12                      -18     IMP:N=3 $LO 3HE RGHT DEAD
16    3  -5.35e-4 +26 -12                      -20     IMP:N=3 $CE 3HE RGHT DEAD
17    4  -7.81    +25 -24                      +19 -22 IMP:N=2 $UPPER SS
18    4  -7.81    +25 -24                      +18 -21 IMP:N=2 $LOWER SS
19    4  -7.81    +13 -12                      +20 -23 IMP:N=2 $CENTER SS
21    0          -11 -1                               IMP:N=0 $LEFT VOID
22    0          +10 -1                               IMP:N=0 $RIGHT VOID
23    0          -14 #(+8 -9 +2 -5) -1        +11 -10 IMP:N=1 $VOID AROUND DET
24    0          +15 -1                       +11 -10 IMP:N=0 $VOID BEHIND SRCE
```

```
25    0           +14 -15 -17 -1          +11 -10 IMP:N=0 $VOID IN SRCE PLN
26    0           +14 -15  16 -1          +11 -10 IMP:N=0 $VOID IN SRCE PLN
27    0           +14 -15 +17 -16         +11 -10 IMP:N=1 $SOURCE REGION
28    0            +1                             IMP:N=0 $UNIVERSE
29    0           +11 -41  -36                    IMP:N=1 $LEFT SC VOID BL
30    0           +11 -41  -37                    IMP:N=1 $LEFT SC VOID TL
31    0           +11 -41  -38                    IMP:N=1 $LEFT SC VOID TR
32    0           +11 -41  -39                    IMP:N=1 $LEFT SC VOID BR
33    0           +40 -10  -36                    IMP:N=1 $RIGHT SC VOID BL
34    0           +40 -10  -37                    IMP:N=1 $RIGHT SC VOID TL
35    0           +40 -10  -38                    IMP:N=1 $RIGHT SC VOID TR
36    0           +40 -10  -39                    IMP:N=1 $RIGHT SC VOID BR
37    9  -1.7     +41 -13  -28                    IMP:N=1 $LEFT PB GLASS BL
38    9  -1.7     +41 -13  -29                    IMP:N=1 $LEFT PB GLASS TL
39    9  -1.7     +41 -13  -30                    IMP:N=1 $LEFT PB GLASS TR
40    9  -1.7     +41 -13  -31                    IMP:N=1 $LEFT PB GLASS BR
41    9  -1.7     +12 -40  -28                    IMP:N=1 $RGHT PB GLASS BL
42    9  -1.7     +12 -40  -29                    IMP:N=1 $RGHT PB GLASS TL
43    9  -1.7     +12 -40  -30                    IMP:N=1 $RGHT PB GLASS TR
44    9  -1.7     +12 -40  -31                    IMP:N=1 $RGHT PB GLASS BR
45    6  -1.032   +13 -12  -28                    IMP:N=1 $SC BL
46    6  -1.032   +13 -12  -29                    IMP:N=1 $SC TL
47    6  -1.032   +13 -12  -30                    IMP:N=1 $SC TR
48    6  -1.032   +13 -12  -31                    IMP:N=1 $SC BR
49    5  -16.65   +41 -40  +28 -32                IMP:N=1 $TA BL
50    5  -16.65   +41 -40  +29 -33                IMP:N=1 $TA TL
51    5  -16.65   +41 -40  +30 -34                IMP:N=1 $TA TR
52    5  -16.65   +41 -40  +31 -35                IMP:N=1 $TA BR
53    0           +41 -40  +32 -36                IMP:N=1 $VOID ARND TA BL
54    0           +41 -40  +33 -37                IMP:N=1 $VOID ARND TA TL
55    0           +41 -40  +34 -38                IMP:N=1 $VOID ARND TA TR
56    0           +41 -40  +35 -39                IMP:N=1 $VOID ARND TA BR
57    0            +2 +8   -58 +36                IMP:N=1 $CORNER VOID LB
58    0            -5 +8   +57 +37                IMP:N=1 $CORNER VOID LT
59    0            -5 -9   -60 +38                IMP:N=1 $CORNER VOID RT
60    0            +2 -9   +59 +39                IMP:N=1 $CORNER VOID RB

C     SURFACE CARDS
24    PZ +10.16                    $3HE TUBE RIGHT BOUNDARY (+4")
25    PZ -10.16                    $3HE TUBE LEFT BOUNDARY (-4")
10    PZ +10.17                    $POLY LEFT SURFACE  (+4")
11    PZ -10.17                    $POLY RIGHT SURFACE (-4")
12    PZ  +7.62                    $3HE DEAD LEFT (8" TUBES)
13    PZ  -7.62                    $3HE DEAD RIGHT
26    PZ  +5.08                    $3HE DEAD LEFT SHORT (6" TUBES)
27    PZ  -5.08                    $3HE DEAD RIGHT SHORT
14 4  PY   0                       $INNER SOURCE BOUNDARY
15 4  PY   1                       $OUTER SOURCE BOUNDARY
40    PZ  +8.06                    $PB GLASS LEFT
41    PZ  -8.06                    $PB GLASS RIGHT
57 6  PY   0                       $TL PLANE LL-UR, +LEFT/UPWARD
58 5  PX   0                       $BL PLANE UL-LR, -LFT/DN
59 8  PY   0                       $BR PLANE LL-UR, -RGT/DWN
60 7  PX   0                       $TR PLANE UL-LR, +RIGHT/UPWARD
18    C/Z  0.000  -1.270   1.270   $BHe
19    C/Z  0.000   3.810   1.270   $THe
20    C/Z -5.080   1.270   0.635   $MHe
21    C/Z  0.000  -1.270   1.321   $Bss
```

```
22    C/Z  0.000   3.810   1.321   $Tss
23    C/Z -5.080   1.270   0.686   $Mss
28    C/Z -4.760  -4.760   1.270   $LBS
29    C/Z -4.760   7.300   1.270   $LTS
30    C/Z  4.760   7.300   1.270   $RTS
31    C/Z  4.760  -4.760   1.270   $RBS
32    C/Z -4.760  -4.760   1.321   $LBT
33    C/Z -4.760   7.300   1.321   $LTT
34    C/Z  4.760   7.300   1.321   $RTT
35    C/Z  4.760  -4.760   1.321   $RBT
36    C/Z -4.760  -4.760   1.590   $LBH
37    C/Z -4.760   7.300   1.590   $LTH
38    C/Z  4.760   7.300   1.590   $RTH
39    C/Z  4.760  -4.760   1.590   $RBH
 1    SO  16.13                   $UNIVERSE
 9    PX   6.35                   $POLY FRONT
 8    PX  -6.35                   $POLY BACK
 5    PY   8.89                   $POLY TOP
 2    PY  -6.35                   $POLY BOT
16 4 PX   6.35                   $HIGH SOURCE LIMIT
17 4 PX  -8.89                   $LOW SOURCE LIMIT

C ANGLE=  0 DMIN=  1.0 DEPTH, HEIGHT= 12.7 15.2
*TR5      -4.7600 -4.7600     0  45  45 90  135 45 90  90 90 0 $LB PLANE
*TR6      -4.7600  7.3000     0  45  45 90  135 45 90  90 90 0 $LT PLANE
*TR7       4.7600 -4.7600     0  45  45 90  135 45 90  90 90 0 $RT PLANE
*TR8       4.7600  7.3000     0  45  45 90  135 45 90  90 90 0 $RB PLANE
*TR4      -7.350   0.000  0.000  90 180 90  180 90 90  90 90 0
SDEF  CEL=27 DIR=1 ERG=D4 X=D1 Y=D2 Z=D3
      VEC= 1.000  0.000 0. WGT=  309.37
SI1      -8.36   -6.34
SI2      -7.35    9.89
NPS      400000
SI4     0.14E+02  0.16E+02
SI3     -10.15 10.15
SP1     0 1
SP2     0 1
SP3     0 1
SP4     0 1
M4      14000.50C .01 24000.50C .19 25055.50C .02
        26000.55C .68 28000.50C .10
M2      2003.50C 1.0
M3      2003.50C .99 2004.50C .01
M1      1001.50C 2. 6000.50C 1.
MT1     POLY.01T
M5      73181.50c 1.  $ta -16.654
M6      1001.50C 1.104 6000.50c 1.
M9      14000.50c 1. 8016.50c 2.  82000.50c 1.  $THICK=0.444 RAD=1.27
PRINT   30 40 50 60 140
F4:N    8 9 10 T
E0      1E-8 1E-7 1E-6 1E-5 1E-4 1E-3 1E-2 1E-1 .4 1 1.5 2 3 4 5 7 10
```

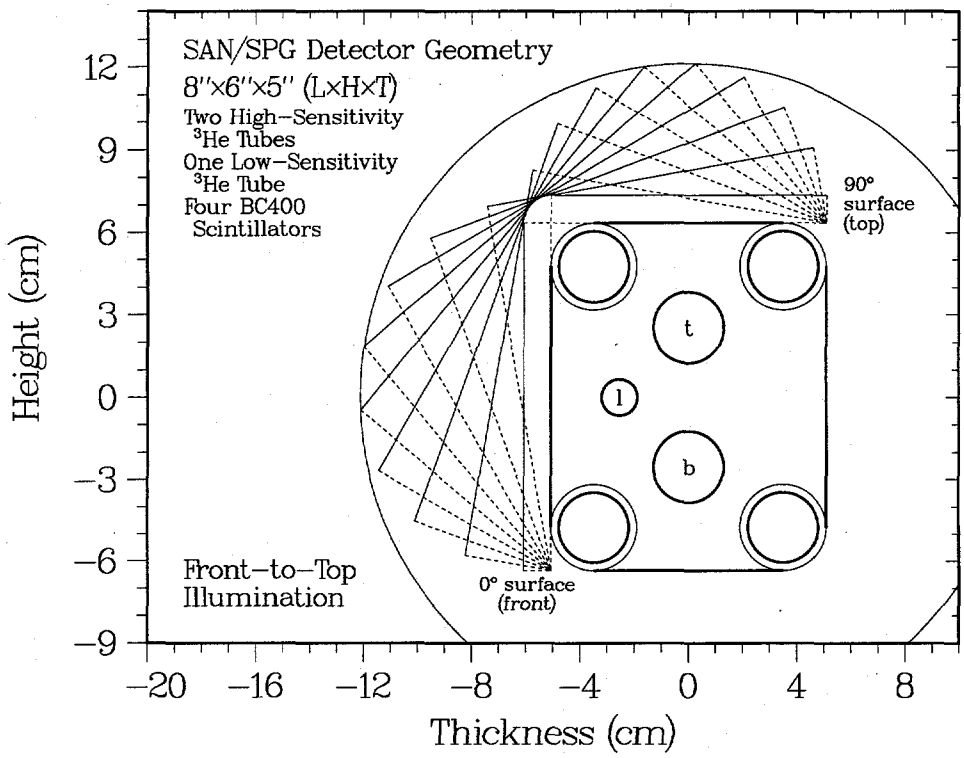

Figure 3.1. End-on view of the reference SAN detector geometry, showing source planes running from 0° (front) to 90° (top).

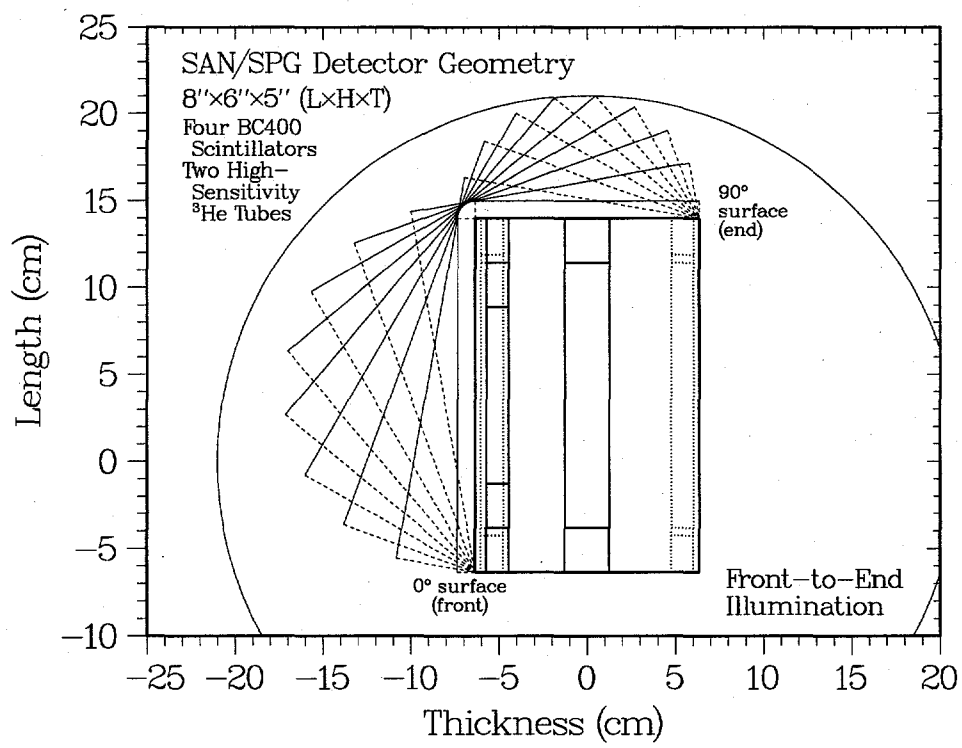

Figure 3.2. Top view of the reference geometry, showing source planes running from 0° (front) to 90° (end).

Energy and Angle Variations. As indicated in Figure 3.1 and Figure 3.2, an important part of the MCNP input is the construction of source planes that rotate in 10° steps around the detector from front to top (Figure 3.1) or front to end (Figure 3.2). Four different types of input files are needed to handle these different rotations, two each for the one-tube and two-tube detectors. The example file in Table 3.1 is the 0° (front) case from a front-to-top rotation around a two-tube detector. As the source plane (cell 27) rotates, its dimensions change to illuminate the entire detector, and the weight of each source particle also changes to produce a unit fluence of 1 n/cm^2. Each set of 10 input runs for a top or end detector rotation provides a complete angular scan about one axis, which is automatically repeated 9 times to give 9 separate incident-energy bins. The full set of energy bins and the reference midpoint energies E_n are given in **Table 3.2**; the file in Table 3.1 is for the bin extending from 14 to 16 MeV. In addition to this set of 10 angles at 9 energies, a complementary set of 10 runs is carried out at the same 10 angles, but with a VOID card added to the MCNP file to turn off all interactions. These 10 VOID runs are used to check that the particle weights correctly provide unit fluences when averaged over the detector. The average of these 10 fluences is then divided into the capture rates for the other 90 runs to provide the complete set of angle-and-energy distributions of the effective area for the existing detector geometry.

Table 3.2. MCNP Energy Bins

Upper Energy (MeV)	Assumed Midpoint (MeV)
1E–6	<1E–6
0.1	3E–4
1	0.3
2	1.5
4	3
8	6
12	10
14	13
16	15

3.2. Front-to-Top Illumination

Angular Distributions. We begin our discussion with the case of front-to-top detector illumination. The first set of results concerns the basic reference geometry for the input file in Table 3.1. **Figure 3.3** gives the angular distributions for each of the nine incident energy bins. The capture rates for the top and bottom tubes have been added together to provide a single effective area for the high-sensitivity range. The resulting rates are higher than those for the existing system (see Table 2.1) by about 30%. The angular nonuniformity is relatively small at both very low and very high energies, although for energies around 1 MeV there is a clear decrease toward back angles. Stronger variations are seen in the separate distributions for the top and bottom tubes, which are shown in **Figure 3.4** and **Figure 3.5**. Below 1 MeV, the count rates for the top tube decrease rapidly at forward angles, but almost the opposite dependence is seen in the rates for the bottom tube, which provides the cancellation that results in the nearly flat distributions in Figure 3.3. At energies above 1 MeV, however, even the sin-

gle-tube distributions are almost flat, which is a general result of the increasing neutron mean free paths.

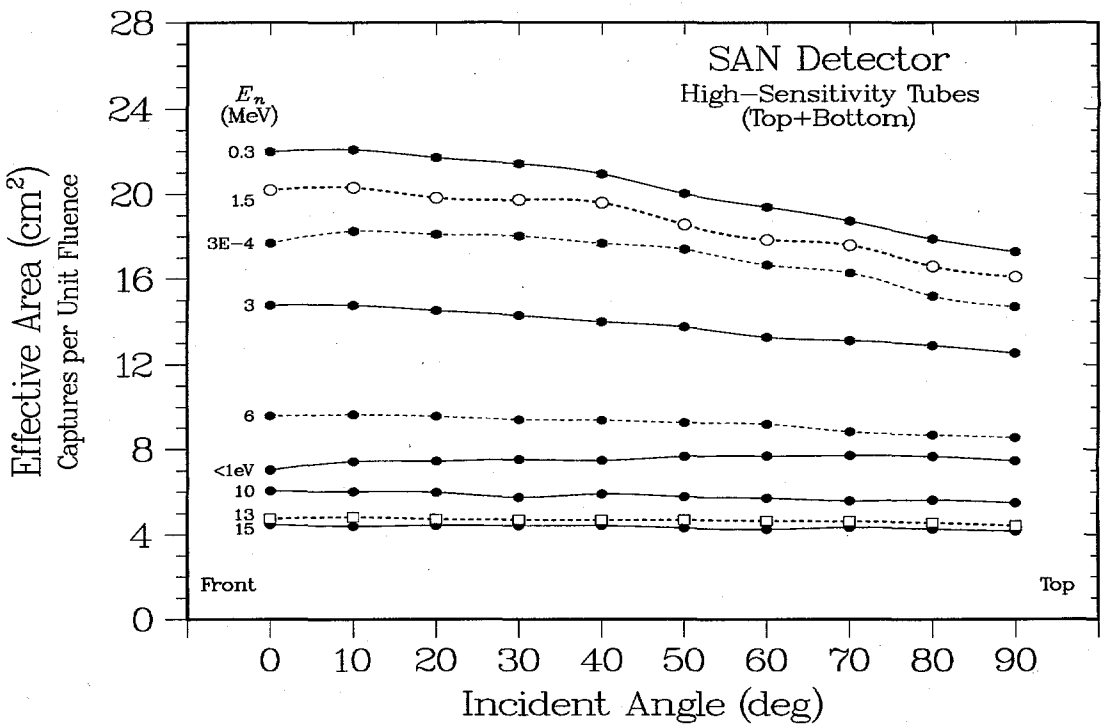

Figure 3.3. Angular distributions of the two-tube total effective areas for the reference detector in energy bins from thermal (<1 eV) to 15 MeV.

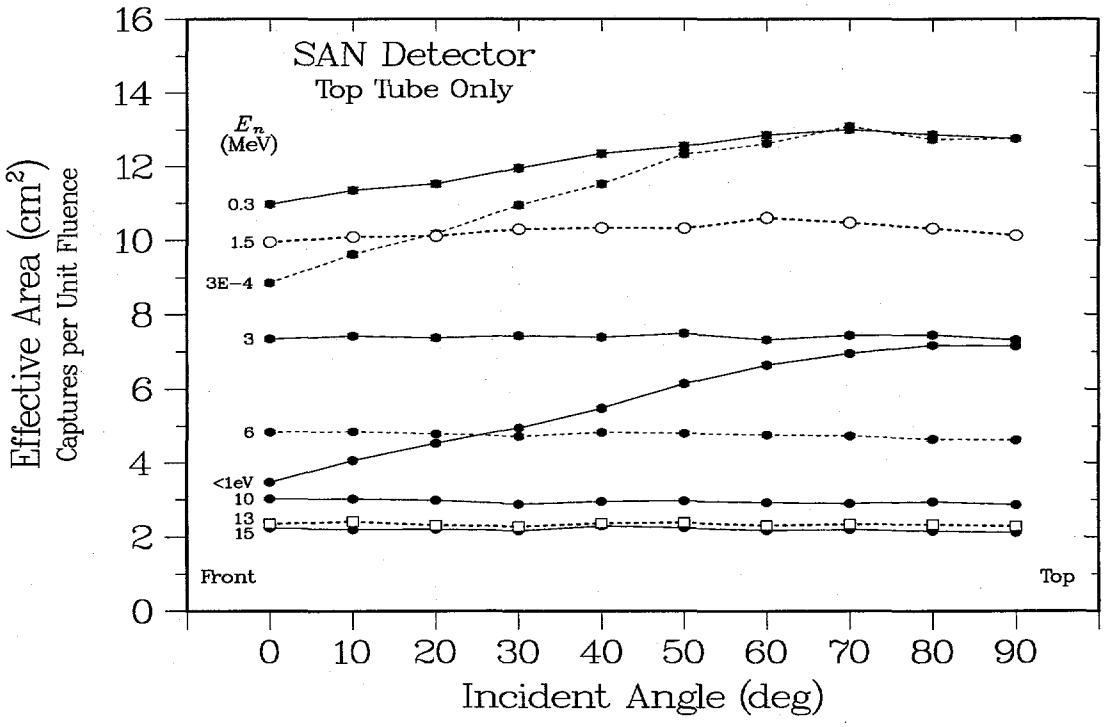

Figure 3.4. Effective areas as in Figure 3.3, but for the top tube only.

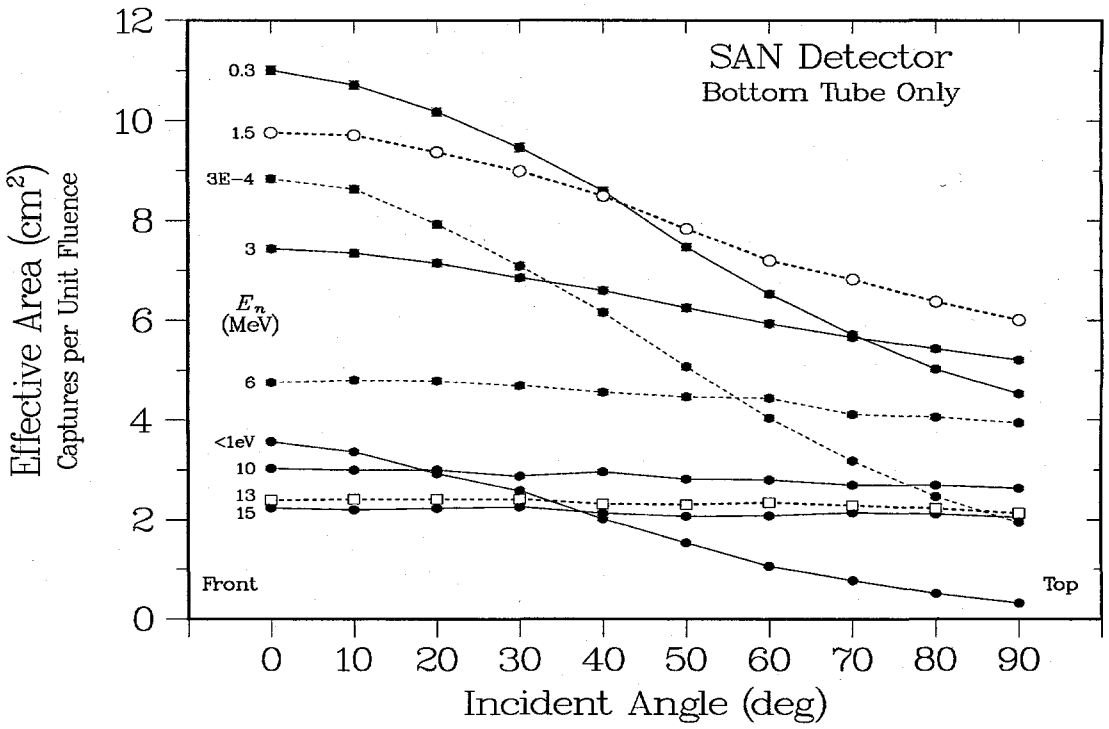

Figure 3.5. Effective areas as in Figure 3.3, but for the bottom tube only.

Energy Distributions. Next, in **Figure 3.6**, **Figure 3.7**, and **Figure 3.8** we show the energy distributions that correspond to the angular distributions in the three previous figures. Figure 3.6 gives the sum of the rates for the top and bottom tubes, which shows a consistently higher value at all energies for angles toward the front of the detector. Figure 3.7 and Figure 3.8 break the sum into its two components. This separation reveals that the rates are almost the same at both angles for the top tube, but they are very different for the bottom tube for illumination from the front or top. As would be expected for the bottom tube's greater distance from the upper face of the detector, the difference becomes much larger as the scattering and attenuation increases at lower neutron energies. This behavior suggests that the angular response for a one-tube detector with dimension equivalent to those for the upper half of the proposed two-tube geometry might provide an almost uniform angular response.

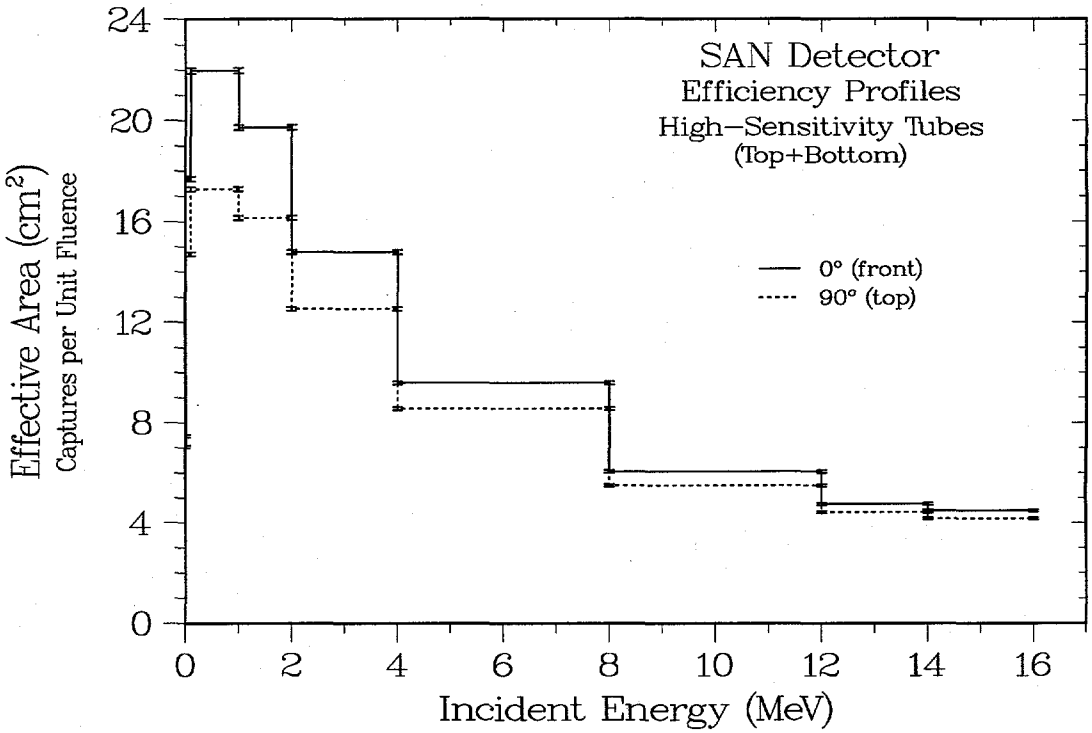

Figure 3.6. Energy distributions of the total two-tube effective areas as in Figure 3.3, but for 0° (front) and 90° (top) only.

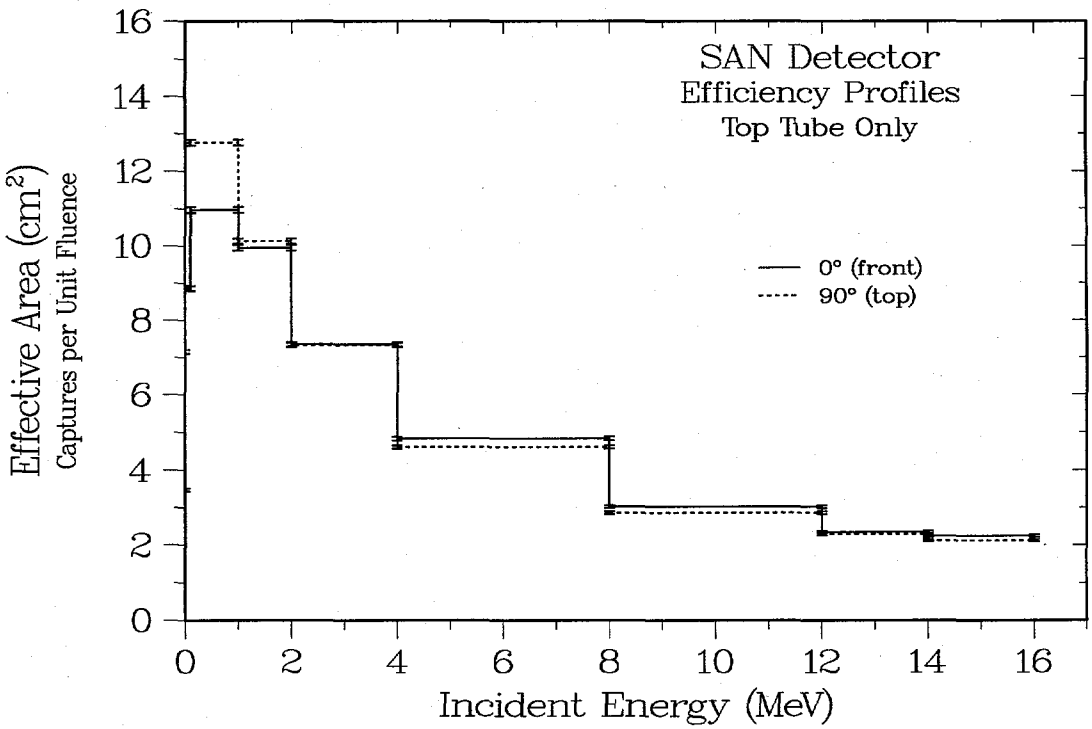

Figure 3.7. Energy distributions as in Figure 3.6, but for the top tube only.

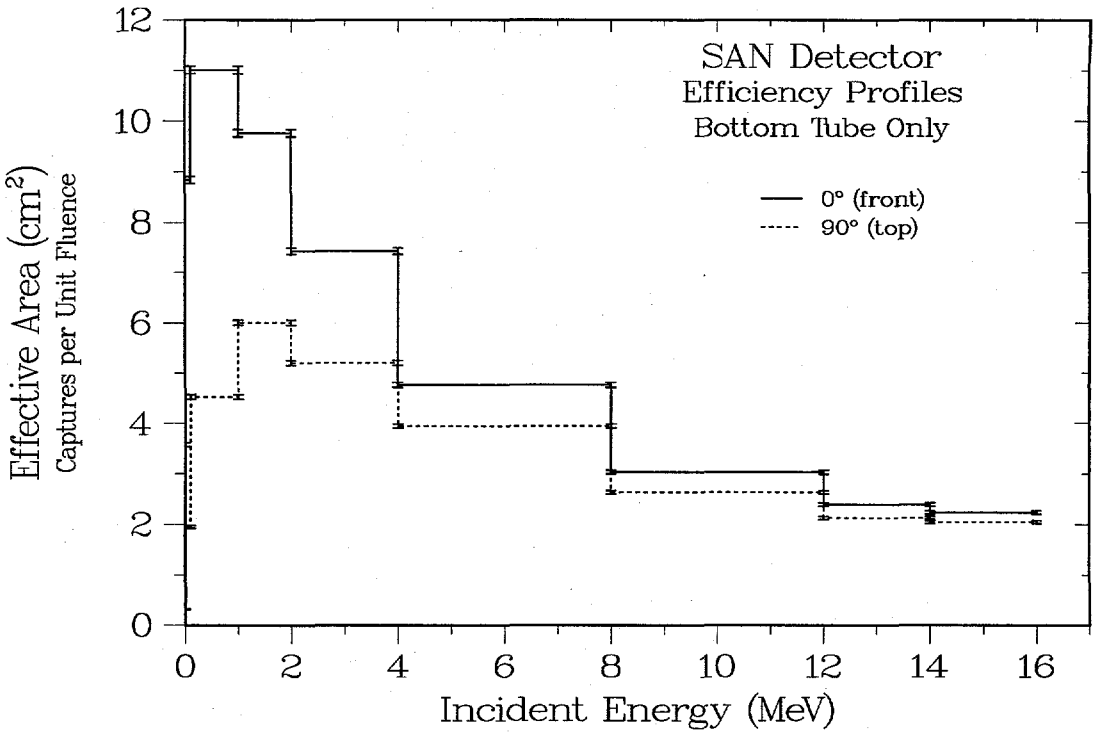

Figure 3.8. Energy distributions as in Figure 3.6, but for the bottom tube only.

3.3. Front-to-End Illumination

Effective Areas. The corresponding energy and angle behavior for the case of front-to-end illumination for the basic detector geometry is illustrated by the angular distributions in **Figure 3.9** and the energy distributions in **Figure 3.10**, in both cases for the sum of the top and bottom high-sensitivity tubes. Again, at the highest energies the response is almost angle-independent, but for lower energies the efficiency usually drops off rapidly. The only exception is for thermal neutrons, where the efficiency increases for incident angles almost directly parallel to the tube axes.

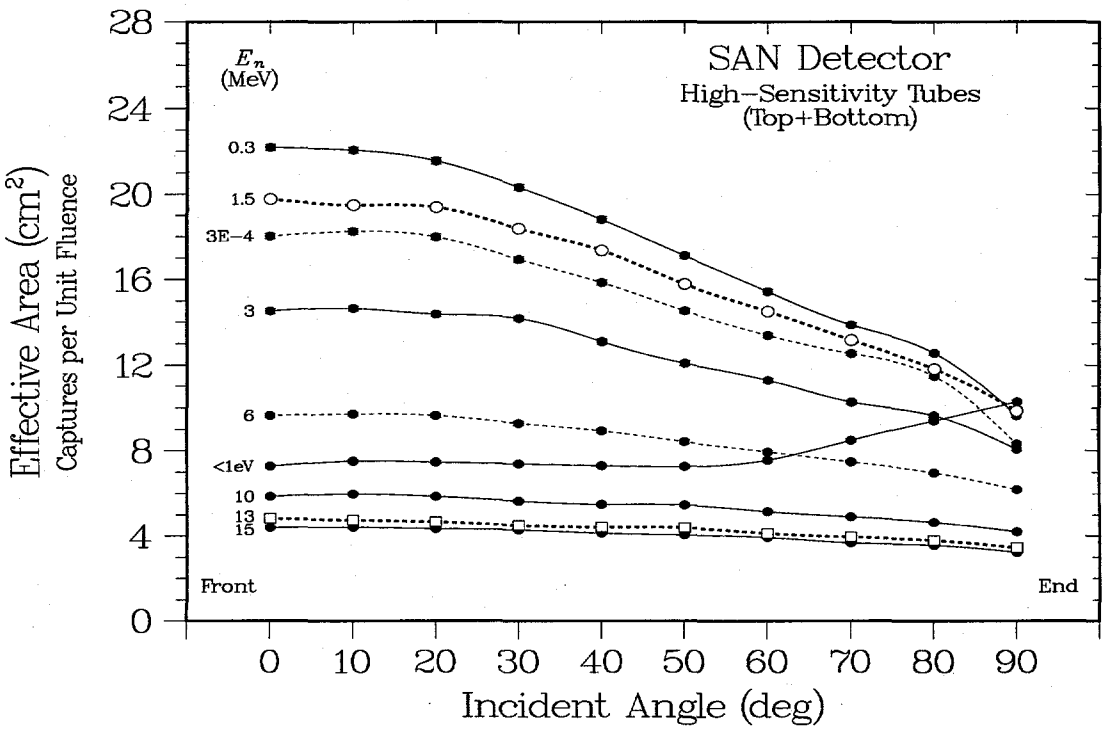

Figure 3.9. Angle-dependent effective areas as in Figure 3.3, but for angles running from 0° (front) to 90° (end).

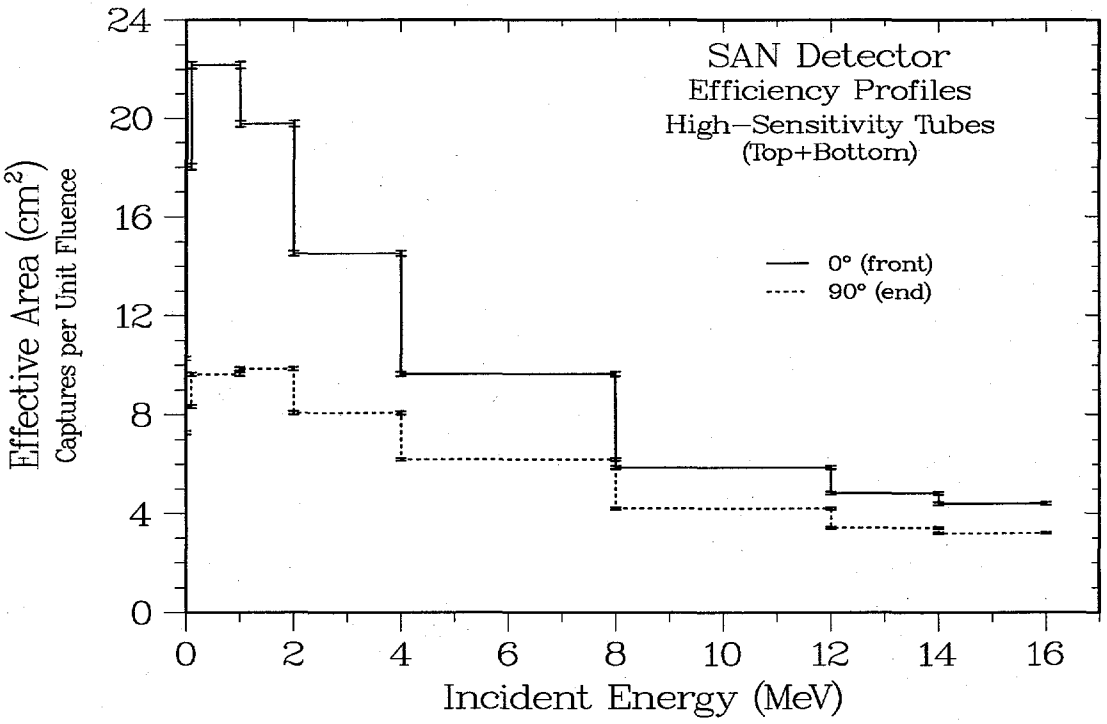

Figure 3.10. Energy distributions of the effective areas in Figure 3.6 for the cases of front (0°) and end illumination (90°).

3.4. Other Geometries

Scintillator Effects. An important issue in the proposed design is the effect of the four scintillator elements[6] located at the corners of the detector, which together constitute 0.16 kg (about 5%) of the hydrogenous (plastic) mass of the detector. Because the hydrogen content per unit mass of the scintillator material is only about 50% of that for the polyethylene, we have reduced the scintillator mass by 50% in computing the plastic mass. Although the use of scintillator instead of polyethylene implies some reduction in moderation efficiency, decreasing the attenuation at the corners of the detector might have the advantage of improving the uniformity of the detector's angular response. To investigate the performance of a comparable all-polyethylene detector, additional calculations were run with all non-polyethylene materials and internal voids replaced by polyethylene, which increases the plastic mass by about 0.2 kg (6%). As seen in **Figure 3.11** and **Figure 3.12**, there is clear evidence that the additional polyethylene increases the efficiency, but there is only a suggestion that the angular uniformity is affected at any energy. In fact, comparing the two sets of efficiencies per unit mass indicates that the polyethylene-plus-scintillator combination has a slightly higher efficiency than the all-polyethylene detector, probably because the scintillator case reduces the amount of inefficient moderator material at the detector's extreme corners. In short, when the change in plastic mass is included it is unlikely that the scintillators have any significant effect on the effective area.

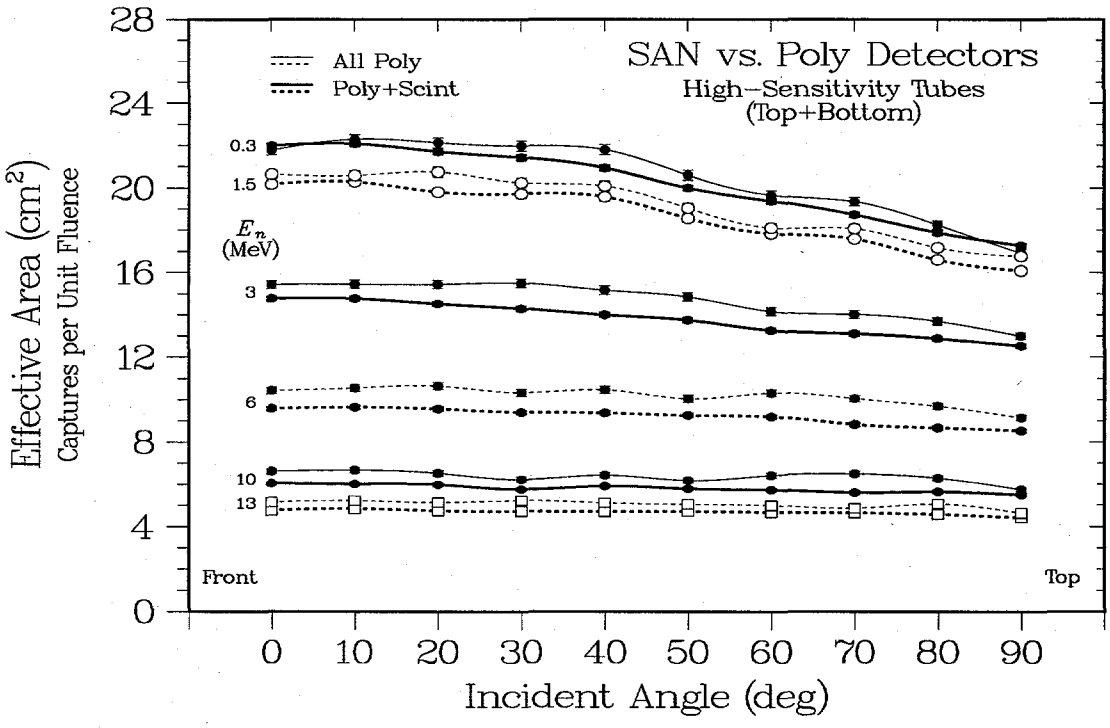

Figure 3.11. Comparison between the angular distributions of the effective areas of the reference SAN detector and the corresponding all-polyethylene design.

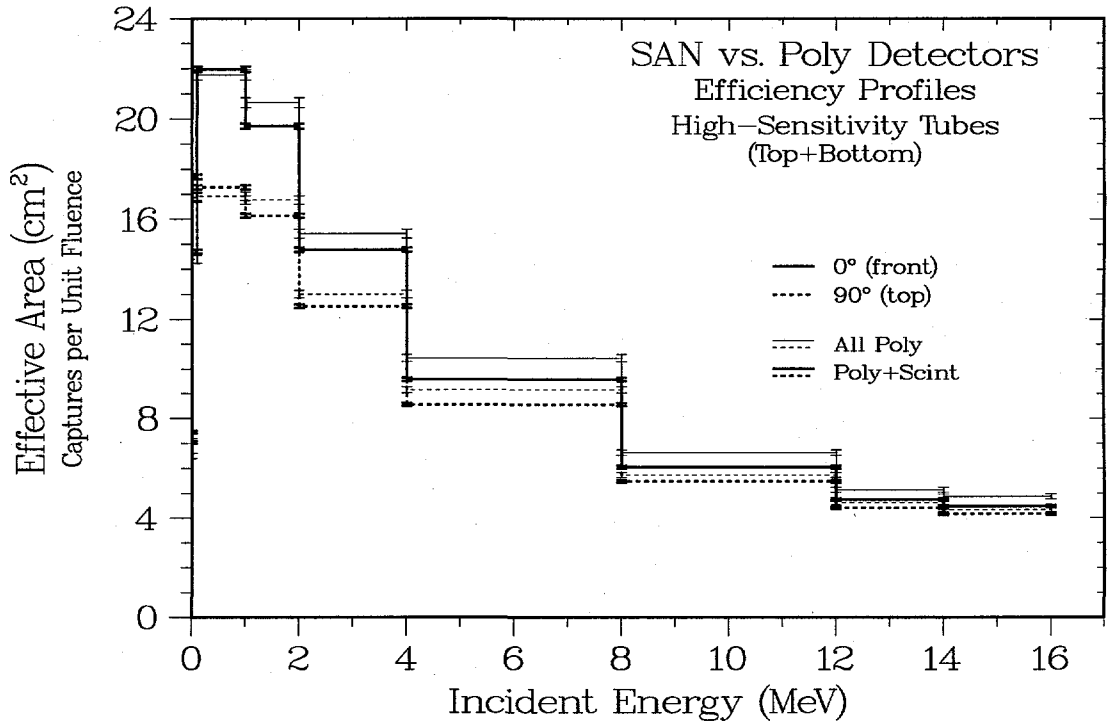

Figure 3.12. As in Figure 3.11, but for a comparison of the energy distributions.

Existing and Alternative Detectors. As represented by Figure 2.2 and Figure 2.7, previous studies[4,5] of the detection efficiency for the existing detector emphasize the dependence on energy, not on angle. In some cases, however, we can obtain angular information from the archived files, which provide the results shown in **Figure 3.13**. These distributions are calculated for incident neutron angles between the detector's *y*- and *x*-axes, that is, for the present front-to-top rotation. Despite the nearly symmetric moderator geometry, there is some residual anisotropy in the response because of the asymmetric tube orientation, with the effect increasing at the lowest energies. Although the nonuniformity in response is less than for the reference design (see Figure 3.3), even small changes in the geometry of our rectangular detector have a pronounced effect on its angular behavior. In **Figure 3.14**, **Figure 3.15**, and **Figure 3.16** we present examples of two such changes that will be followed throughout our analyses. First, in Figure 3.14 the variation labeled as 6″H×5″T is similar to the reference design, but the two high-sensitivity tubes have been offset toward the front of the detector by 0.5 cm (0.2″) and their separation has been increased from the reference 2″ value (5.08 cm) to 5.5 cm (2.17″). This 10% change has no effect on the detector mass, but it noticeably increases the efficiency near 1 MeV. Second, in Figure 3.15 the variation labeled 5.5″H×5.5″T includes the same offsets in tube position, but it also changes the detector height and thickness to provide a more symmetric design. In effect, the tubes are now farther from the detector's front and closer to its top and bottom. This change in moderator dimensions results in a nearly uniform angular response in both the front-to-top (Figure 3.15) and the front-to-end (Figure 3.16) illumination patterns. Note that these alternatives require at most a 1% change in the detector mass from the reference design, but they provide a response that is more forward directed (6″H×5″T) versus one that is more uniform in at least one plane (5.5″H×5.5″T). We will continue to highlight the results for these two alternative designs throughout our analyses.

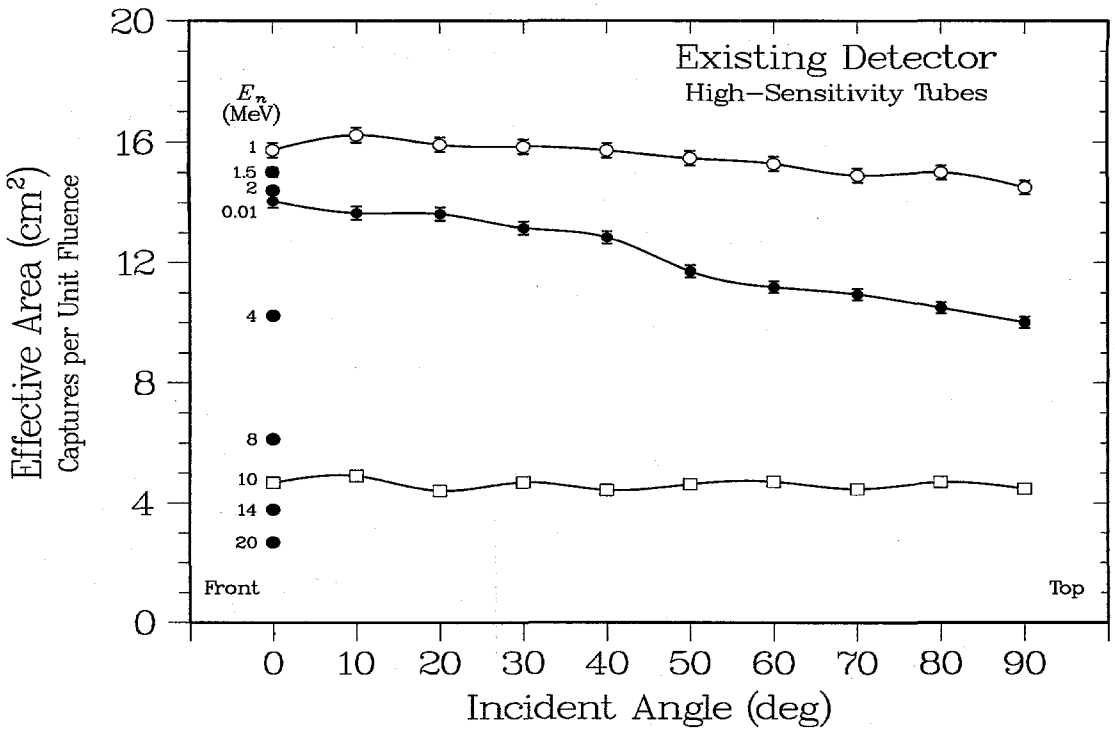

Figure 3.13. Available data on the angular distribution of the effective area for the existing nearly spherical detector.

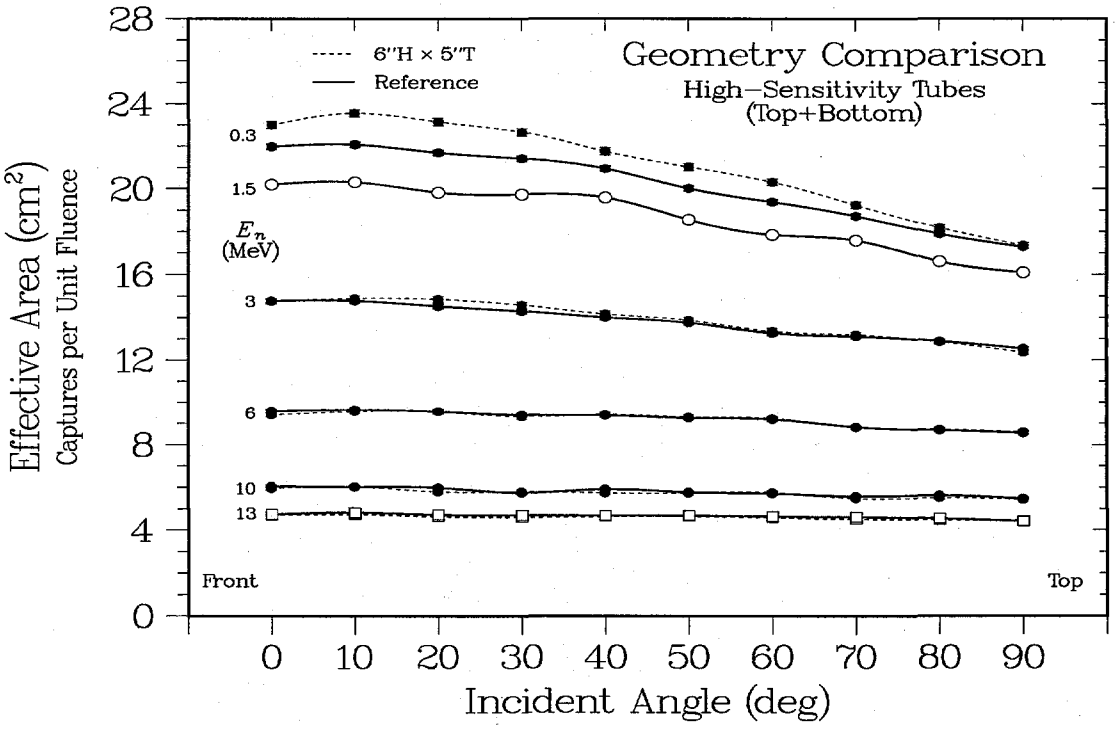

Figure 3.14. Effect of small changes in the tube positions from those assumed in the reference design (see Figure 3.3).

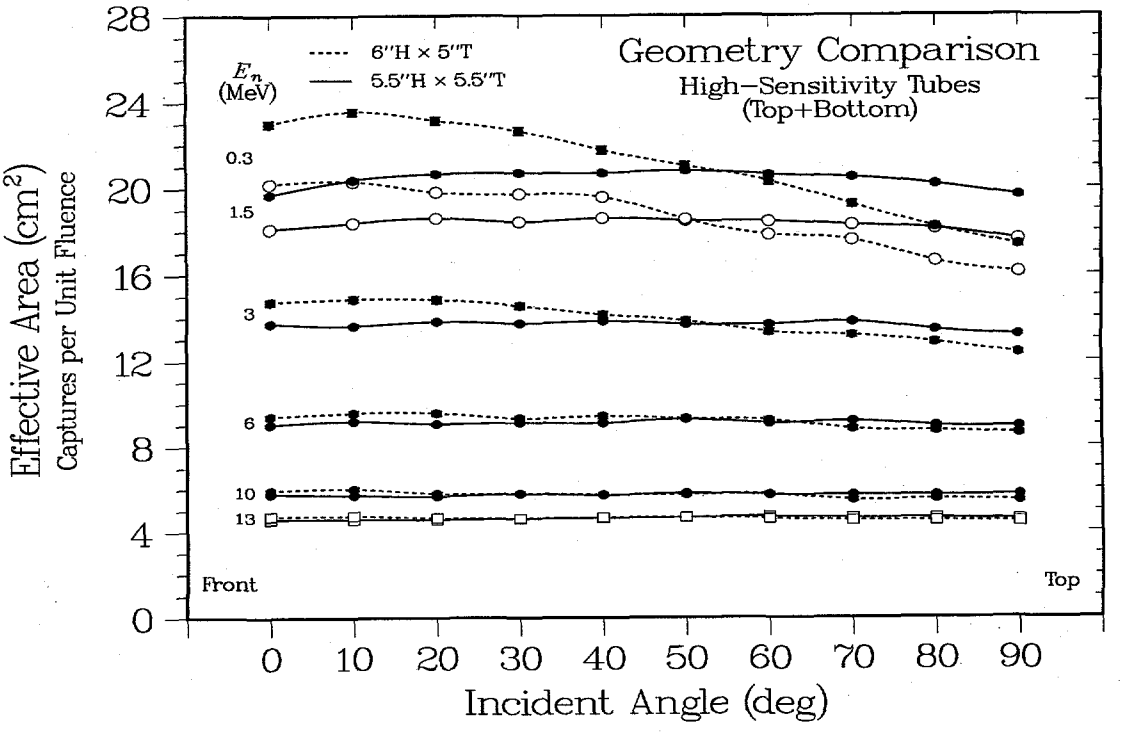

Figure 3.15. Comparison of the front-to-top angular responses of two alternative detector designs, each slightly different from the reference detector (Figure 3.3).

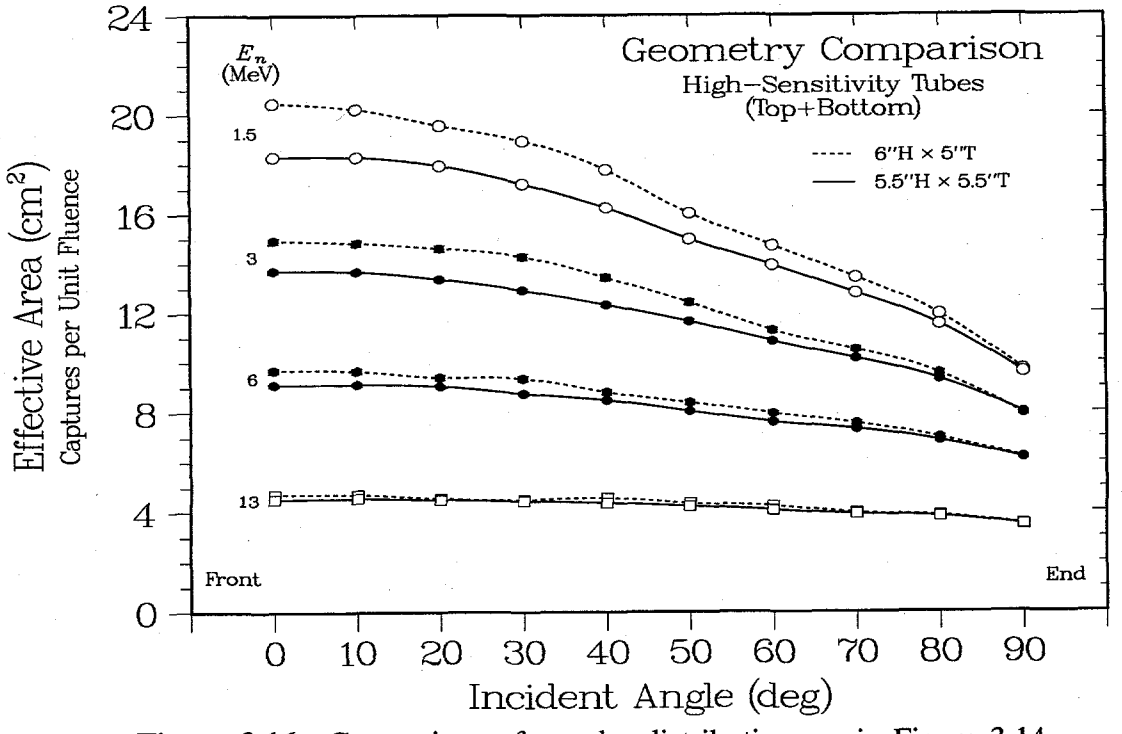

Figure 3.16. Comparison of angular distributions as in Figure 3.14, but for front-to-end illumination of two slightly different detector designs (see also Figure 3.9).

3.5. Discussion

Geometry Issues. The proposed detector differs from the existing design in two obvious features: the proposed rectangular shape versus the existing spherical one, and the use of multiple tubes in the existing detector to provide different sensitivities. The difference in shape arises from the anticipated constraints of the eventual satellite platform, and the difference in dynamic range relates to the different missions for the existing operational system versus the present developmental program to design and test a possible replacement. In particular, although the BF_3 tubes used for the existing medium- and low-sensitivity channels should be avoided in future detectors, as yet no acceptable alternative has been identified. Our two-detector files therefore include an additional central tube, but only as a placeholder. In the one-detector files discussed in this report the roles are reversed: the central tube becomes the high-sensitivity element, and the top and bottom tubes are ignored.

4. ANALYTICAL MODELING

Overview. As shown by the calculations in Chaps. 2 and 3, it can be very difficult to unravel the effects of changes in more than a single parameter, especially if both the energy and angular dependence are considered. Fortunately, we have been able to develop a simple and surprisingly successful model that relates a change in each of the detector parameters to its effect on the overall effective area. Section 4.1 describes the procedures for creating the MCNP input files for mapping the parameter values and collecting the results from the corresponding MCNP output files. The result is a large database of input parameter values for different detector configurations and the corresponding effective areas and angular slopes. Section 4.2 explains the assumptions and operation of the model used to organize this database and separate the effects of the individual parameters, and Sec. 4.3 summarizes the results of the entire process.

4.1. Database Construction

Input Processing. As discussed in Chap. 3, each of the detector configurations involves 100 separate MCNP calculations, one for each of 10 angles at each of 9 energies, plus 10 VOID calculations for source normalization. Obviously, producing 100 files by hand for every configuration (over 500 total) would be out of the question. Instead, a combination of FORTRAN and VMS job-control coding was used to generate the input files and then run each set of energy and angle calculations almost automatically. As examples, **Table 4.1** shows the sections of FORTRAN programming for generating the front-to-top and front-to-end files for the detector geometry in Table 3.1. Only these small sections of the program need to be modified to create the 100 files for a new configuration.

Table 4.1. Input File Parameters

```
c input parameters for two-tube front-to-top files
       nps=4e5          !number of incident neutrons
       cl=2.54          !added top slab height for 6" detector
       ct=0.            !added back and front slab depths for 5" detector
       zmax=10.15       !z-axis half-length (8")
       radt=2*0.635     !radius of bot and top tubes (1" diam)
       radc=0.5*radt    !radius of cen tube (1/2" diam)
       xoft=0*radt      !front-back offset of bot and top tubes (0")
       xofc=-4*radt     !front-back offset cen tube (-1")
       yspt=4*radt      !up-down separation of bot and top tubes

c input parameters for two-tube front-to-end files
       nps=2.5e5        !number of incident neutrons
       cl=3.01*2.54     !added end length for 8" detector
       ct=0*2.54/2      !added back and front slab depths for 5" detector
       zmax=6*2.54/2    !half-height (total 6" height)
       radt=1.27        !radius of bot and top tubes (1" diam)
       radm=0.5*radt    !radius of middle tube (1/2" diam)
       xoft=-0*radt     !offset of bot and top tubes toward front
       xofm=-4*radt     !offset of middle tube toward back (-1")
       zspt=4*radt      !up-down separation of bot and top tubes
       pcn=-5.34e-4     !center tube pressure (10 atm)
       pud=-5.35e-4     !up/down tube pressure (4 atm)
```

Output Processing. Once a set of 100 MCNP calculations for a particular configuration was complete, another set of FORTRAN/VMS routines scanned the input and output files to extract detector parameters, incident fluence normalizations, and resulting capture yields; checked for consistency between the inputs and outputs; and produced a summary file. Overall summaries were then accumulated for the four major combinations of front-to-top or front-to-end illumination for either one- or two-tube detectors. These tables of fluences and yields were used to generate the required database of the effective areas and slopes as functions of all the detector parameters. Eventually, this database contained results for 569 different detector configurations. The majority (344) were for front-to-top illumination of either two-tube (190) or one-tube (154) designs; the remaining 125 front-to-end combinations included 73 two-tube and 52 one-tube cases.

4.2. Modeling Approach

Effective-Area Function. Our steps in analyzing the calculation database were to

(1) identify a set of independent variables that separately determine the effective area and its slope,
(2) explicitly identify the relationships between effective area and detector mass and between angular uniformity and detector geometry, and
(3) determine how changes in each variable affect the overall effective area and slope.

The first step assumes that the effective area can be divided into independent components. We have taken the simple approach that A_{eff} can be written as a *product* of separate functions for each of the individual parameters:

$$A_{eff} = m(M) \times p(P) \times r(R) \times x(X) \times y(Y) \times h(H) \times t(T) \times l(L) \ldots , \quad (4\text{-}1)$$

where M is the plastic mass (polyethylene plus scintillator); P is the ^{3}He gas pressure; R is the tube radius; X and Y are the front/back offset and the vertical separation of the high-sensitivity tubes; and H, T, and L are the detector height, thickness, and length. Note that some of the parameters are connected; for example, changing the detector height also changes the mass. Although both changes affect the effective area, the mechanisms are different: increasing the height increases the projected area, but increasing the mass generally increases the amount of moderation, which in turn increases the detection efficiency. Similarly, an increase in the tube radius will both increase the capture probability and decrease the amount of moderation, and these effects tend to cancel one another. The use of coupled mass and size factors is also related to our second step; in Eq. (4-1) the mass dependence of A_{eff} is contained solely in the lead $m(M)$ term. To emphasize this distinction, only A_{eff} and $m(M)$ are given in absolute units (cm^2 and kg); all other factors are dimensionless multipliers that provide the fractional change from the reference configuration in Table 3.1, with moderator dimensions of 8″×6″×5″ and tubes with 1″ diameters and 4-atm pressures.

Slope Functions. Our model for the slope S of the A_{eff} angular distribution follows a similar pattern, except we assume a *sum* of separable functions:

$$S = r(D_I) + s(X_I) \ldots . \quad (4\text{-}2)$$

As stated in step 2, this approach emphasizes the importance of symmetry in the projected area for rotations about each direction. For example, for a one-tube detector with equal height and thickness, the projected areas in the front and top directions are equal, $H \times L = H \times T$, so the effective areas for these two directions should also be the same. Conversely, for different height and thickness values, the slope of the front-to-top angular distribution should be pro-

portional to the difference between the projected areas: $S \propto (HL–TL)$. To obtain a dimensionless quantity, we normalize this difference to the average area for the rotation, that is, the projected area at the diagonal, $L\times(H^2+T^2)^{1/2}$. Accordingly, the D_I parameters in the first S term in Eq. (4-2) are calculated by subtracting the 0° (height) and 90° (thickness or length) dimensions and then normalizing to the intermediate value (diagonal). Front-to-top illumination uses $D_H = (H–T)/(H^2+T^2)^{1/2}$, and front-to-end illumination uses $D_L = (L–T)/(L^2+T^2)^{1/2}$. Similarly, the tube-offset parameters X_I and Y_I in the second term are obtained by dividing the corresponding X and Y offsets by the appropriate detector diagonals, e.g., $X_L = X/(L^2+T^2)^{1/2}$. Note that S is a function of dimensionless quantities, and its result is also dimensionless; specifically, S is the fractional change in the effective area $\Delta A_{\text{eff}}/A_{\text{eff}}$ per unit angle (in radians).

Decoupling Procedure. The third step requires developing a technique for identifying the effect of changes in each of the detector parameters. We identify the i^{th} detector configuration in our data set by its parameters M_i, P_i, R_i, X_i, Y_i, H_i, T_i, and L_i, and we use the resulting MCNP capture and fluence values to calculate the resulting $A_{\text{eff},i}$ value. To determine the effects of the individual parameters, we solve Eq. 4-1 for each parameter in turn and use the resulting expression to correct the $A_{\text{eff},i}$ value for the variation of each of the other parameters away from their reference value, as follows:

$$\begin{aligned} m_i(M_i) &= A_{\text{eff},i}\,[p_a(P_i)\times r_a(R_i)\times x_a(X_i)\times y_a(Y_i)\times h_a(H_i)\times t_a(T_i)\times l_a(L_i)]^{-1} \\ p_i(P_i) &= A_{\text{eff},i}\,[m_a(M_i)\times r_a(R_i)\times x_a(X_i)\times y_a(Y_i)\times h_a(H_i)\times t_a(T_i)\times l_a(L_i)]^{-1} \\ \ldots &= \qquad\qquad \ldots \\ l_i(L_i) &= A_{\text{eff},i}\,[m_a(M_i)\times p_a(P_i)\times r_a(R_i)\times x_a(X_i)\times y_a(Y_i)\times h_a(H_i)\times t_a(T_i)]^{-1}\ . \end{aligned} \tag{4-3}$$

The source of the critical m_a, p_a, …, l_a functions will be apparent in a moment. For the i^{th} configuration, these adjustments give us a set of corrected parameters m_i, p_i, r_i, x_i, y_i, h_i, t_i, and l_i. When each of the corrections m_i, p_i, …, l_i is plotted as functions of the original parameters M_i, P_i, …, L_i, the resulting relations reveal the effect of varying each parameter independently. We then summarize these relations by using a spline interpretation to obtain smoothed functions $m_a(M_i)$, $p_a(P_i)$, …, $l_a(L_i)$ as

$$\begin{aligned} m_a(M_i) &= \langle m_i(M_i)\rangle \\ p_a(P_i) &= \langle p_i(P_i)\rangle \\ \ldots &= \ \ldots \\ l_a(L_i) &= \langle l_i(L_i)\rangle\ . \end{aligned} \tag{4-4}$$

These smoothed functions provide the adjustments to the $A_{\text{eff},i}$ values in Eq. (4-3), thereby setting up an iterative cycle that aims to find the best agreement between the actual $A_{\text{eff},i}$ values and the corresponding model predictions:

$$A_{\text{eff},i}^{\,a} = m_a(M_i)\times p_a(P_i)\times r_a(R_i)\times x_a(X_i)\times y_a(Y_i)\times h_a(H_i)\times t_a(T_i)\times l_a(L_i)\ . \tag{4-5}$$

A similar procedure is followed for the slope function. Taken together, these three steps provide independent functions for all the variables and explicitly recognize the central roles of detector mass and geometry.

4.3. Discussion

Modeling. The results in Chaps. 2 and 3 make it clear that understanding the effects of the different parameter variations will be a difficult problem. The analysis steps outlined in this chapter address this problem, but only the results will show whether our approach is successful. Chapters 5 and 6 carry out the proposed analyses for the cases of two-tube and one-

tube detectors, respectively, and the results for both the effective area and the slope are very encouraging. Specifically, the separable A_{eff} and S functions assumed in Eqs. (4-1) and (4-2) make it easy to determine the effects of variations in the different variables, and the results reproduce the database of individual $A_{eff,i}$ and S_i values for a wide range of detectors to within about 10%. Chapter 7 follows by demonstrating that the functions for the one-tube and two-tube detectors can be combined to provide a single generic model for both detector types, and Chap. 8 uses the results from all the analyses to propose a final configuration that optimizes both the effective area per unit mass and the uniformity of the angular response. Although our simple approach may not be valid for all possible moderated ^{3}He detectors, it is at least able to explain the results for cases with parameters near this optimum design.

5. TWO-TUBE DETECTOR

Overview. Although this chapter focuses on calculations for the two-tube version of our particular detector, the discussion also serves to demonstrate our analytical approach for separating the effects of different parameter changes. If successful, this separation also provides both the basis for a physical interpretation of the detector's operation and the template for our subsequent analyses of other detector designs. Our discussions will therefore be unusually thorough. Section 5.1 covers the magnitude and angular dependence of the effective areas for a front-to-top rotation of the source plane about the detector's long axis, and Sec. 5.2 provides the same analyses for the front-to-end source rotation. Section 5.3 covers the detector's ability to use differences in count rate for the two high-sensitivity tubes to determinate the source direction, and Sec. 5.4 provides a summary of the entire chapter.

5.1. Front-to-Top Illumination

MCNP Calculations versus Analytical Model. The success of our analytical model for effective areas is demonstrated by the agreement shown in **Figure 5.1** between the actual database effective areas $A_{\text{eff},i}$ and the corresponding $A_{\text{eff},i}^{a}$ predictions from Eq. (4-5). Two sets of comparisons are shown, one for high energies (12–14 MeV) and the other for relatively low energies (1–2 MeV). These calculations include a wide variety of different parameter values, with masses varying from 2 to 8 kg, gas pressures from 1 to 20 atm, tube radii from 0.4 to 2.5 cm (0.2″ to 1.0″), front/back offsets from –4 to +5 cm (–1.6″ to 2.0″), and tube separations from 2 to 9 cm (0.8″ to 3.5″). In addition, detector heights vary from 11 to 20 cm (4″ to 8″), lengths from 20 to 25 cm (8″ to 10″), and thicknesses from 10 to 20 cm (4″ to 8″). Even when multiple parameters are varied simultaneously, the simple analytical model is able to reproduce the actual area, usually within much better than 10%. The small + and × symbols show the individual A_{eff} values, and the small ○ and □ symbols show the interpolation averages. Also shown are larger symbols for the particular values for the 6″×5″ (○, □) and 5.5″×5.5″ (●, ■) detectors and the estimated values for the existing detector (◇), which were calculated from the results in Table 2.1. (Because there are no predictions for this detector, its values are simply plotted along the diagonal.)

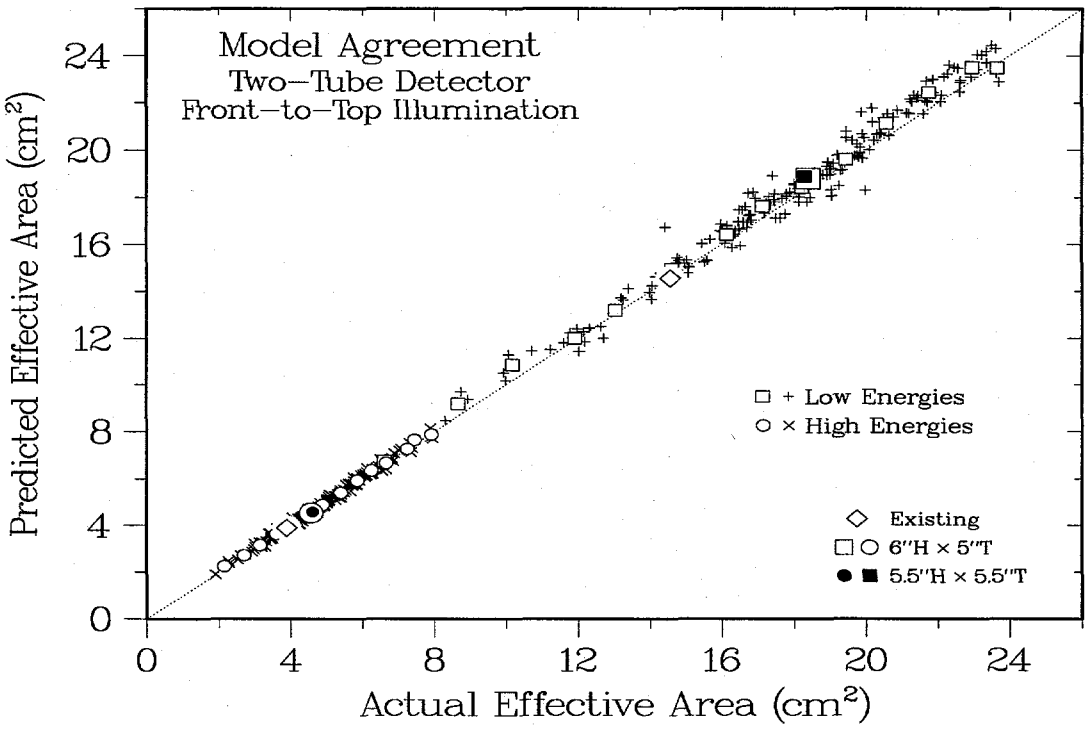

Figure 5.1. Comparison between the actual MCNP effective areas and the corresponding predicted values obtained from the analytical model, in this case for front-to-top illumination of a two-tube detector. The individual data points include the effects of variations in all parameters, including polyethylene mass, ^{3}He gas pressure, tube radius, and so on. The open symbols are interpolated average values.

Mass Dependence. The major independent parameter affecting the effective area is the plastic mass (which includes one half of the four scintillator masses), whose effects are shown explicitly in **Figure 5.2**. The mass dependence is clearly asymptotic for the low-energy data, but it shows no signs of saturating at the higher energies. For reference, the specific results for the two alternative geometries from Sec. 3.4 (6″×5″ and 5.5″×5.5″) are shown at mass values just below 3 kg. Note also that the estimated value for the existing detector is in good agreement at high energies, but it falls slightly below the trend of the present low-energy results. A likely explanation for the low-energy discrepancy is the effect of the nearby low-sensitivity tubes in the existing detector. Nevertheless, the most important result in the figure is a simple mass scaling that is independent of all other parameter variations.

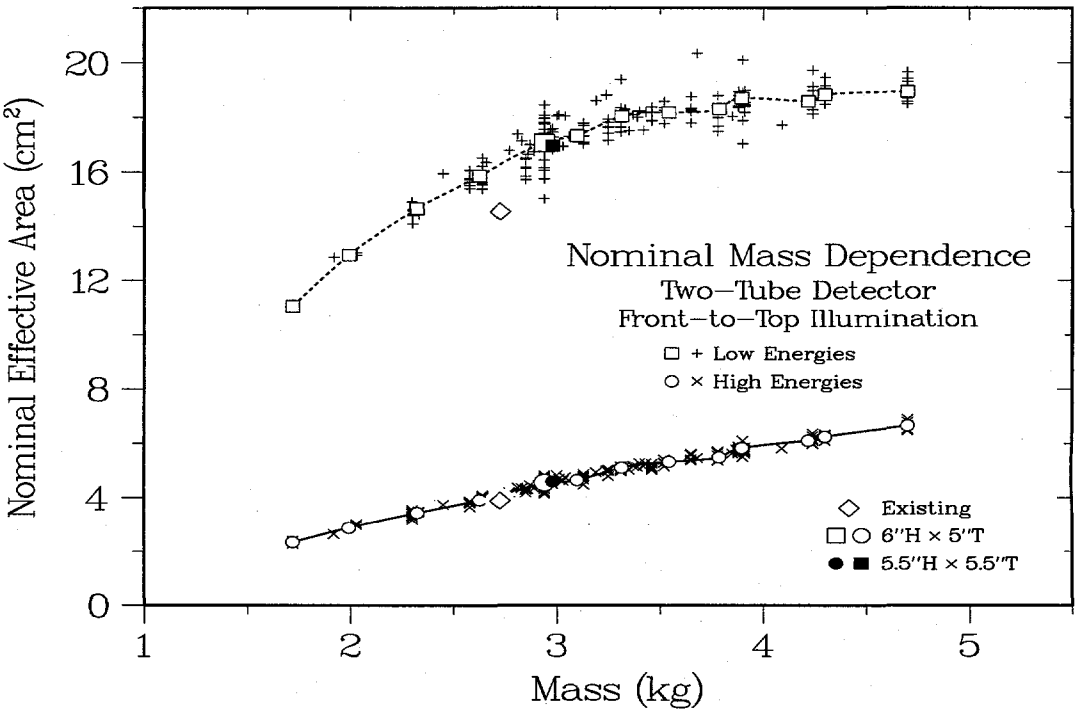

Figure 5.2. Mass dependence of the effective areas for the nominal two-tube detector at low and high neutron energies. The detector uses two 1″ diameter (1.27-cm radius), 4-atm ^{3}He tubes that are separated by 2″ (5.08 cm) center to center and placed along the vertical centerline.

Tube Pressure and Radius. The mass dependence in Figure 5.2 assumes the reference detector arrangement, which uses 1″ diameter tubes filled to a ^{3}He pressure of 4 atm. A simple change involves varying the gas pressure, which produces the results shown in **Figure 5.3**. The normalization to unity at a pressure of 4 atm indicates that the gas factor multiplies the basic mass factor in Figure 5.2. For pressures below the reference 4-atm value, the efficiency decreases rapidly; from 4 to 10 atm the increase is more gradual; above 10 atm the increase appears to have almost saturated. In our previous study[4] the pressure dependence was estimated as $P^{1/4}$ (see Figure 2.3), and the present 25% increase from 4 to 10 atm is in good agreement. Finally, note that the same pressure dependence can be used to describe both energy ranges. In contrast, **Figure 5.4** shows that the low- and high-energy radius dependences are slightly different. The low-energy curve is slightly steeper, and the high-energy values show signs of decreasing at the highest values. Similar behavior is seen throughout all our analyses. Finally, **Figure 5.5** shows the result of replacing the pressure and radius parameters with the single gas quantity $Q = P \times R^2$, which provides a total ^{3}He content that incorporates changes in both the pressure and volume simultaneously. The predictions using this single parameter are almost as good as those obtained for the separate analyses.

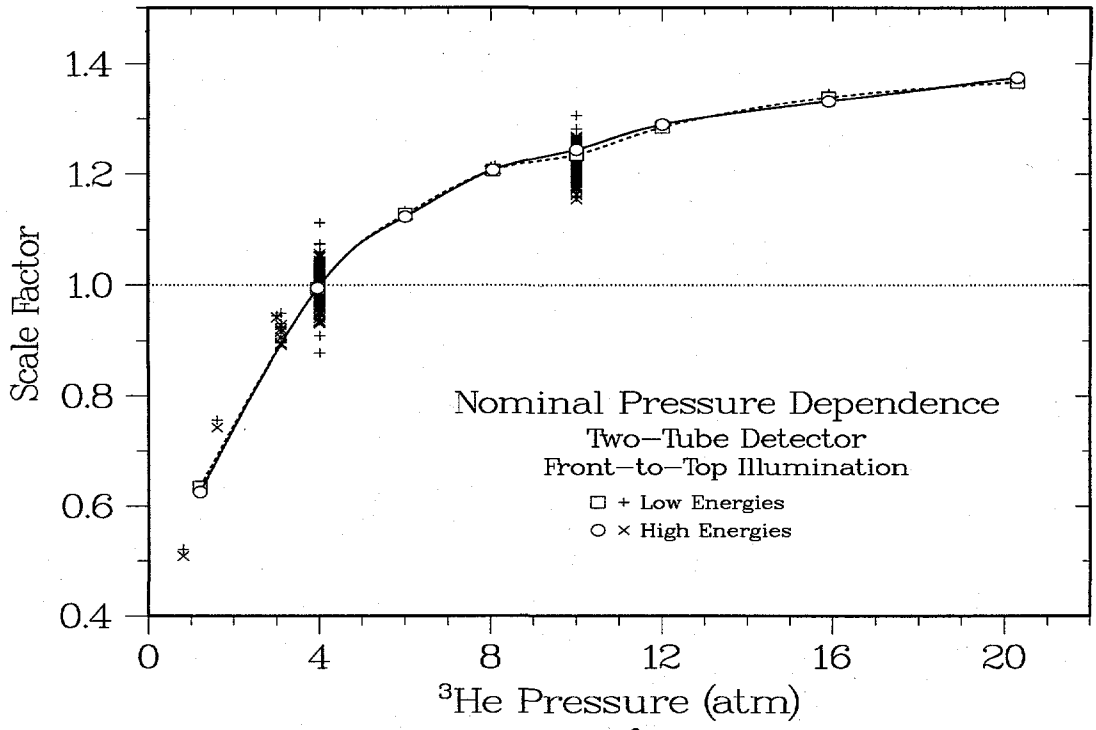

Figure 5.3. Effect of changes in the ^{3}He gas pressure on the nominal effective area for the reference 4-atm detector, which gives a scale factor of 1.0.

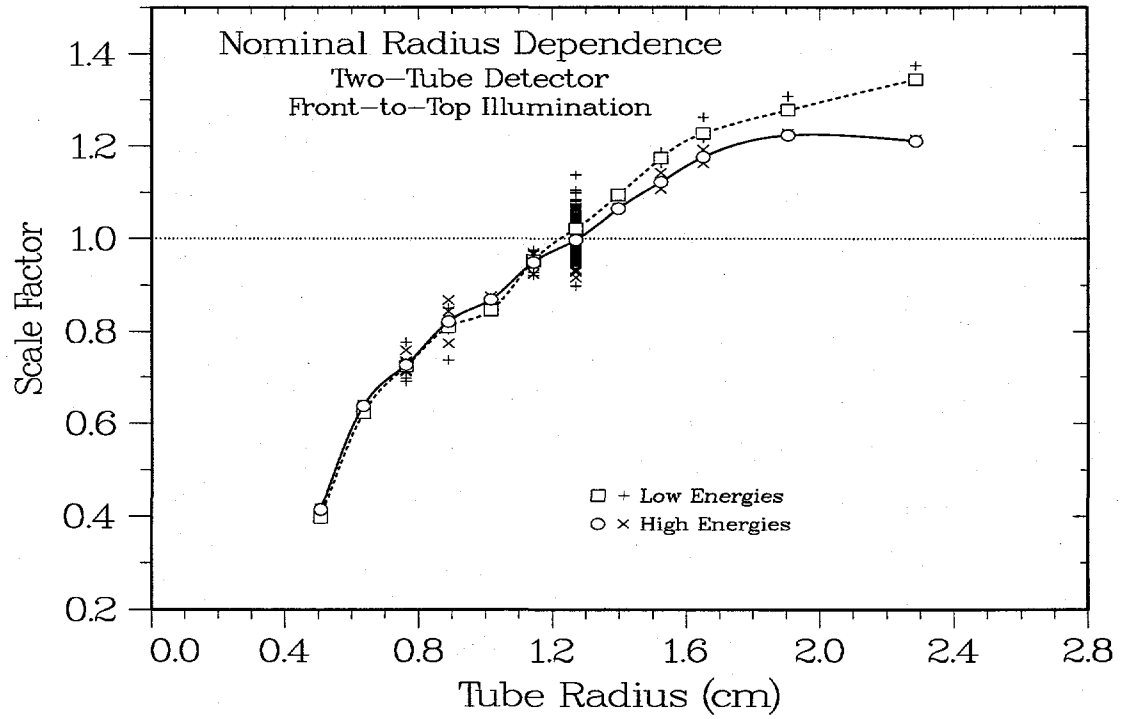

Figure 5.4. Effect of changes in the radii of the ^{3}He tubes on the effective area of the nominal detector, which uses a pair of 1″ diameter ^{3}He tubes illuminated from the front and top.

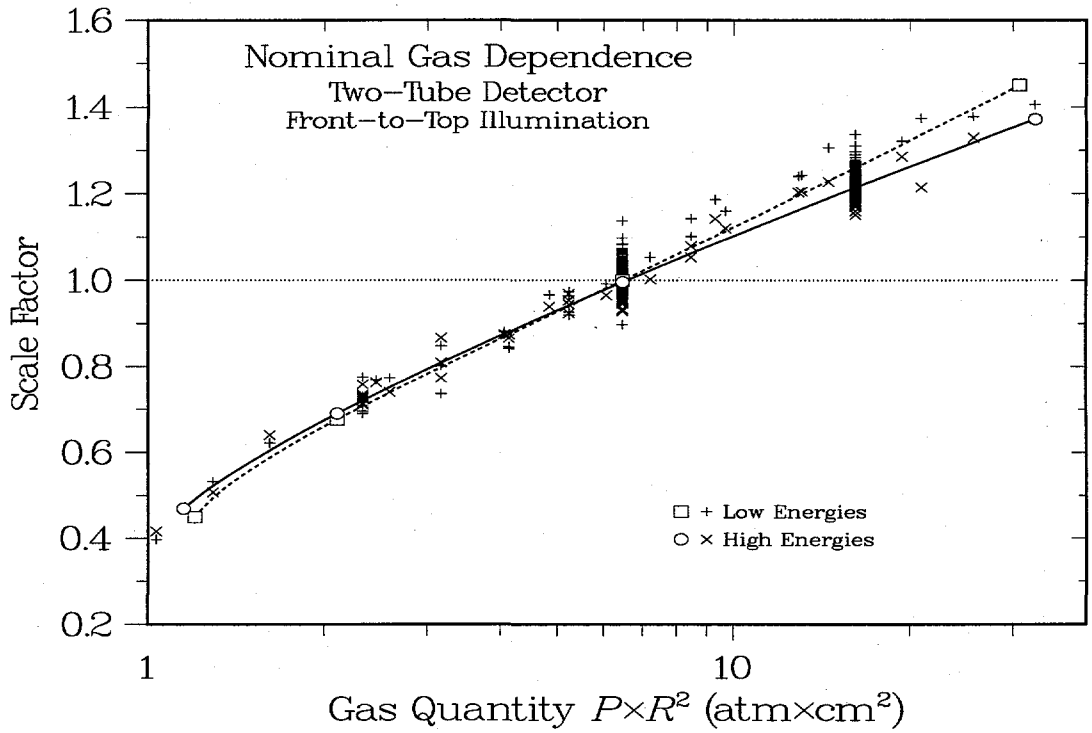

Figure 5.5. Result of combining gas pressure and tube radius into a single quantity $Q = P\times R^2$.

Tube Positions. The two remaining major parameters are the front/back tube offset across the detector and the center-to-center separation between the two tubes. The offset dependence is shown in **Figure 5.6**. At high energies the curve is almost symmetric about the detector center, but at low energies there is a pronounced shift toward the neutron source at the front of the detector. For the separation dependence in **Figure 5.7** it is nevertheless clear that the reference value of 5.08 cm appears to be slightly too low. Because the two alternative geometries use a nonstandard offset of –0.5 cm (instead of 0) and a separation of 5.5 cm (instead of 5.08 cm), their results are highlighted in these two figures. The scatter in the separation results and the erratic structure in the spline function are our first suggestions of residual coupling between parameters; for example, significantly different tube radii may lead to somewhat different tube separation values. On the whole, however, the performance of a wide range of different detector designs can be described very accurately by the use of relatively few parameters.

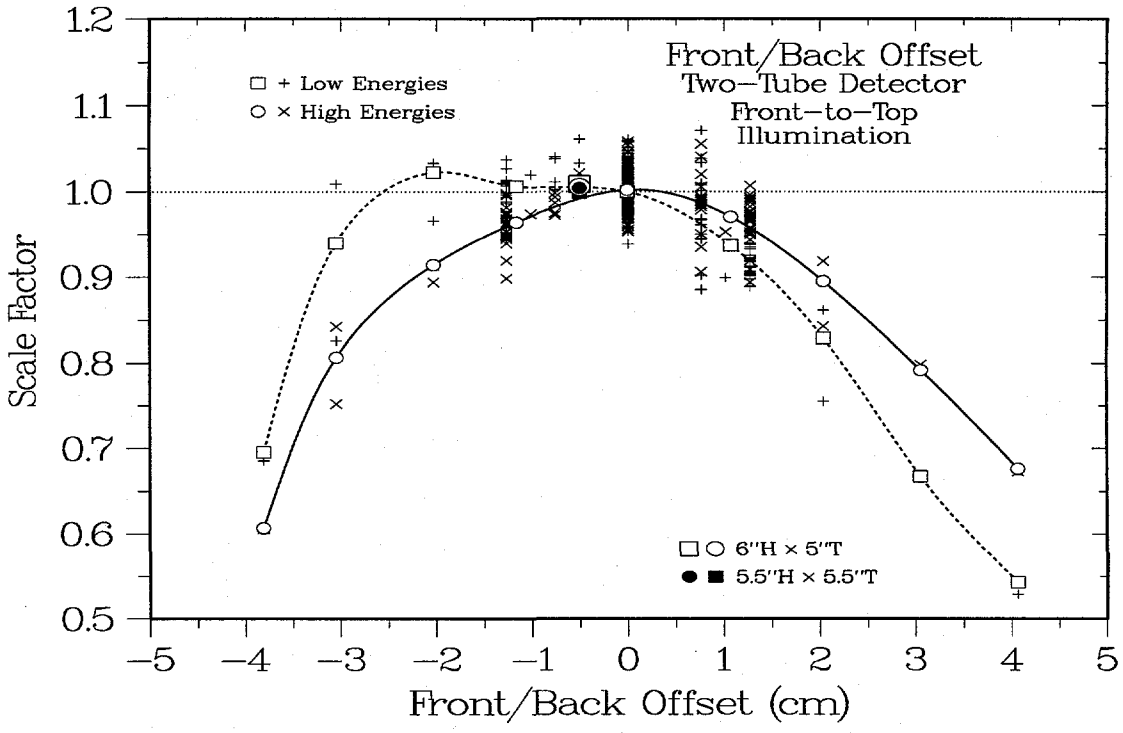

Figure 5.6. Effect of changes in the front/back horizontal offset of the two ^{3}He tubes' centerline from the nominal position in the middle of the detector (0 cm).

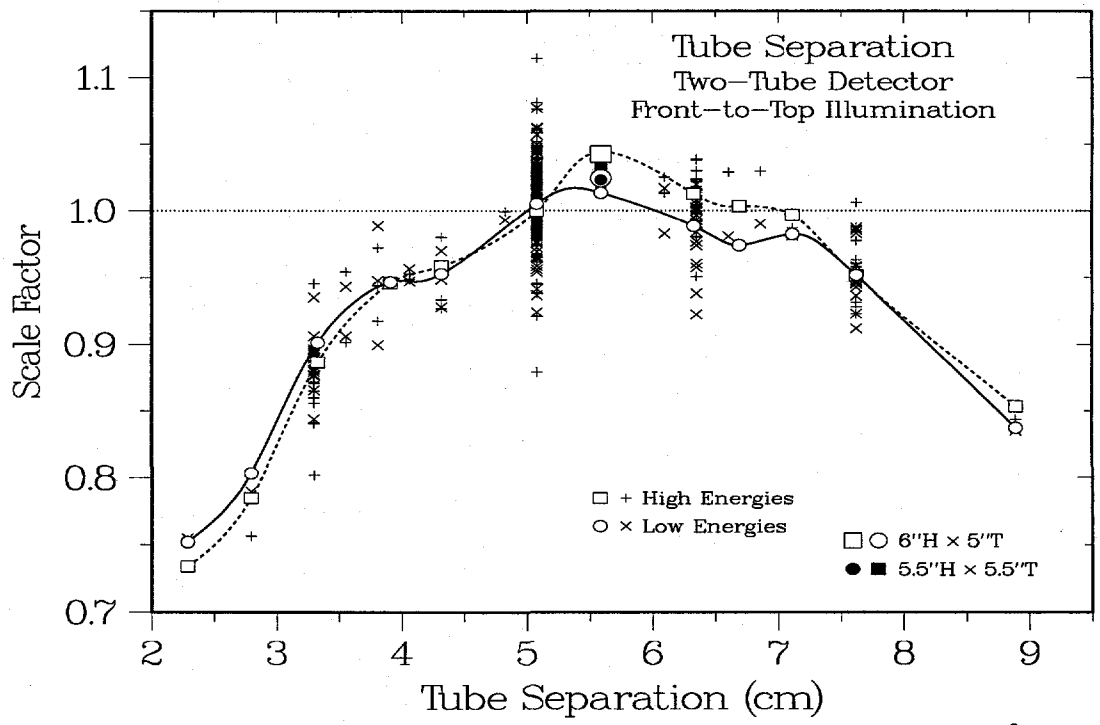

Figure 5.7. Effect of changing the vertical separation of the two ^{3}He tubes from the nominal 2″ (5.08-cm) center-to-center value.

Moderator Height, Length, and Thickness. In principle, the dependence on moderator dimensions should be accounted for by the mass dependence of Figure 5.2. It is therefore reassuring that neither the height, length, or thickness variation shown in **Figure 5.8**, **Figure 5.9**, and **Figure 5.10** indicates any substantial effect on the effective area. Accordingly, the contribution from each of these parameters has been set to 1.0 in our model, and the symbols for the average values shown in the figures are simply the averages of the corrected values.

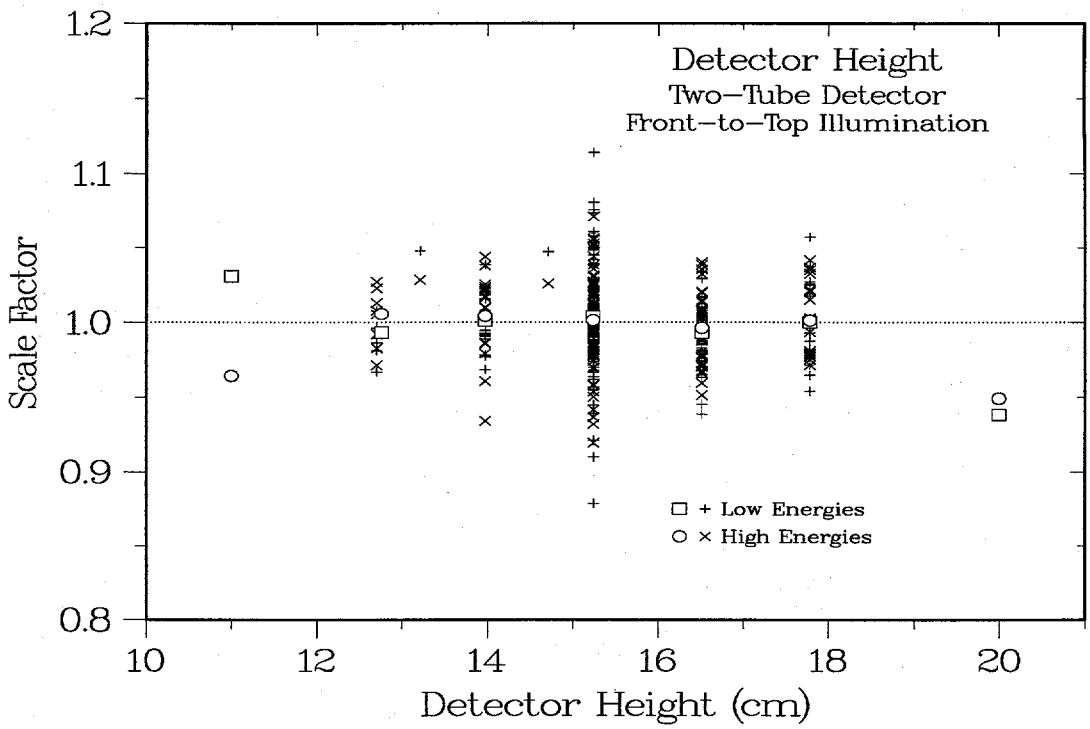

Figure 5.8. Lack of effect of changing the height of the polyethylene moderator from the nominal 6″ (15.2-cm) value.

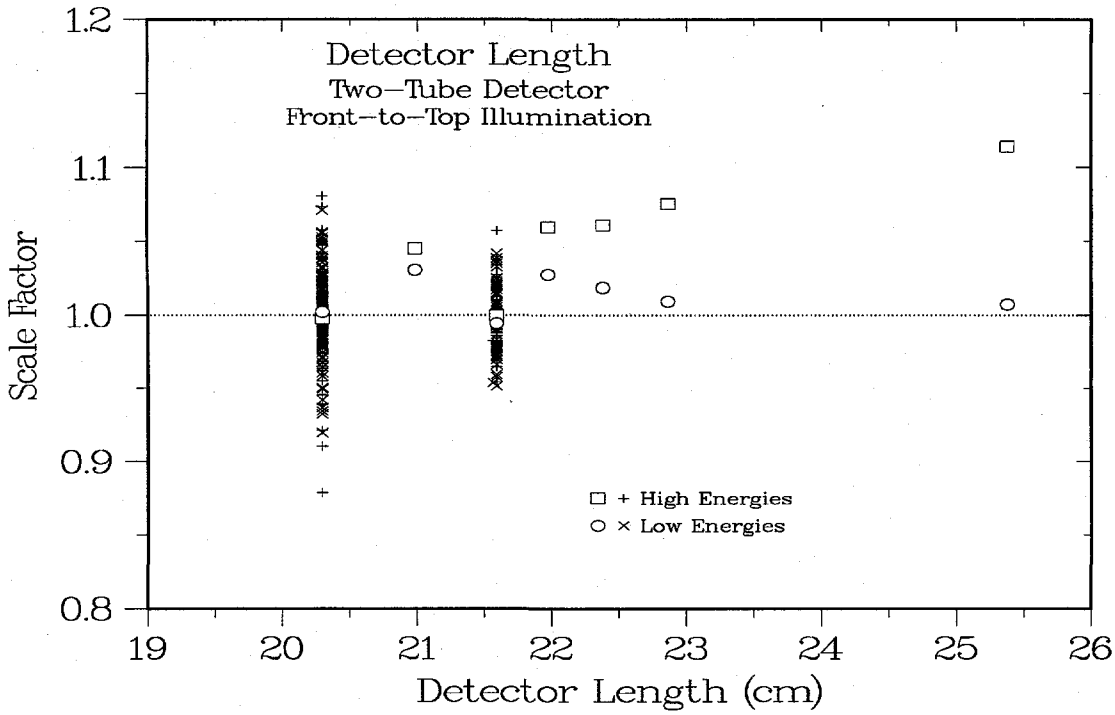

Figure 5.9. Lack of effect of changing the length of the polyethylene moderator from the nominal 8″ (20.3-cm) value.

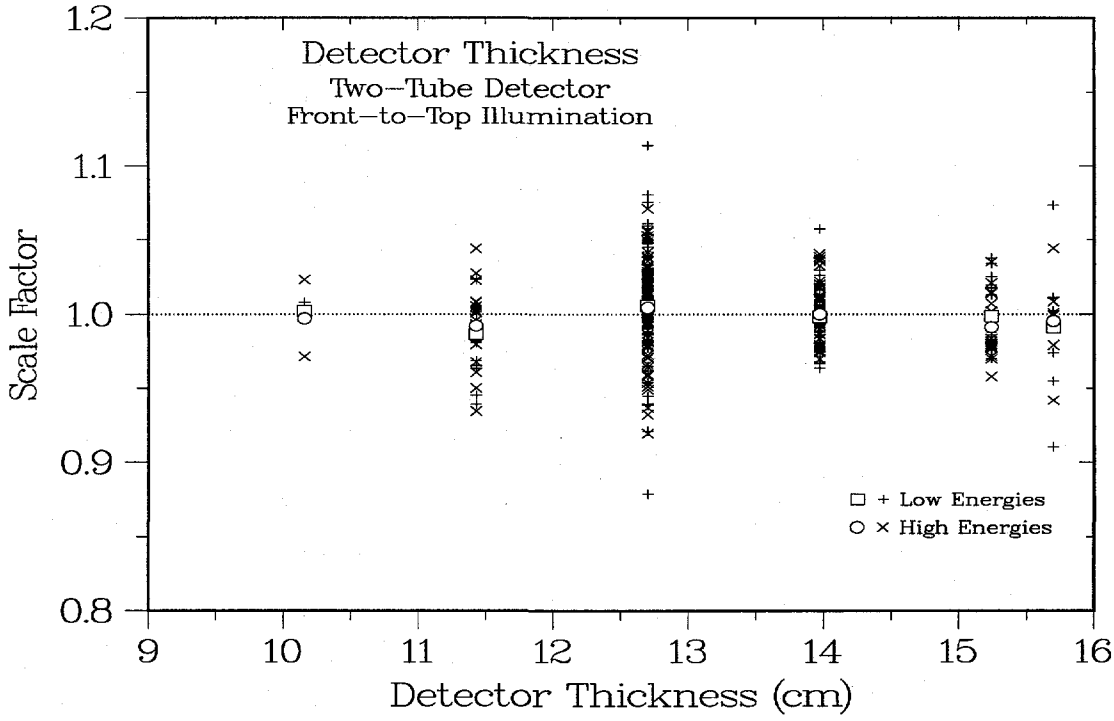

Figure 5.10. Lack of effect of changing the thickness of the polyethylene moderator from the nominal 5″ (12.7-cm) value.

Angular Distribution Slopes. As suggested by the results for the two alternative geometries in Figure 3.15, a symmetric detector cross section leads to a flat angular distribu-

tion. Specifically, the slope for this symmetric case is almost zero, but the slope is clearly nonzero for the near-identical 6″H×5″T detector and all other nonsymmetric cases. As shown by the comparison between actual and predicted slopes in **Figure 5.11**, our analytical model is able to predict not only the average values of the angle-dependent effective areas but also the average slopes of the angular distributions at different energies. As shown in **Figure 5.12**, most of the slope dependence can be described by a single parameter, the difference between the detector's height and thickness, with only the small correction shown in **Figure 5.13** for the front/back offset of the two tubes. Increasing the detector's aspect ratio increases the slope, but moving the tubes backward decreases the effective areas at the front of the detector and tends to flatten out the distribution. Note that the effects are much larger at low than at high energies, as would be expected for the corresponding mean free paths.

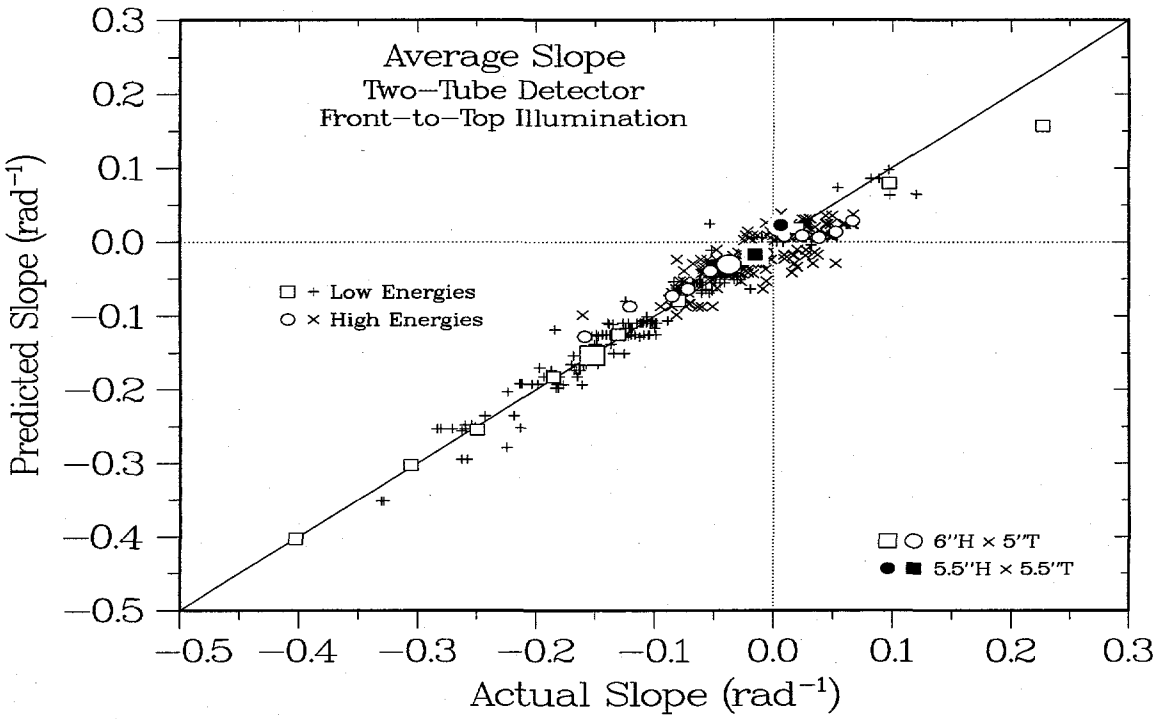

Figure 5.11. Agreement between actual slopes of the individual MCNP angular distributions and the corresponding predictions from the analytical model.

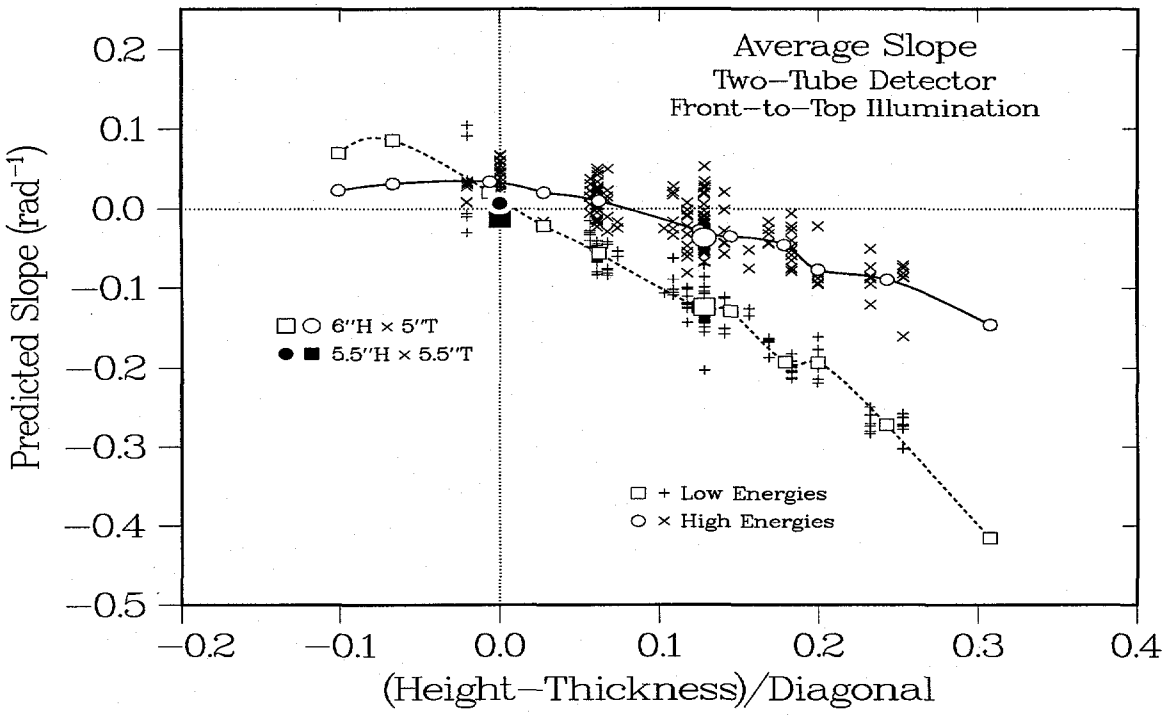

Figure 5.12. Dependence of the predicted slopes on the difference between the height and thickness of the polyethylene moderator.

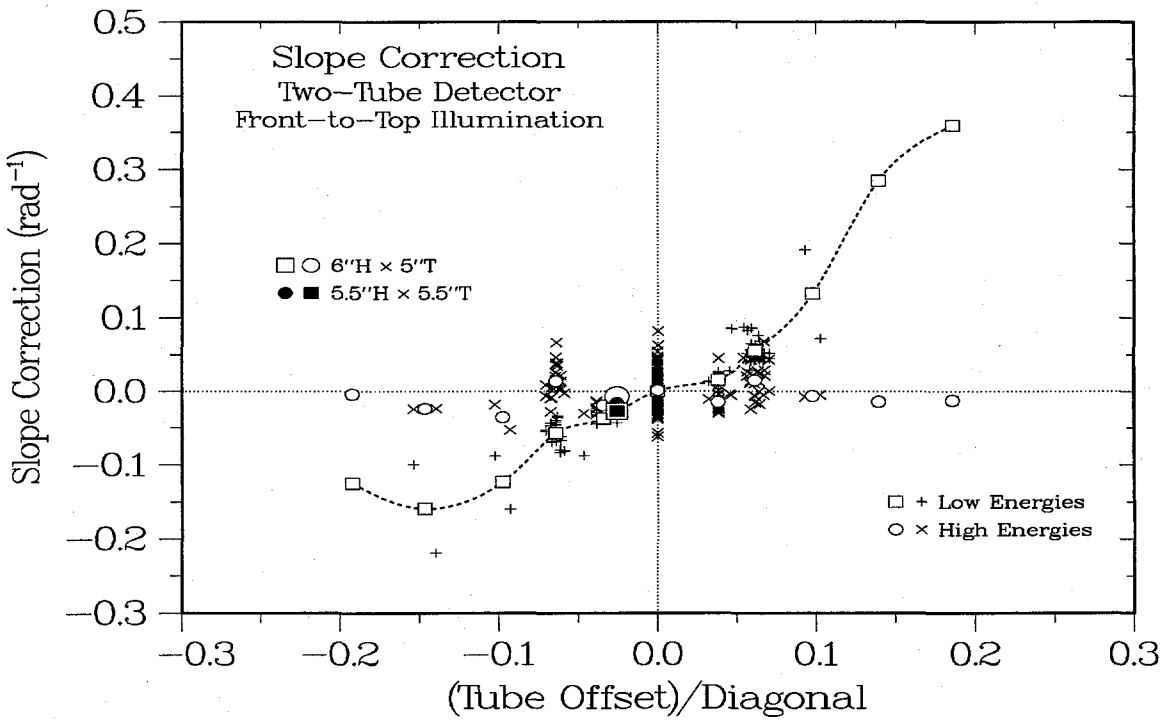

Figure 5.13. Correction to the predicted slope caused by moving the vertical centerline of the detectors toward the front or back of the moderator.

Summary of Front-to-Top Analyses. As shown by the comparisons between the actual and predicted effective areas and slopes in Figure 5.1 and Figure 5.11, the complex da-

tabase of MCNP effective-area angular distributions has been essentially replaced by a set of simple look-up tables. Recalling that the ratio between the two count rates in the high-sensitivity tubes is also a direct function of the incident direction (see Chap. 2), we see that we can completely describe the performance of any detector using only two major parameters (*M* and *Q*) and three minor ones (*X*, *Y*, and *D*). This result is certainly convenient, and it will greatly simplify the evaluation of optimum detector designs to be presented in Chap. 8.

5.2. Front-to-End Illumination

Model Agreement and Mass Dependence. The front-to-end analyses for the two-tube detector follow much the same pattern as the front-to-top studies. The agreement between the actual effective areas and the product-function predictions at low and high energies is shown in **Figure 5.14**, and again the results are excellent. The dependence of effective area on the detector's plastic mass is shown in **Figure 5.15**. Again, the low-energy values begin to show evidence of saturation above 4 kg, with the function reaching a broad maximum just above 5 kg. Although there may be some evidence of decreasing slope in the high-energy values, there is no clear maximum for masses below 7 kg. Once again, the estimated values for the existing detector are in good agreement with the expected values for the corresponding proposed design.

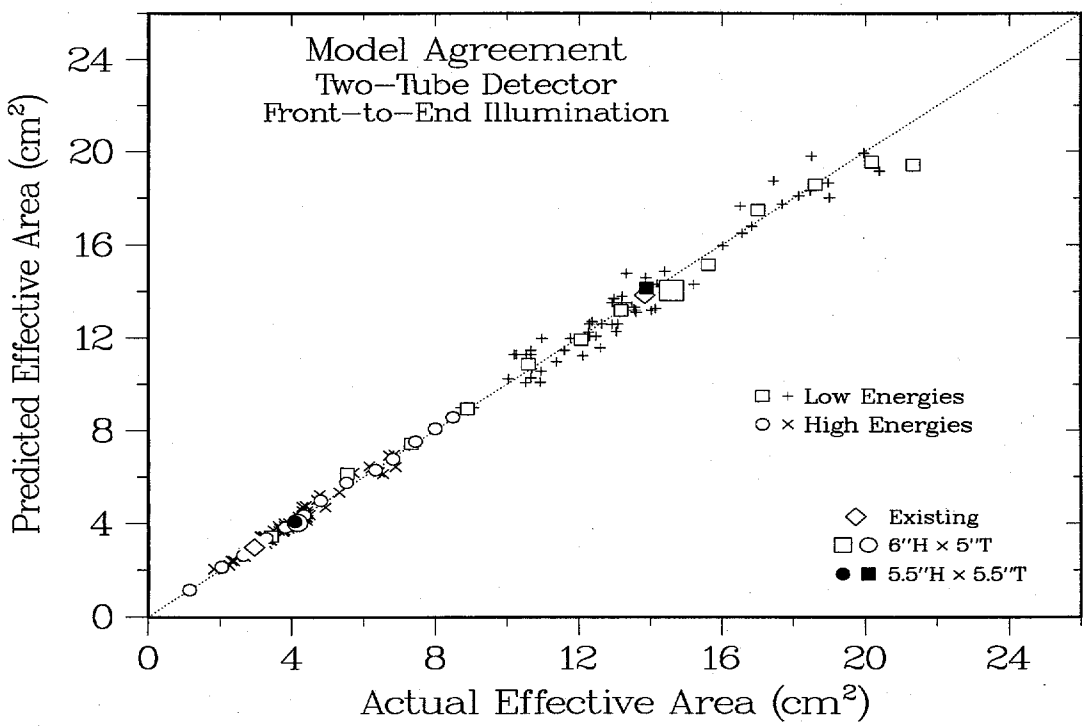

Figure 5.14. As in Figure 5.1, agreement between the actual and predicted effective areas for a neutron detector with two polyethylene-moderated ^{3}He tubes, but now for illumination rotating from the front to the end of the detector.

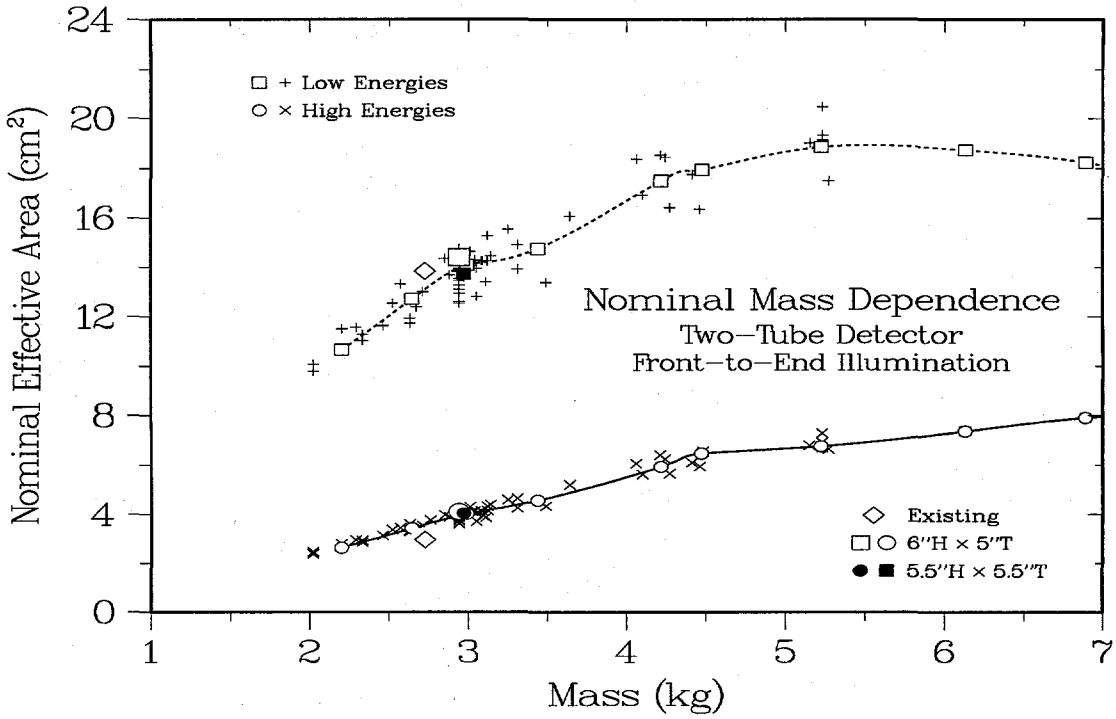

Figure 5.15. As in Figure 5.2, mass dependence of the effective area of a two-tube neutron detector with illumination changing from front-on to end-on.

Changes in Tube Pressure and Radius. The general behavior of the end-on gas parameters is similar to that for the front-to-top results. The pressure variation in **Figure 5.16** is again independent of energy; it rises rapidly below 4 atm and then appears to saturate toward 16 atm, with the increase between 4 and 10 atm again about 20%. As seen in **Figure 5.17**, the radius dependence is also quite steep below the reference value; although there is significant scatter in the data for larger radii, there again appears to be a crossover in the energy dependence near the reference point. Finally, although the data for the combined $P \times R^2$ quantity are quite scattered at the highest values, **Figure 5.18** indicates that the results with the single parameter are apparently no worse than those obtained using two independent functions.

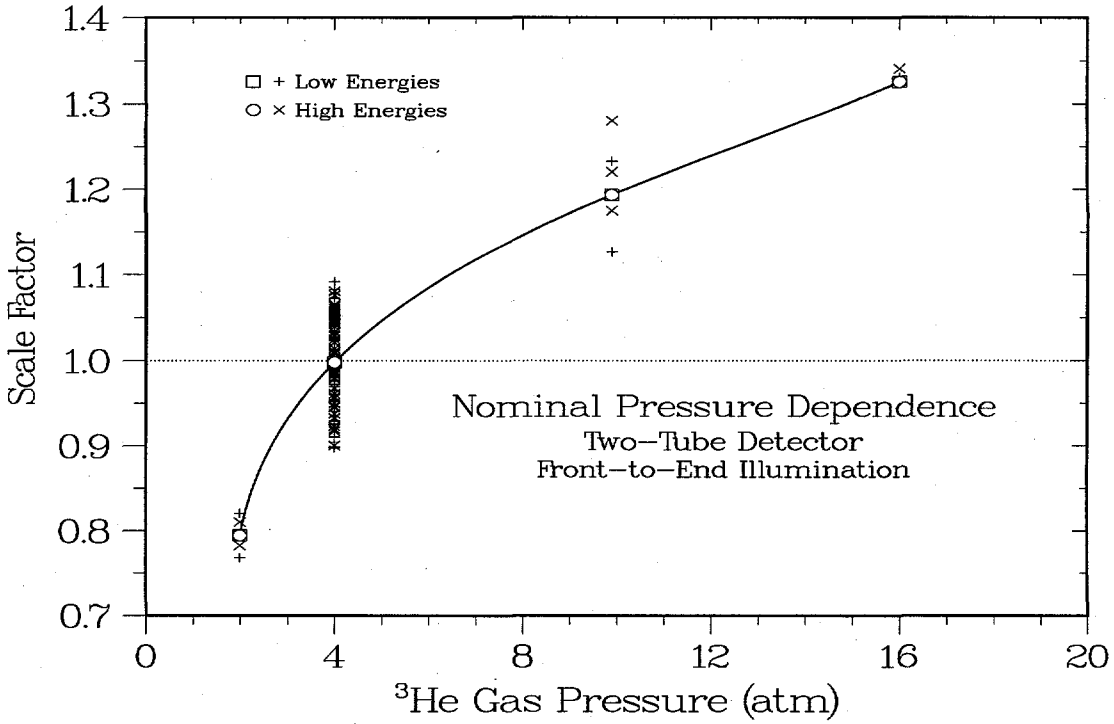

Figure 5.16. As in Figure 5.3, effect of variations in the ^{3}He gas pressure on the effective area of a two-tube detector, but for illumination ranging from the front to the end.

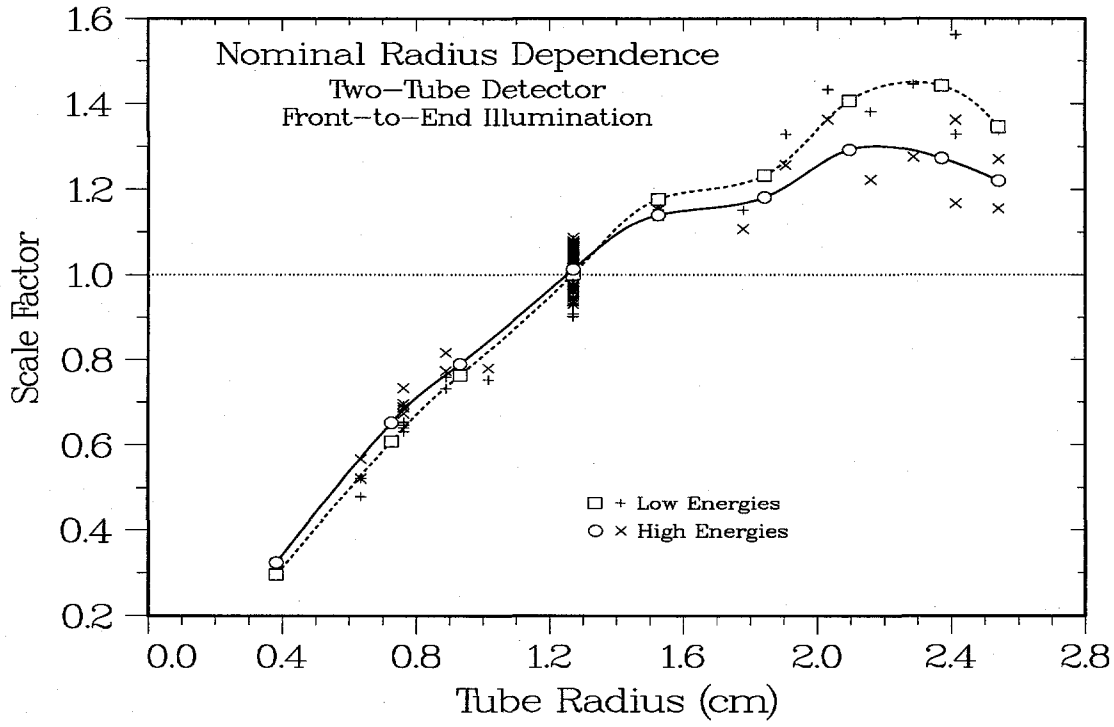

Figure 5.17. As in Figure 5.4, effect of varying the tube radii on the efficiency of a two-tube detector illuminated from the front to the end.

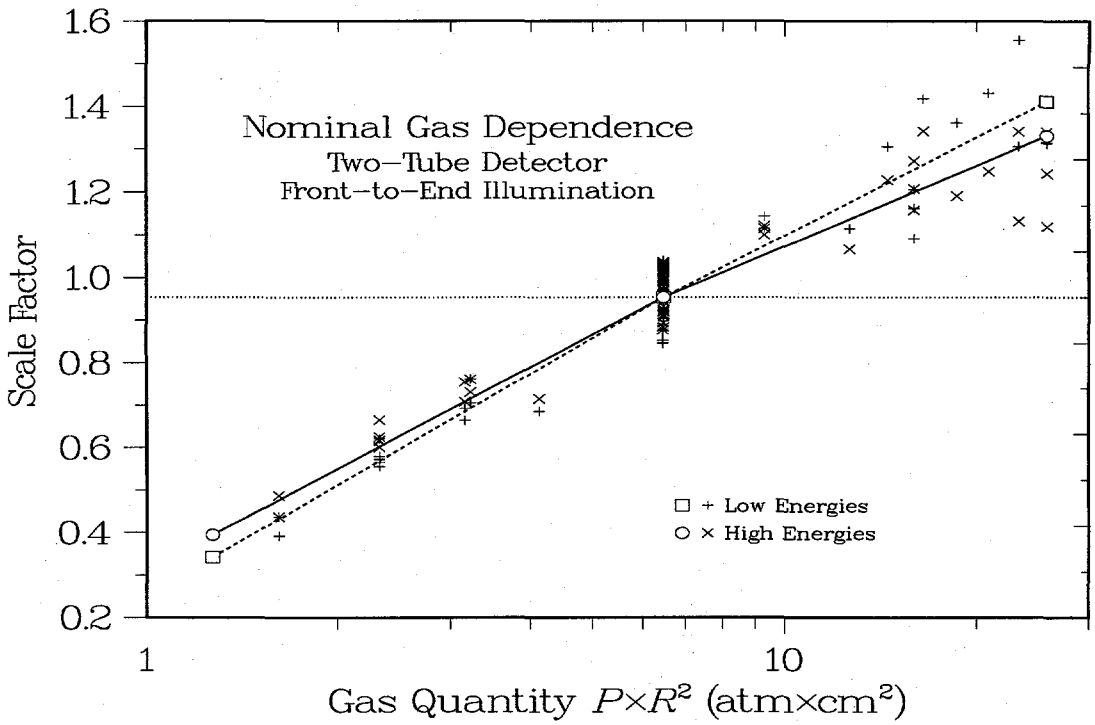

Figure 5.18. As in Figure 5.5, result of combining changes in gas pressure and tube radius into a single parameter.

Changes in Tube Position. As before, the behavior of the front/back offset shown in **Figure 5.19** appears to favor shifting the tubes slightly toward the front of the detector, although here the improvement exists at both low and high energies. No results are shown for the vertical tube separation because the results are consistent with unity, as should be expected from the symmetry of the detector and the angular rotation. As in the front-to-top results, there is also no consistent trend in the data for the detector height, length, or thickness, so no results are shown here.

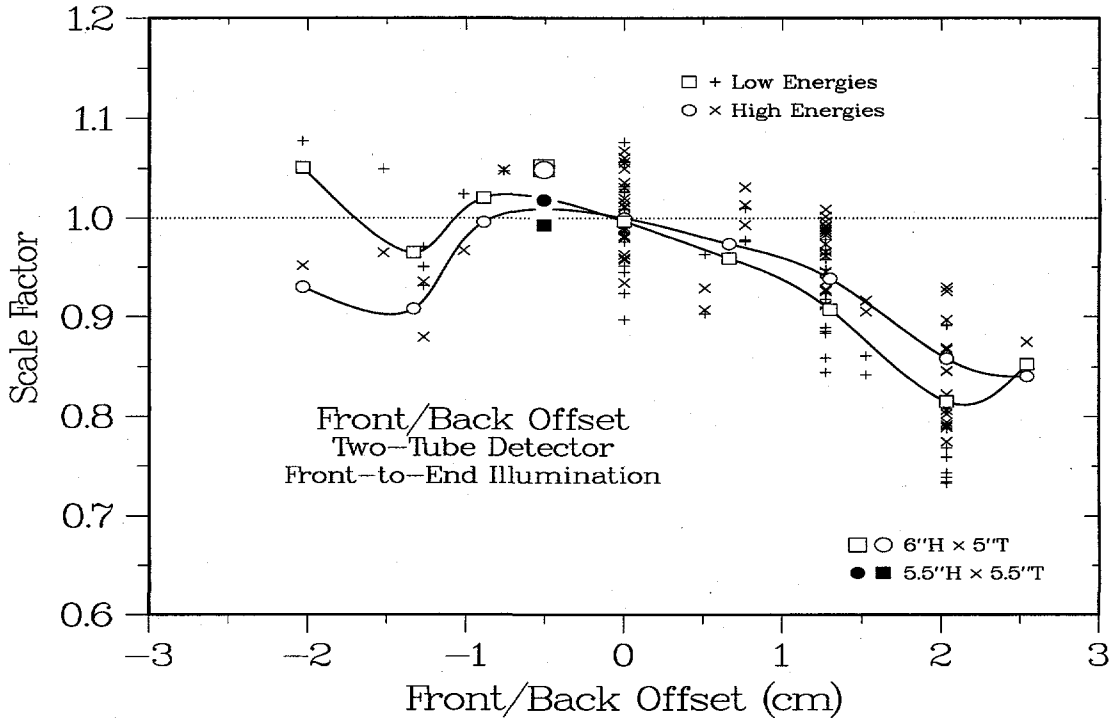

Figure 5.19. As in Figure 5.6, effect of changing the front/back offset of the two tubes in a polyethylene-moderated neutron detector illuminated from the front and end.

Slope Dependence. The model used to represent the front-to-end slope data is the same as that for the front-to-top analyses, except the physical areas involved require using the difference between the detector's length×height (front illumination) and its thickness×height (end illumination), that is, the scaling parameters are expressed in terms of $D_L = (L-T)/(L^2+T^2)^{1/2}$ and $X_L = X/(L^2+T^2)^{1/2}$. As indicated in **Figure 5.20**, **Figure 5.21**, and **Figure 5.22**, the model is also successful at describing the angular dependence about the alternate axis using only the difference between the detector's length and thickness.

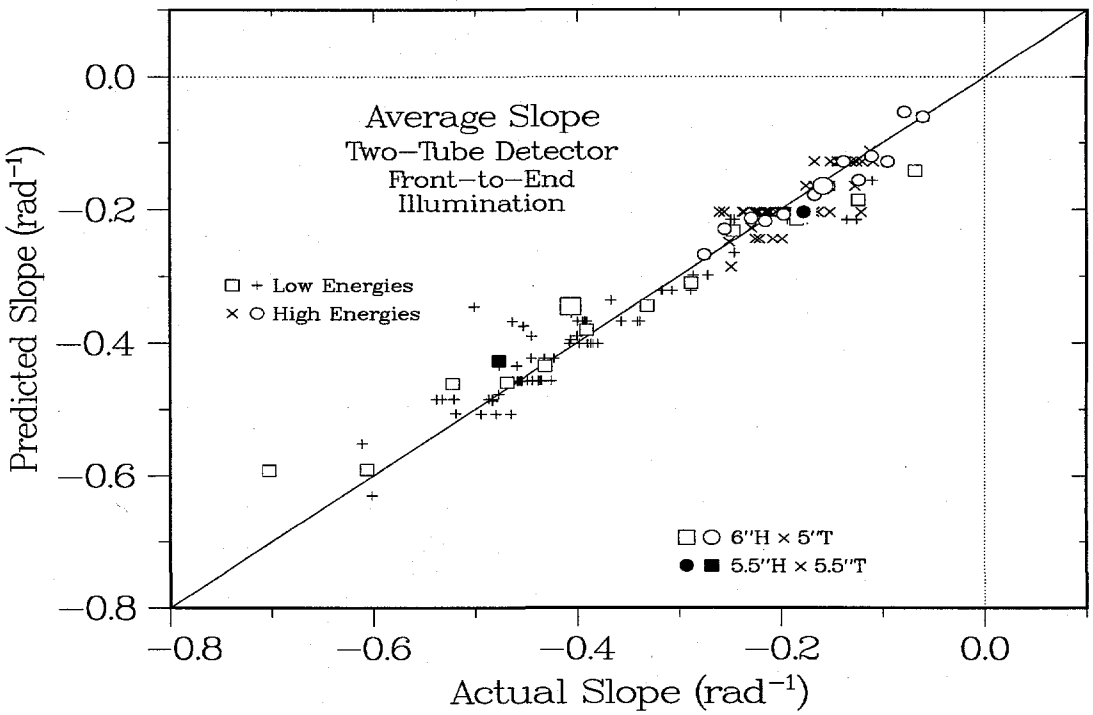

Figure 5.20. Accuracy of slope predictions as in Figure 5.11, but for rotation of the incident neutron direction from the front to the end of the detector.

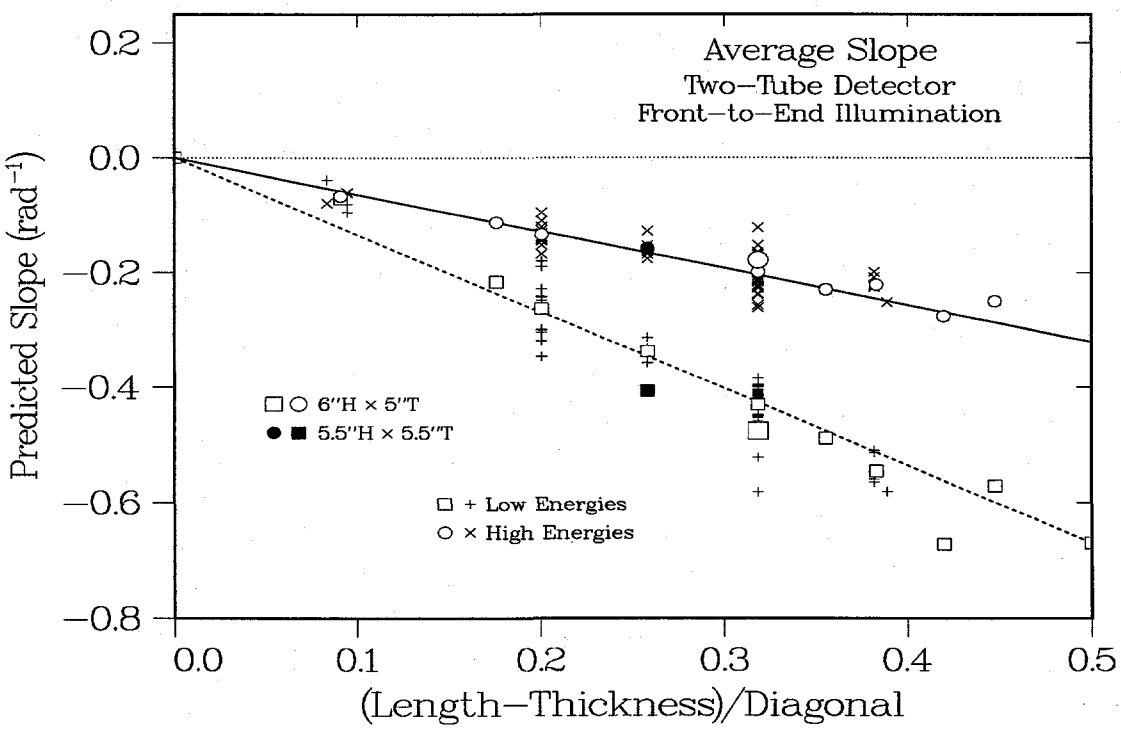

Figure 5.21. Slope dependence of the difference between the detector's length and thickness for front-to-end illumination (see Figure 5.12).

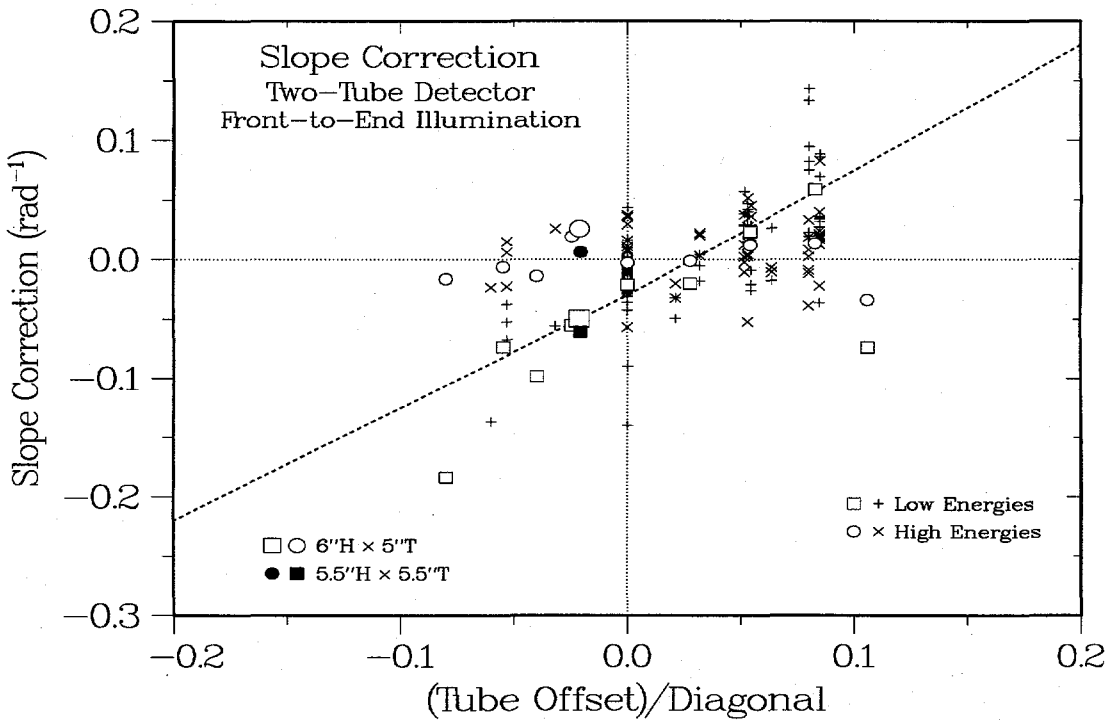

Figure 5.22. Lack of significant dependence of the slope on the front/back position of the two tubes (see Figure 5.13).

Summary of Front-to-End Analyses. The front-to-end results for the two-tube case are similar to those for the corresponding front-to-top analyses, although the smaller number of individual runs causes more scatter in the data set. Again, the effective areas for all detector variations can be adequately described by a minimum number of parameters: the polyethylene mass, the gas quantity, and perhaps the front/back offset.

5.3. Analyzing Powers

Magnitudes. The ability to determine the average direction of the incident neutron fluence is summarized in Sec. 2.3 and discussed in detail in Ref. 5. Additional examples of the approach and mathematical formalism are described in Ref. 10. Basically, the difference between the count rates in the different segments of a multielement detector depends at least partly on the incident beam direction. In our case, the count rates are equal by symmetry for illumination from the detector's front or end, but illumination from the detector's top can be expected to give a higher rate in the upper tubes. Accordingly, rotating the beam from the front to the top gives a count-rate ratio that increases with angle, usually with a cosine dependence. Rotation from the front to the end provides no such effect and provides no angular information. Further, the magnitude of the count-rate difference depends on energy; it reaches a maximum at low energies and should almost disappear at high energies. The largest value of the difference at a particular energy gives the detector's analyzing power, which has a maximum value of 1.0. For the reference design this energy-dependent quantity is illustrated in **Figure 5.23**, which shows that the count-rate ratio indeed approaches zero for energies above 10 MeV. In fact, the present values are essentially the same as those for the existing detector, which are given in Table 2.1.

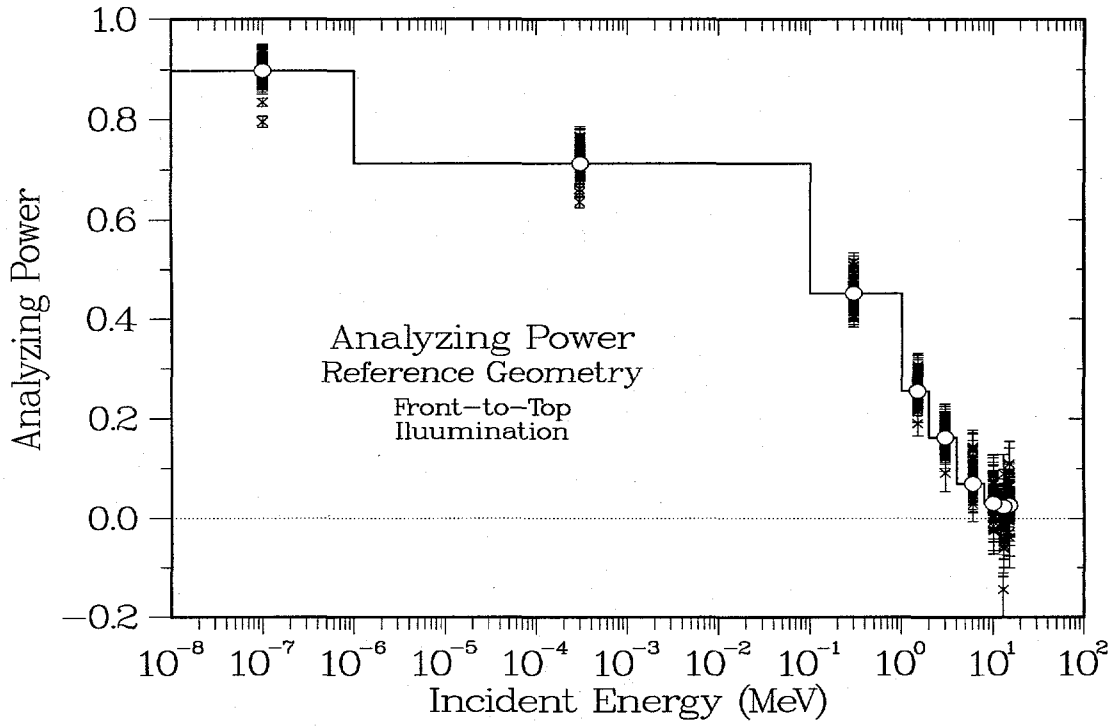

Figure 5.23. Energy-dependent analyzing power for the reference design for neutrons incident on the top of the detector.

Geometry Effects. The values plotted in Figure 5.23 are for the reference design; the values for other geometries can be converted to give equivalent results. This conversion allows us to determine how different features of the design affect the maximum size of the count-rate differences. This variation is largely determined by only two parameters, the separation between the two ^{3}He tubes (**Figure 5.24**) and the height of the detector (**Figure 5.25**). The dependence on separation distance is to be expected; as the distance increases, the difference between the fluences at the two tubes also increases, as does the ratio between the count rates. The reason for the height dependence is similar, but more subtle. Once the separation dependence is accounted for, as the height increases, the average neutron energy at the tube locations decreases; the attenuation between the tubes therefore increases, which then increases the count-rate ratio. The results of this two-parameter model for the energy bin from 1 to 2 MeV are given in **Figure 5.26**, which shows that the analyzing power near 1.5 MeV varies from a low of 0.05 to a high of 0.40, with typical values clustered around the reference value near 0.25.

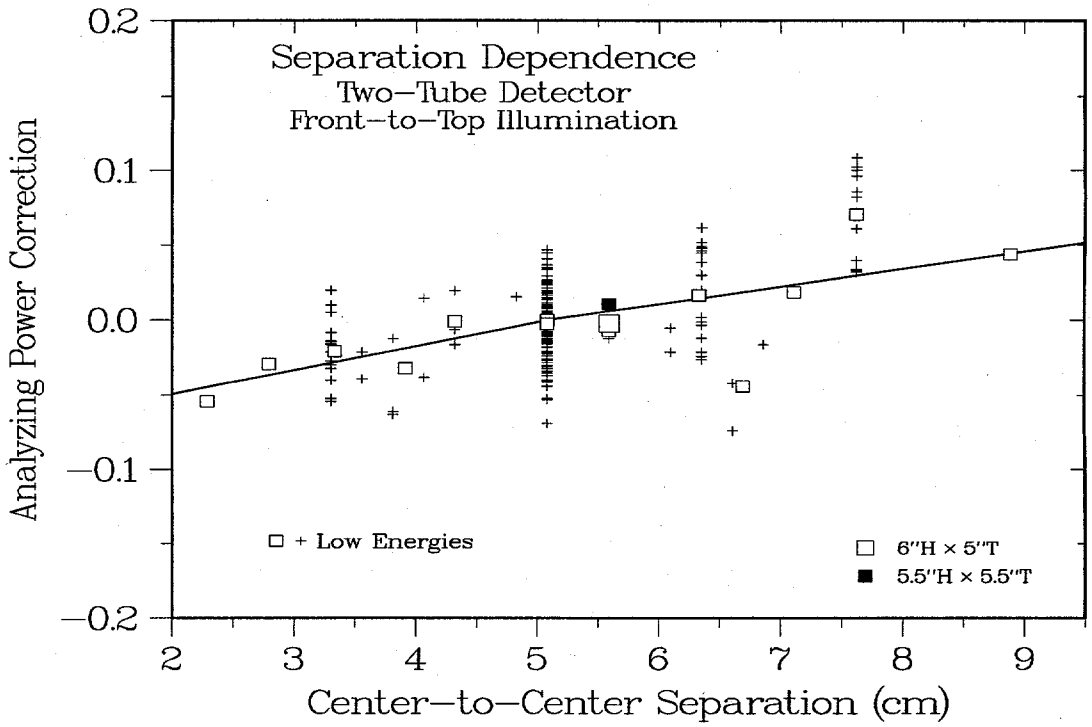

Figure 5.24. Dependence of the 1.5-MeV analyzing power on tube separation.

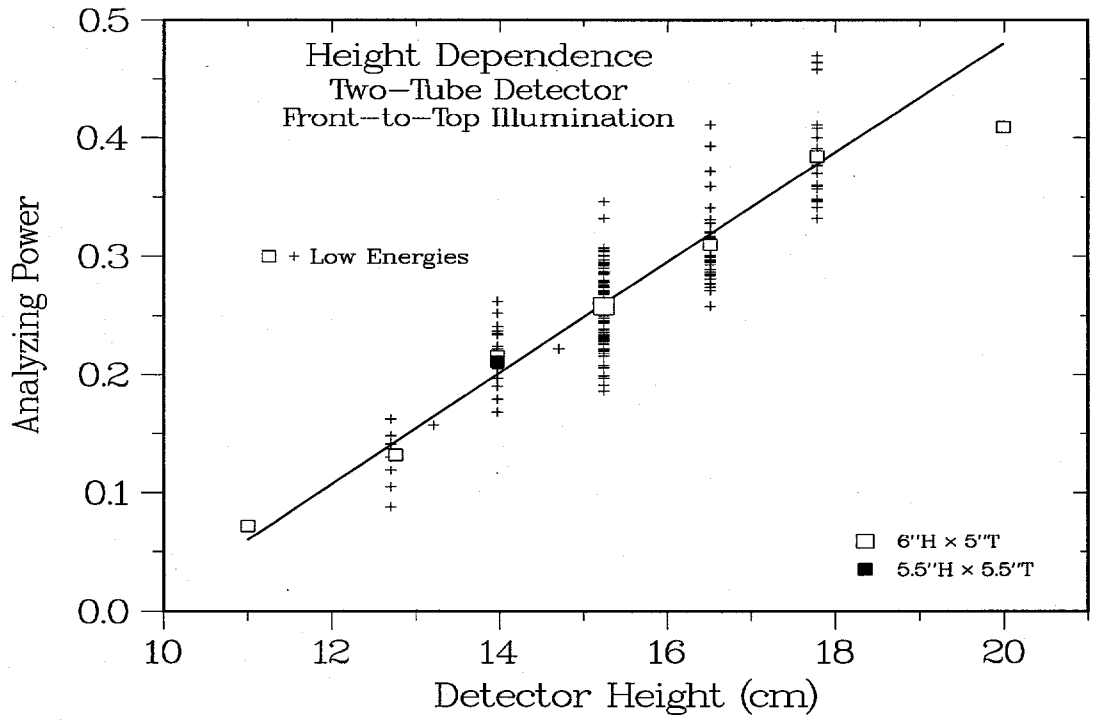

Figure 5.25. Dependence of the 1.5-MeV analyzing power on detector height.

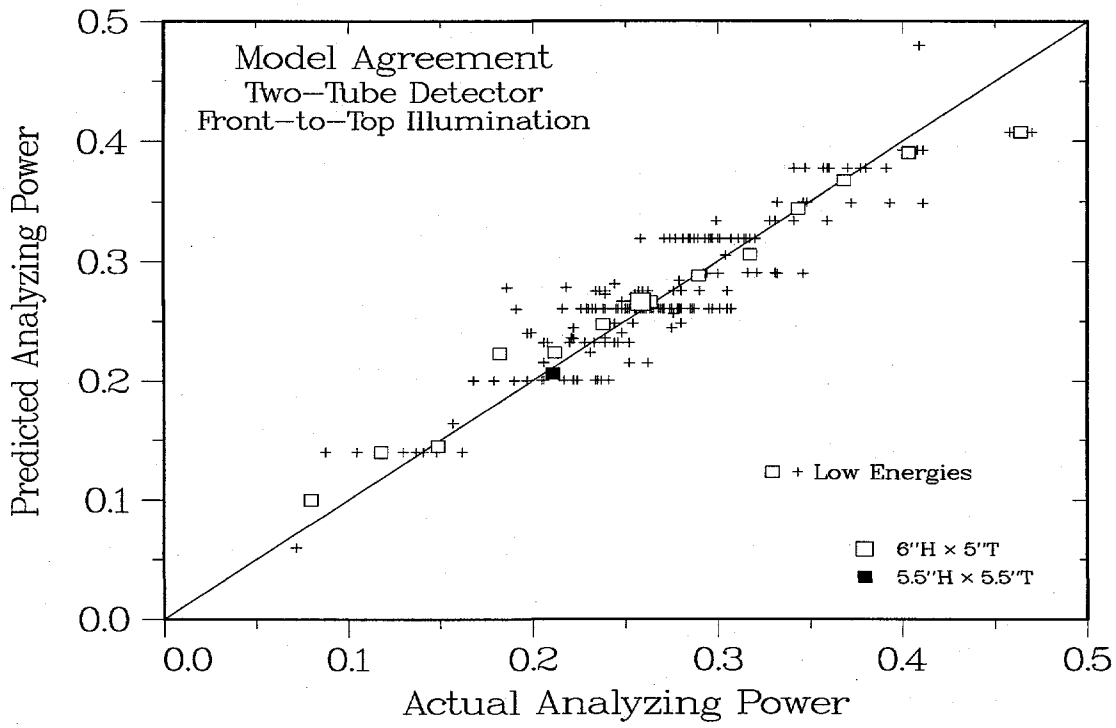

Figure 5.26. Agreement between the actual 1-MeV analyzing power and that predicted by a two-parameter model.

5.4. Two-Tube Discussion

Results. As shown by the agreement between the actual and predicted results for the effective areas (Figure 5.1 and Figure 5.14), the slopes (Figure 5.11 and Figure 5.20), and the analyzing power (Figure 5.26), our simple model is very successful at describing the magnitude, angular distribution, and ratio between the count rates for the two tubes at all incident energies and directions. The major parameters in the model are the detector's plastic mass, aspect ratio, and gas quantity; minor parameters are the front/back tube offset and the tube separation. Because these parameters can each be varied independently, it is easy to evaluate the effect of each one separately and to determine an optimum value, which is an issue of central importance to the problem of detector design. Our results therefore satisfy the goals embodied in the three analysis steps listed in Chap. 4.

6. ONE-TUBE DETECTOR

6.1. Front-to-Top Illumination

Effective Areas and Moderator Masses. The analysis approach described in detail for the two-tube detector in Chap. 5 can also be applied to the corresponding one-tube detector design. The results for the actual and predicted effective areas are shown in **Figure 6.1**, and the agreement is again excellent. The explicit dependence of effective area on plastic mass is shown in **Figure 6.2**. It is immediately clear that a given amount of polyethylene provides much less effective area than it does for the corresponding two-tube results in Figure 5.2. It is also apparent that increasing the amount of polyethylene would be of little use in this case, because even the high-energy data are beginning to saturate at the largest mass values.

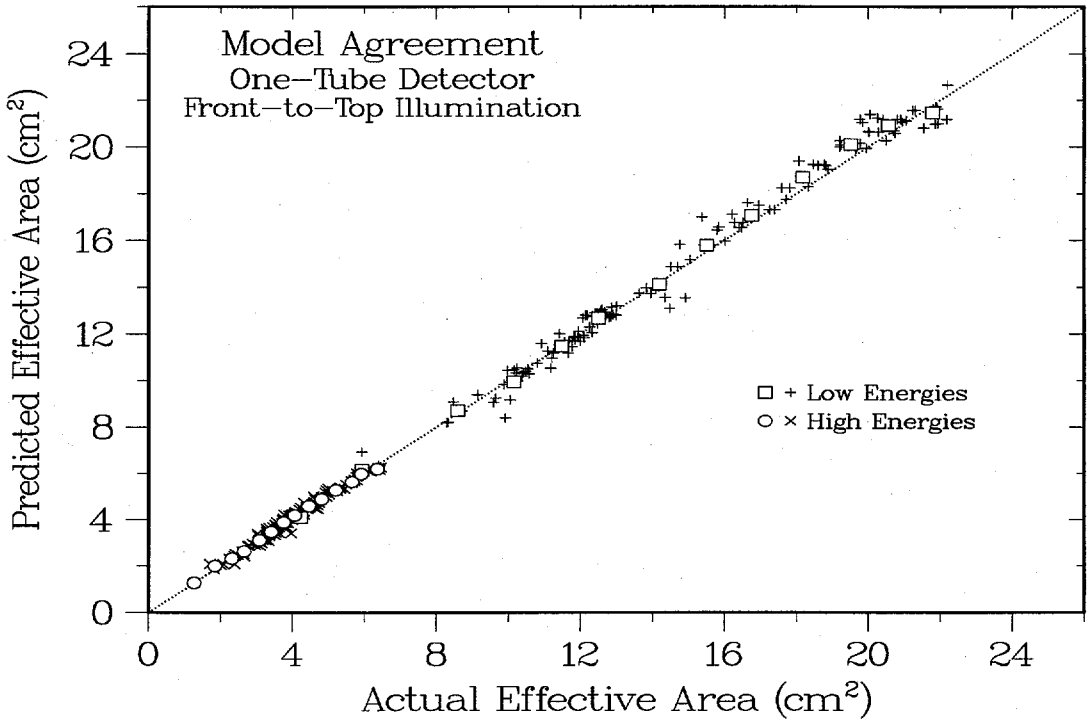

Figure 6.1. Agreement between the actual and predicted effective areas for a neutron detector with a single polyethylene-moderated ^{3}He tube (see Figure 5.1).

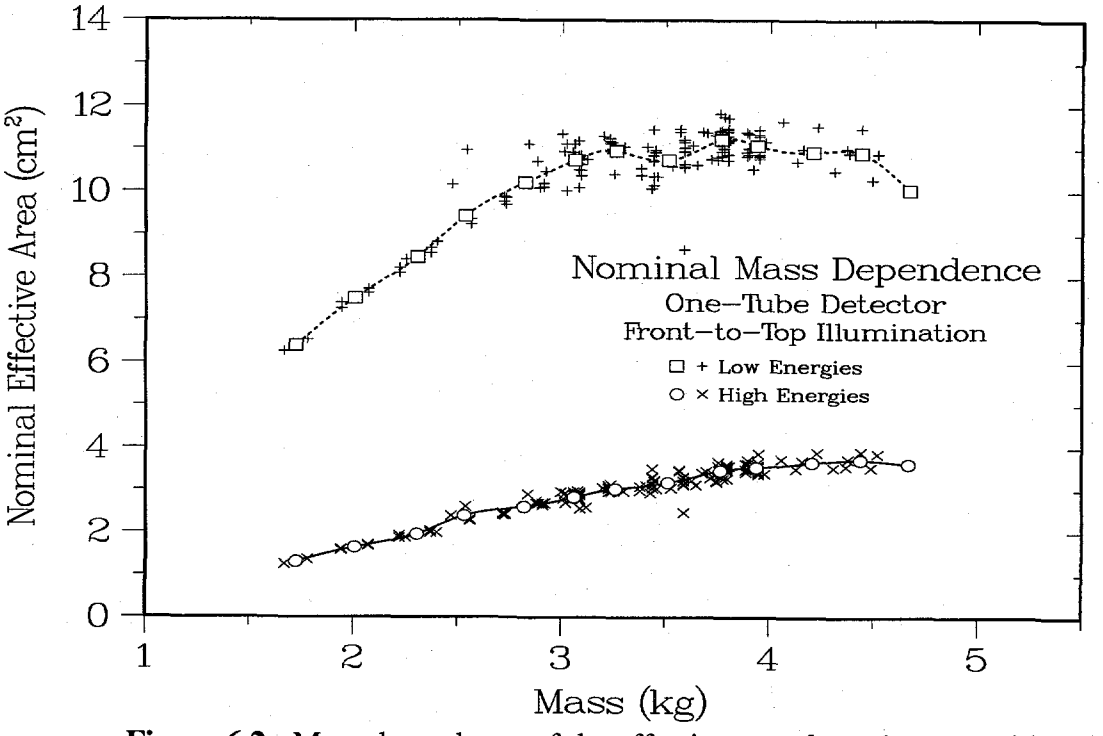

Figure 6.2. Mass dependence of the effective area for a detector with a single ^{3}He tube illuminated from the front and top (see Figure 5.2).

Tube Pressure, Radius, and Location. As seen in **Figure 6.3**, **Figure 6.4**, and **Figure 6.5**, the comparison between the one-tube and two-tube gas parameters follows the pattern seen in the mass dependence: the behaviors are qualitatively similar, but there is greater evidence of saturation in the one-tube data as the pressure or radius is increased. In particular, note that the dependence of radius on energy is the same as before, but the dependence on the gas quantity Q appears to less reproducible than previously. In contrast, **Figure 6.6** shows a clear energy dependence in the optimum values for the front/back offset of the single counter tube.

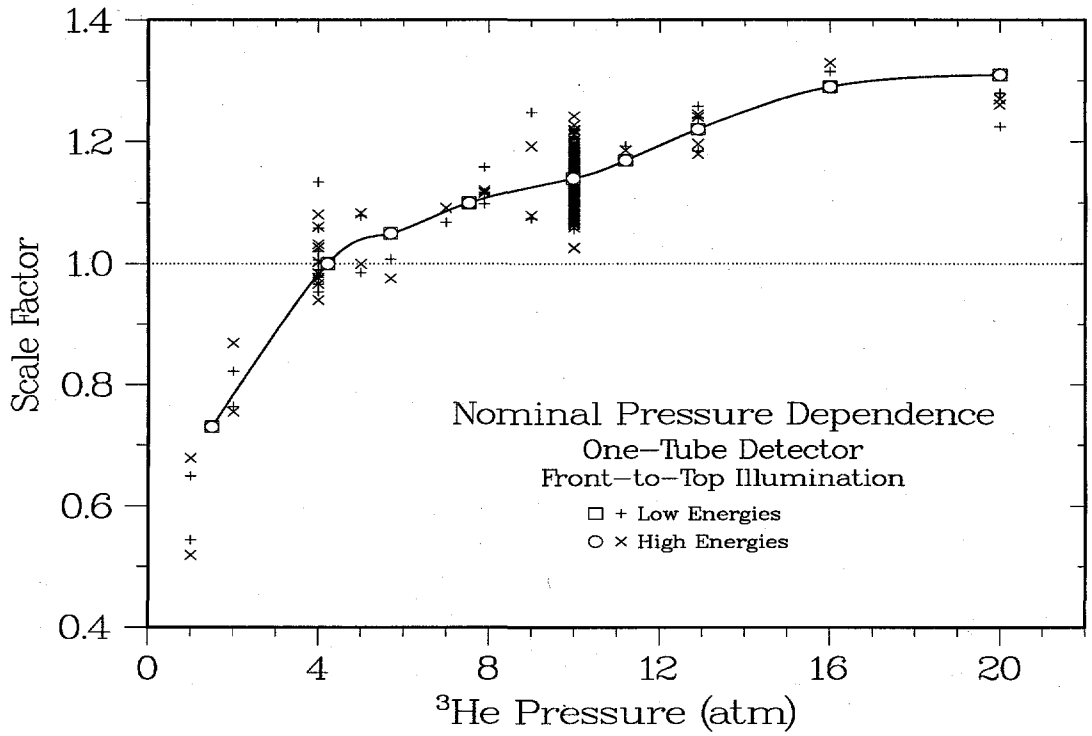

Figure 6.3. Effect of varying the gas pressure on the effective area of a detector with a single ^{3}He tube illuminated from the front and top (see Figure 5.3).

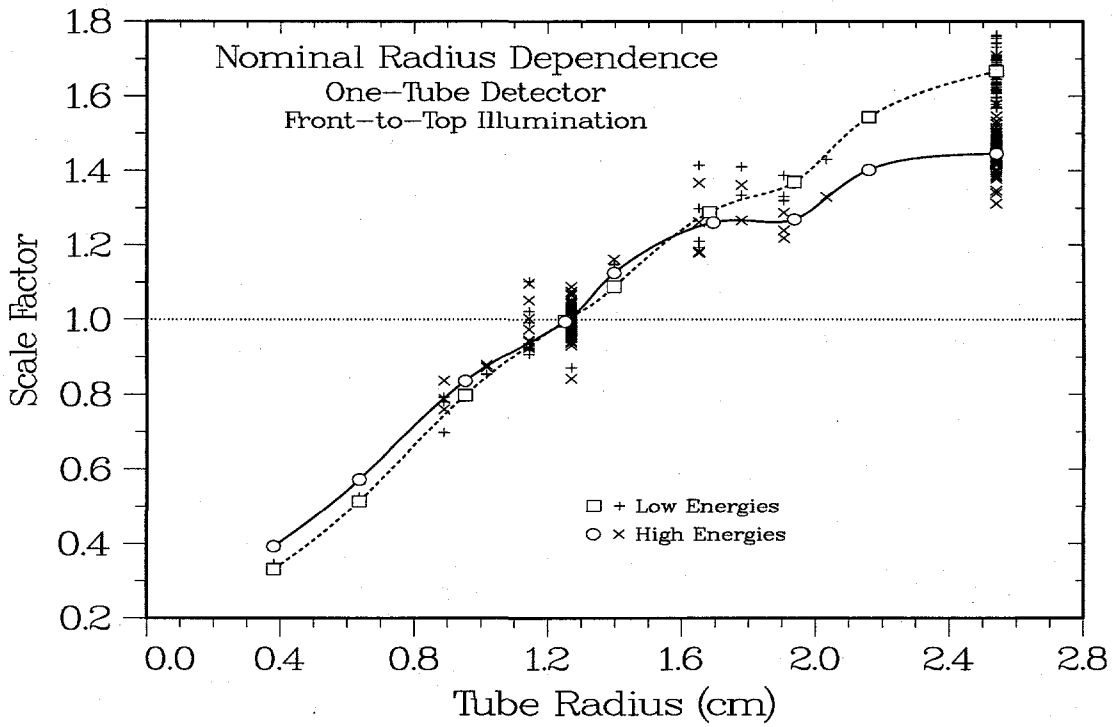

Figure 6.4. Effect varying the radius of the single ^{3}He tube in a polyethylene-moderated neutron detector illuminated from the front and top (see Figure 5.4).

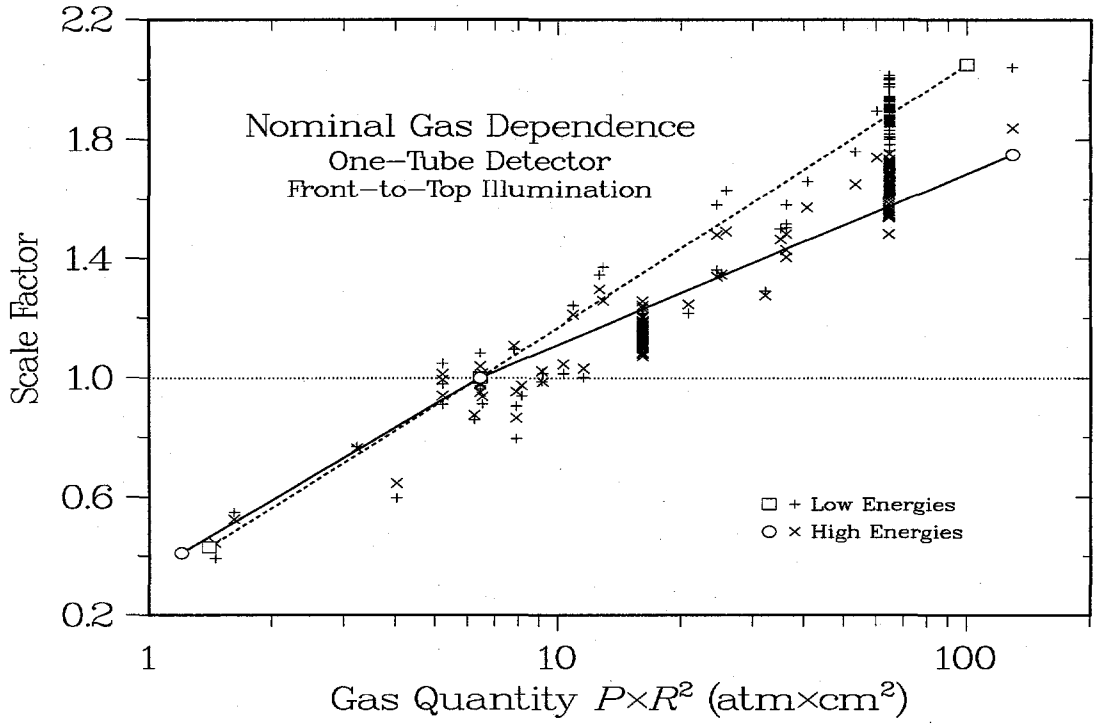

Figure 6.5. Result of combining gas pressure and tube radius into a single quantity (see Figure 5.5).

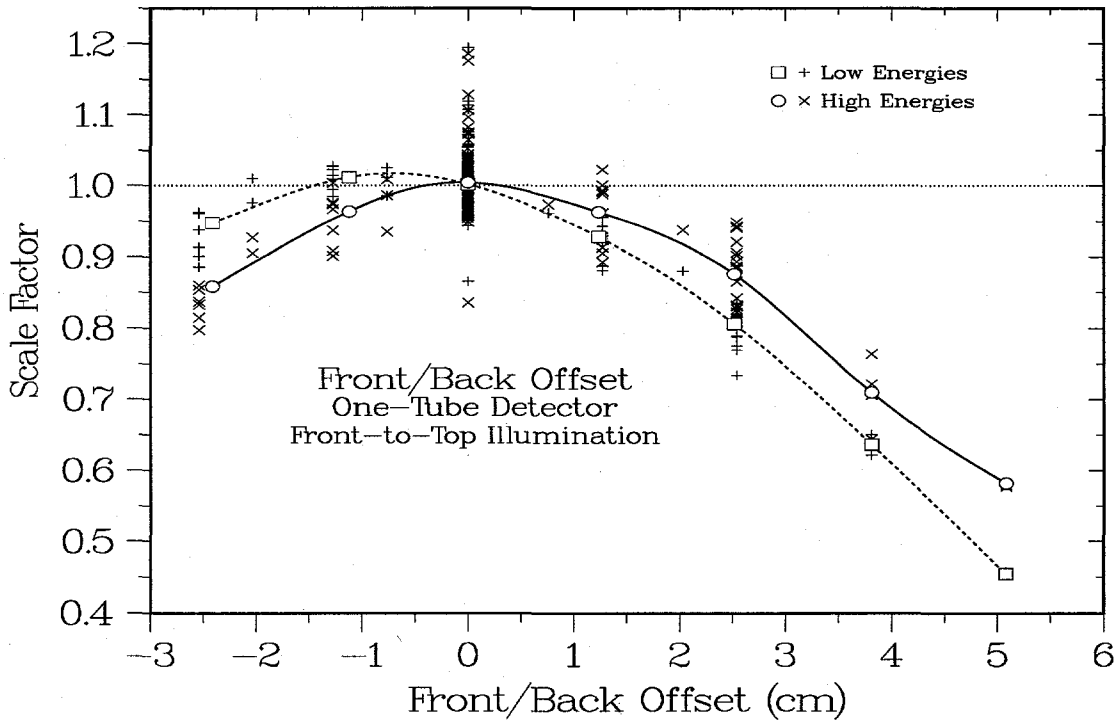

Figure 6.6. Effect of changing the front/back offset of the single ^{3}He tube in a polyethylene-moderated neutron detector illuminated from the front and top (see Figure 5.6).

Slope Dependence. The slope dependence of the one-tube model uses the same formalism as the two-tube case, except of course there is no variation in separation distance. As seen in **Figure 6.7**, the agreement between the actual and predicted slopes is again good, and **Figure 6.8** and **Figure 6.9** show that the dependence on detector geometry agrees with that seen in the two-tube data.

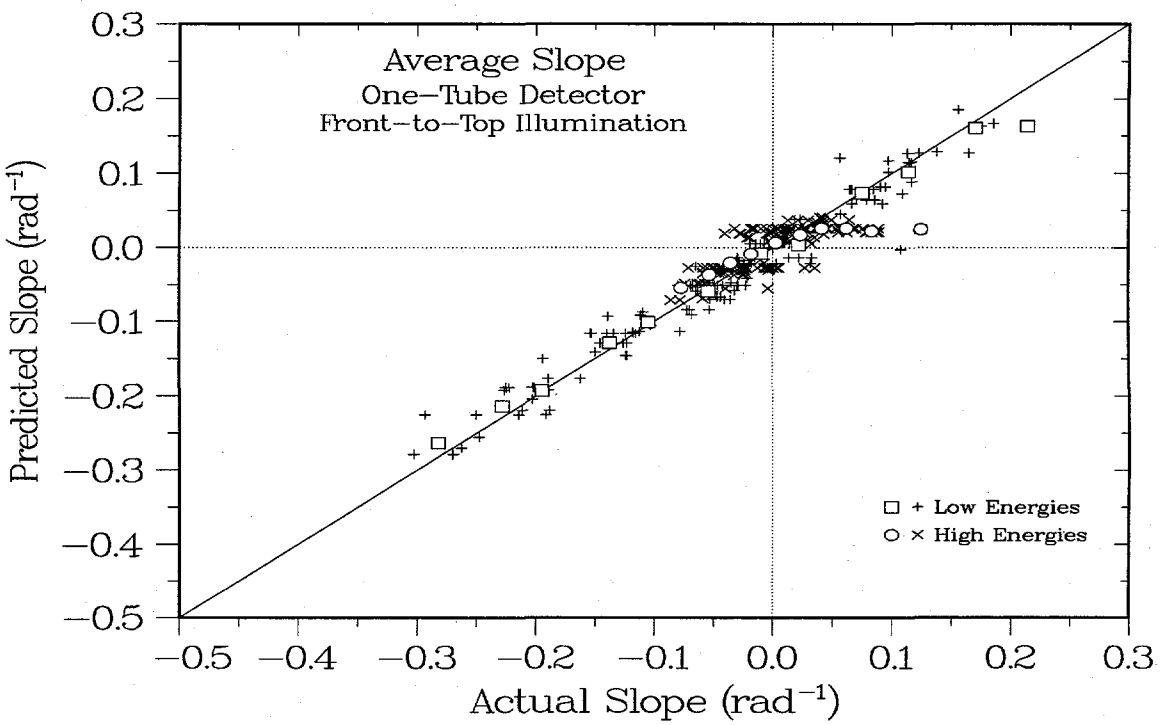

Figure 6.7. Agreement between the actual slopes of the calculated MCNP angular distributions and the values predicted by the analytical model (see Figure 5.11).

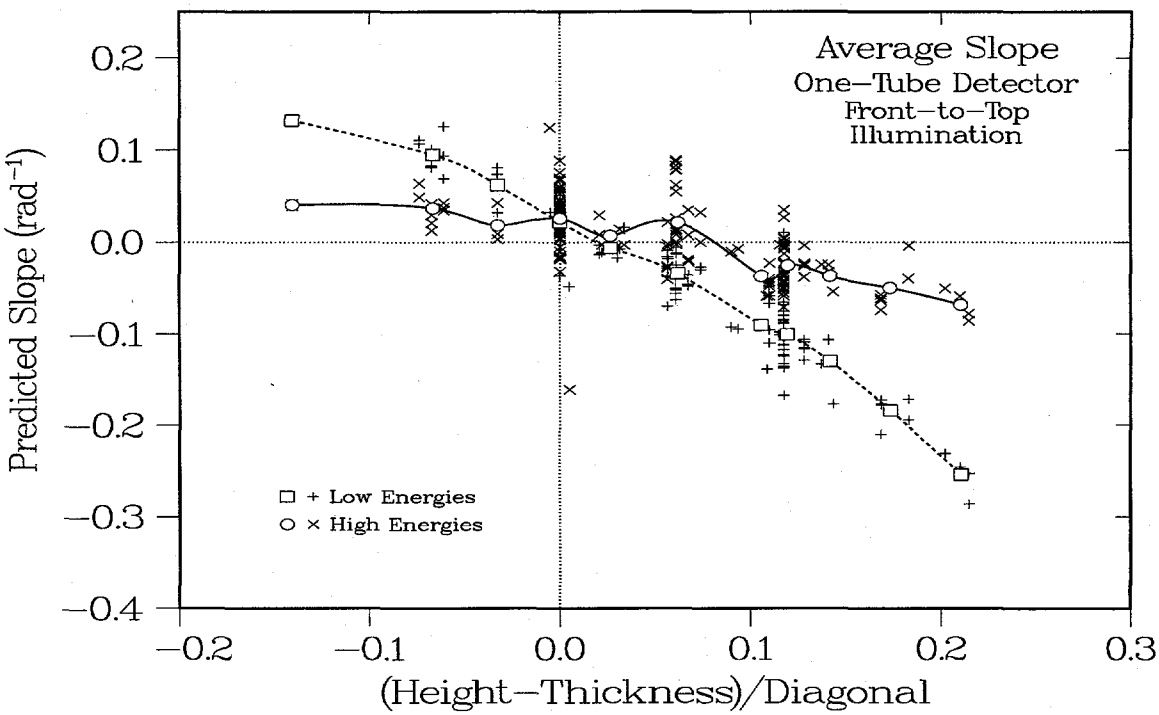

Figure 6.8. Effect of changes in the difference between the moderator height and thickness on the slopes of angle distributions for a one-tube detector (see Figure 5.12).

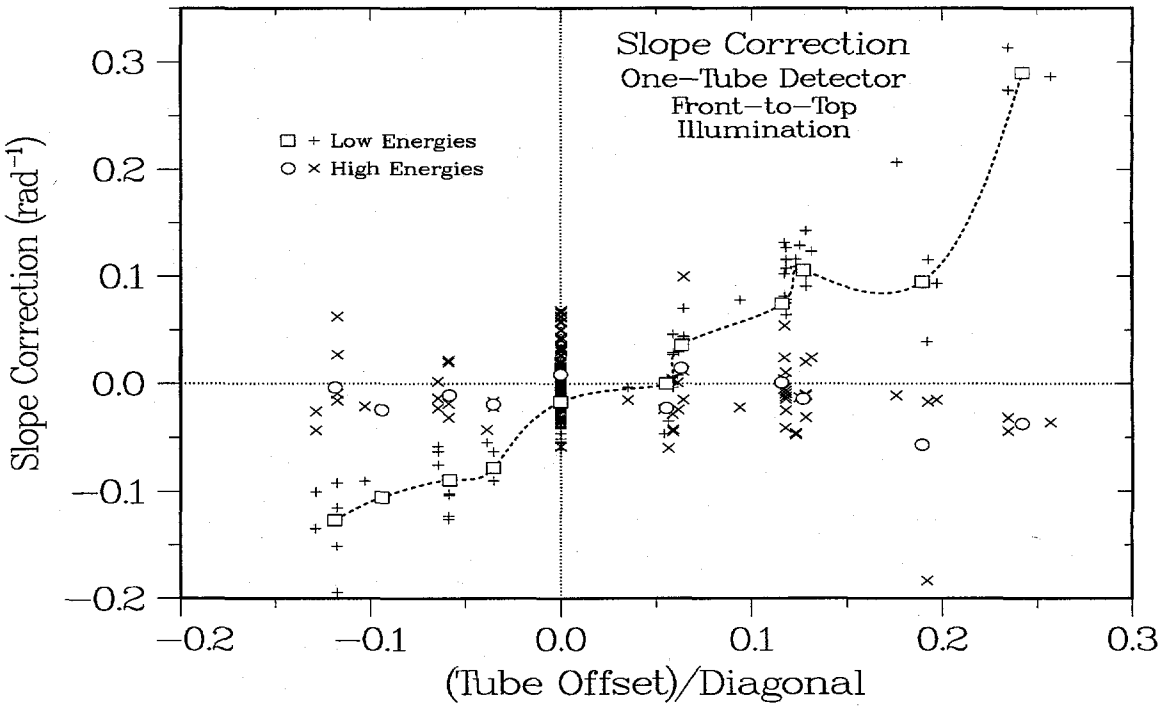

Figure 6.9. Effect of changes in the front/back offset in the tube position on the slope of the angular distribution for front-to-top illumination of a one-tube detector (see Figure 5.13).

6.2. Front-to-End Illumination

Effective Areas and Mass Dependence. The one-tube detector's front-to-end modeling completes our set of four detector geometries, and the results are again excellent. The agreement between actual and predicted areas is shown in **Figure 6.10**, and the dependence on plastic mass is shown in **Figure 6.11**. As before, the front-to-end orientation shows less evidence of mass saturation than the corresponding front-to-top results.

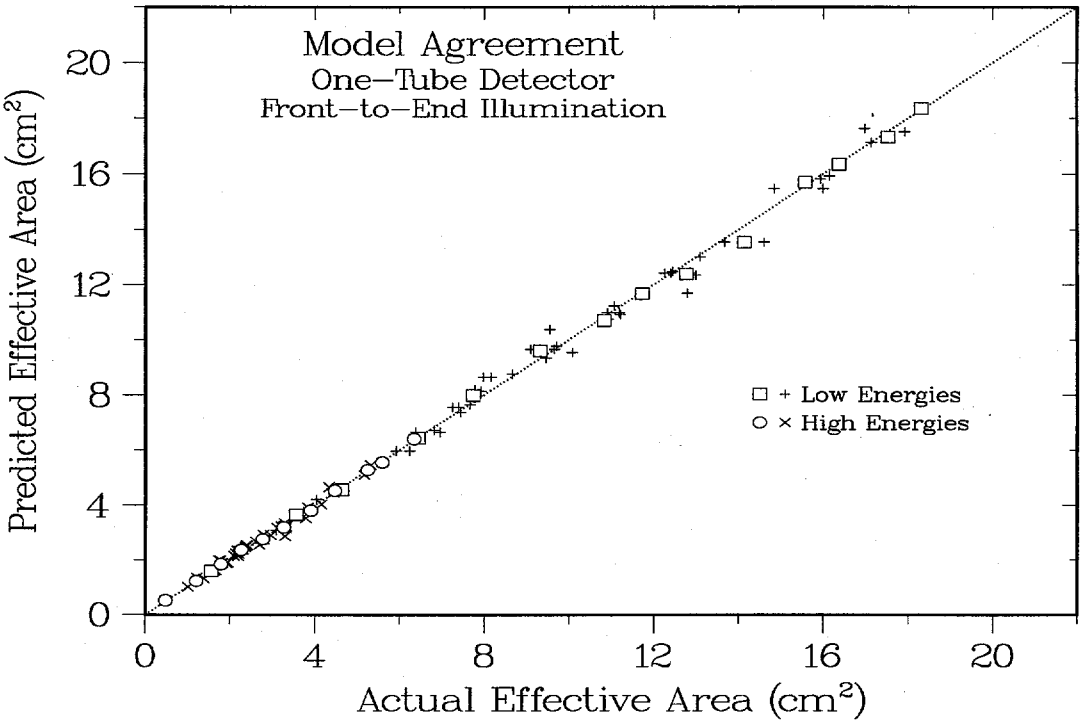

Figure 6.10. Agreement between MCNP calculations and analytical predictions for front-to-end illumination of a one-tube detector (see Figure 6.1).

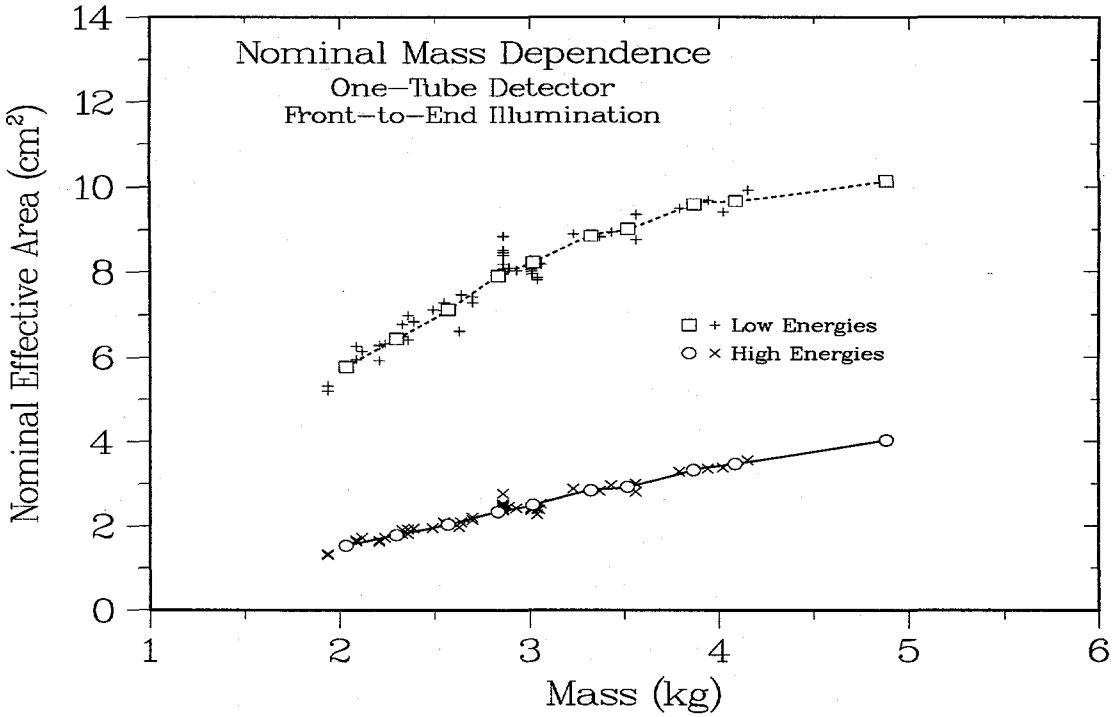

Figure 6.11. Mass dependence of a one-tube detector illuminated front the front and top (see Figure 6.2).

Tube Pressure, Radius, and Position. Within the limitations of the sparser data sets, the dependences on pressure (**Figure 6.12**), radius (**Figure 6.13**), and gas quantity (**Figure 6.14**) are essentially as expected, and the dependence of front/back offset (**Figure 6.15**) shows the customary shift between the optimum locations and low and high energies.

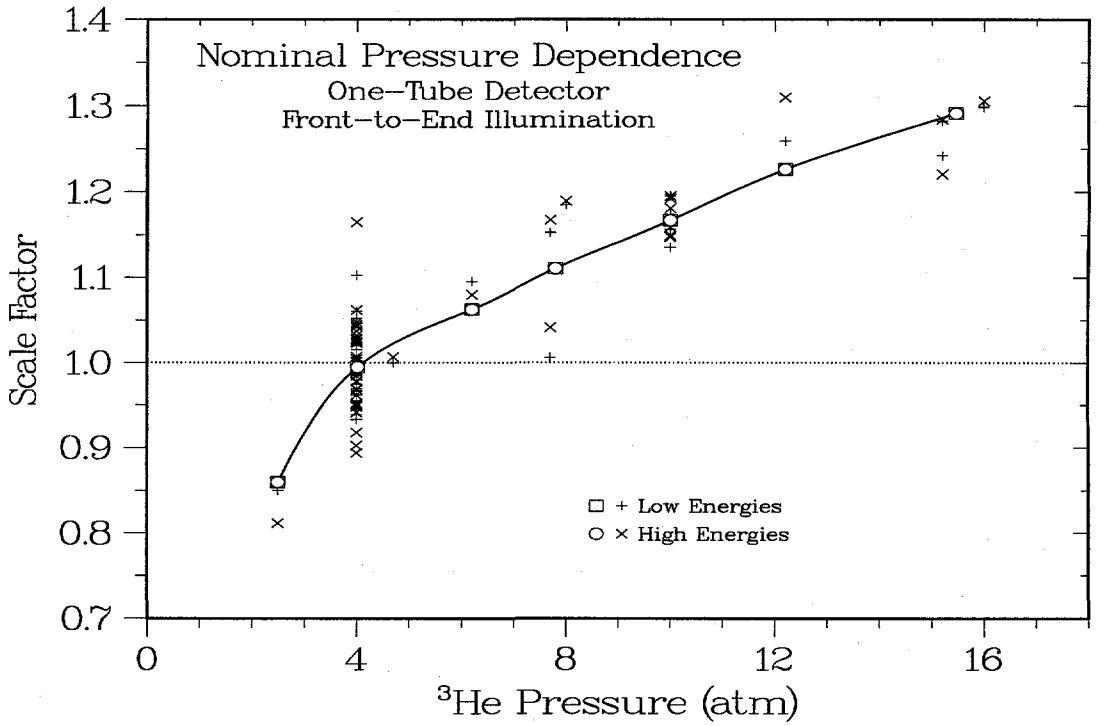

Figure 6.12. Pressure dependence of the effective area of a single-tube detector with front-to-end illumination (see Figure 6.3).

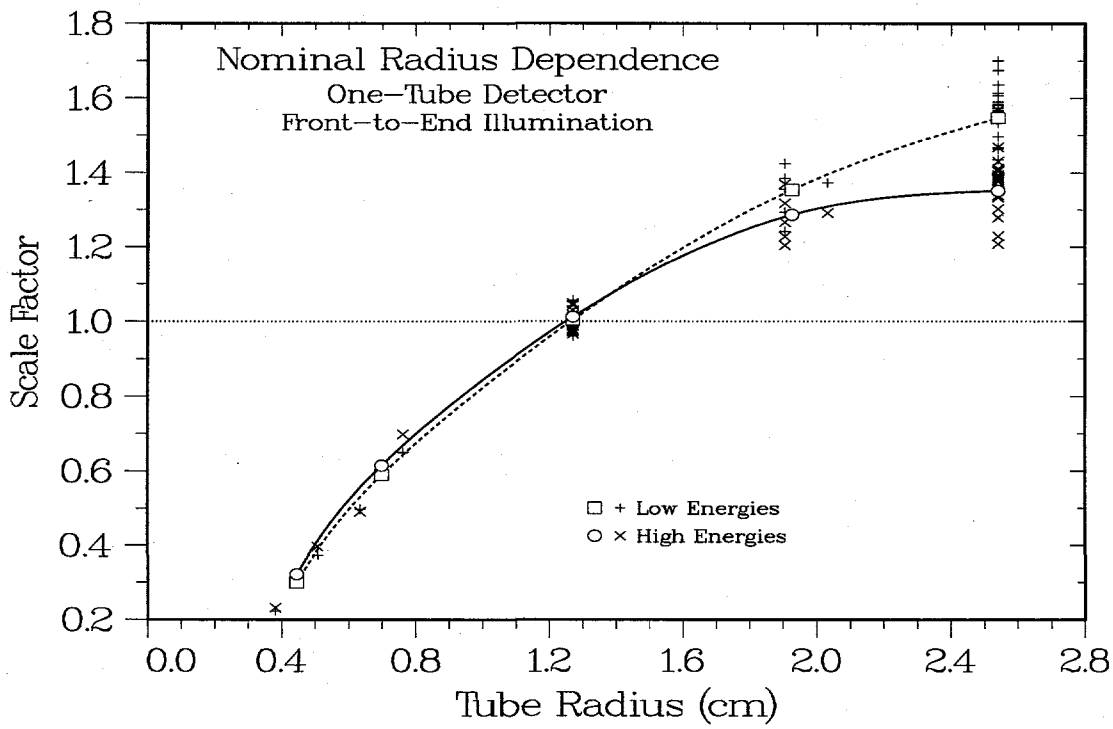

Figure 6.13. Effect of changing the radius of the ^{3}He tube for front-to-end illumination of a one-tube detector (see Figure 6.4).

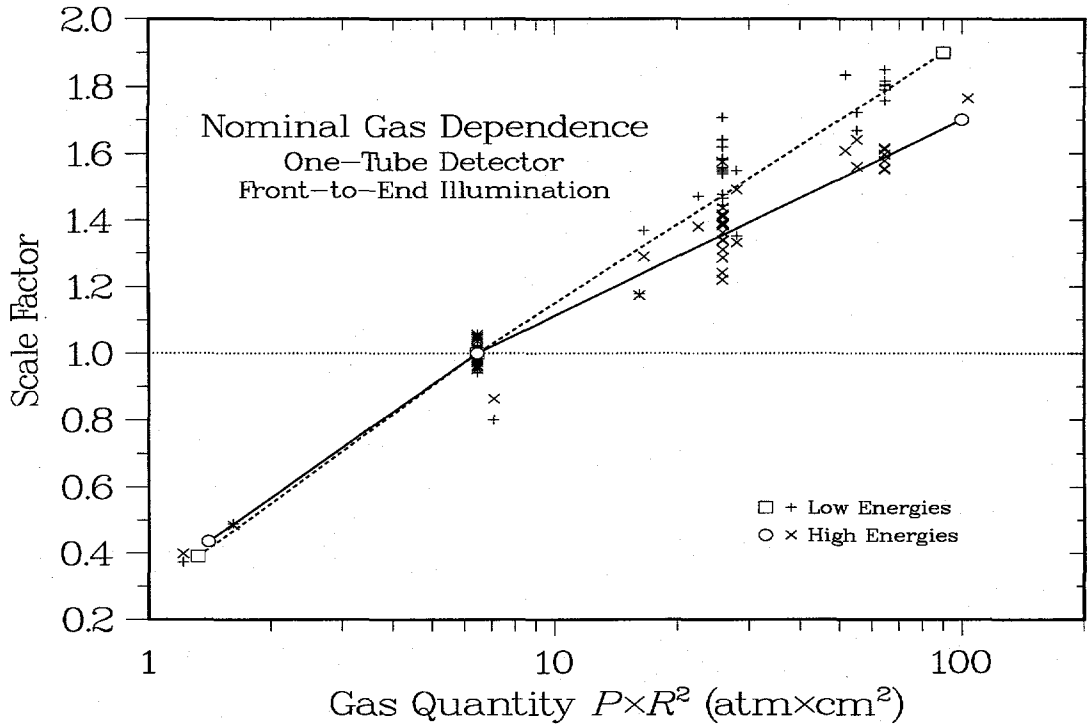

Figure 6.14. Result of combining gas pressure and tube radius into a single parameter (see Figure 6.5.)

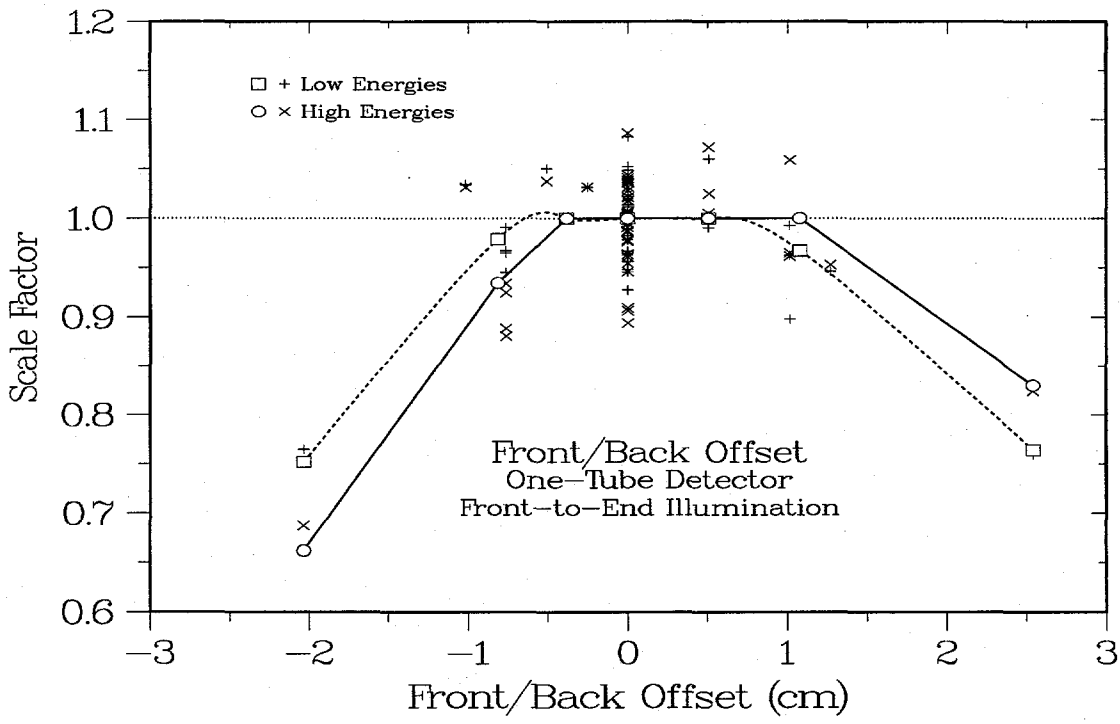

Figure 6.15. Effect of changing the front/back position of the single tube in a one-tube detector (see Figure 6.6).

Slope Dependences. The angular dependence of the one-tube front-to-end *results* is again well described by the same analytical model, as shown by the comparison in **Figure**

6.16, the detector geometry dependence in **Figure 6.17**, and the lack of a clear offset dependence in **Figure 6.18**.

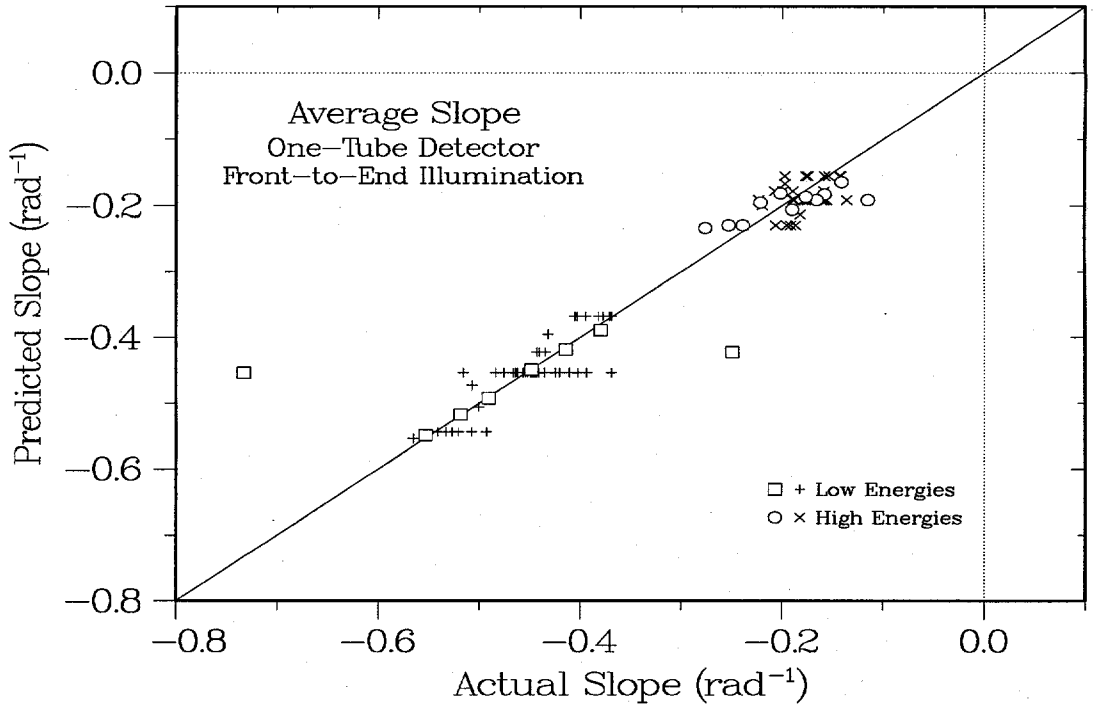

Figure 6.16. Success of the model in describing the slope results for front-to-end illumination of a one-tube detector.

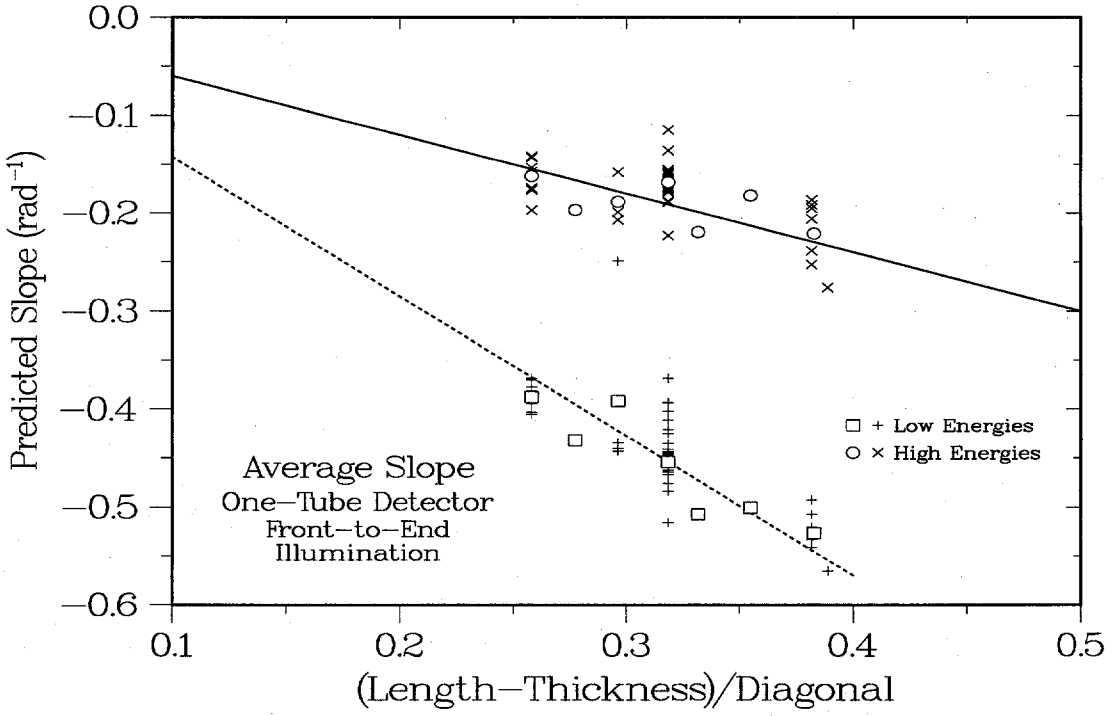

Figure 6.17. Dependence of the average slope on the difference between the detector length and thickness.

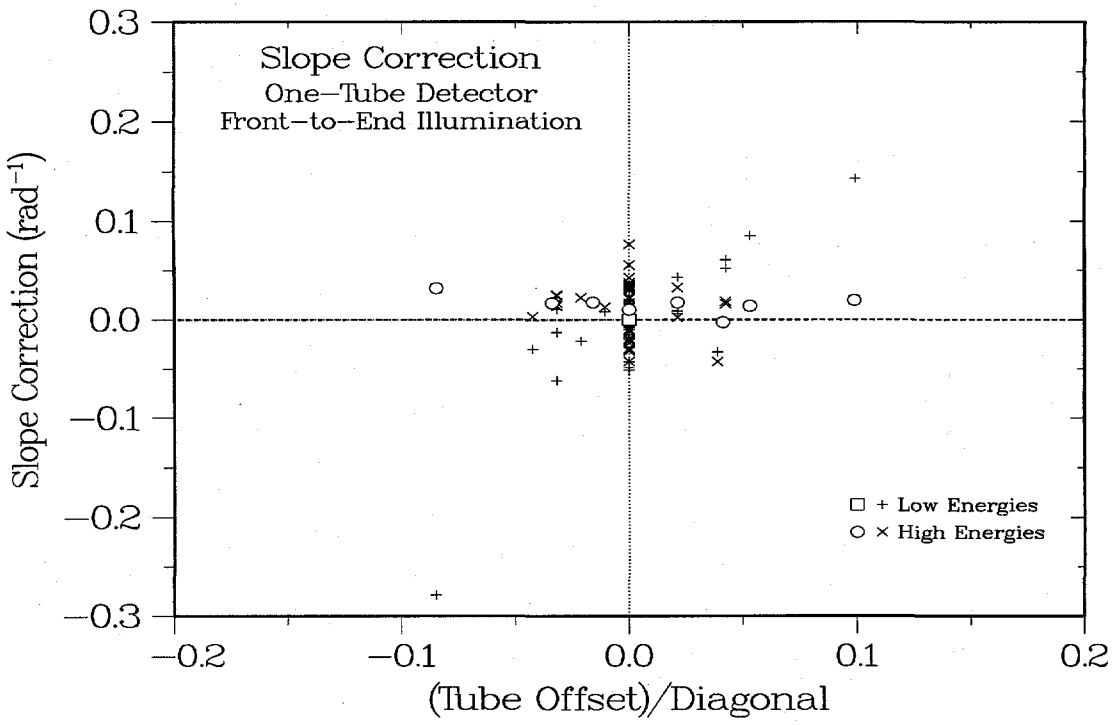

Figure 6.18. Lack of dependence of the slope on the tube offset in a one-tube detector.

6.3. One-Tube Discussion

Results. In most cases the one-tube analyses provide results that are qualitatively similar to those for the two-tube analyses in the previous chapter. A significant difference, however, is the behavior of the mass dependence, which does not appear to reach an asymptotic limit at high energies. This result suggests that the relative amounts of polyethylene and ^{3}He gas are not as optimized as in the two-tube case. We will return to this issue in the next chapter, which attempts to develop a single analytical model that covers both the one- and two-tube detector designs.

7. GENERIC DETECTOR

Overview. There exists a definite similarity between the behaviors of the parameters for the two-tube and one-tube detectors described in the previous two chapters. With the exception of the mass dependence, it appears that a single set of parameterizations could be developed that would be able to reproduce the results for both cases. We therefore begin our analyses by developing a method for at least approximately combining the mass dependences, and then we combine the remaining parameters using these common mass values. Throughout this chapter the individual and average values for the individual runs are the same as those shown in the separate analyses in Chaps. 5 and 6; the only difference is the spline curves drawn through the points, which are smooth functions used to provide a new set of predictions for the effective area and slope of any given detector.

7.1. Approach

Mass Dependence. The effective areas for the four combinations of orientation and one- or two-tube geometries all have qualitatively similar behavior as functions of increasing mass (see Figure 5.2, Figure 5.15, Figure 6.2, and Figure 6.11). At low energies there is clear saturation at 3–4 MeV, but at high energies there is very little saturation at even the largest masses. It is therefore reasonable to keep the results for the two energy dependences separate but to combine the data for all other parameters with the appropriate normalization factors to compare with our reference 3-kg detector. The results in **Figure 7.1** indicate that the data for the front-to-top orientation are consistently 20% greater than those for the front-to-end case, and the two-tube data are 64% greater than the one-tube results. Note that these factors are multiplicative: the two-tube front-to-top data are $1.64 \times 1.20 = 1.97$ times the one-tube front-to-end results. Also, if the low-energy and high-energy data had been combined, the normalization factor between the low and high energies would have been 3.57 at 3 kg. In general, the agreement between the data and the smooth spline curve is good up to about 4 kg, where there begins to be clear evidence of differing saturation characteristics for the different geometries.

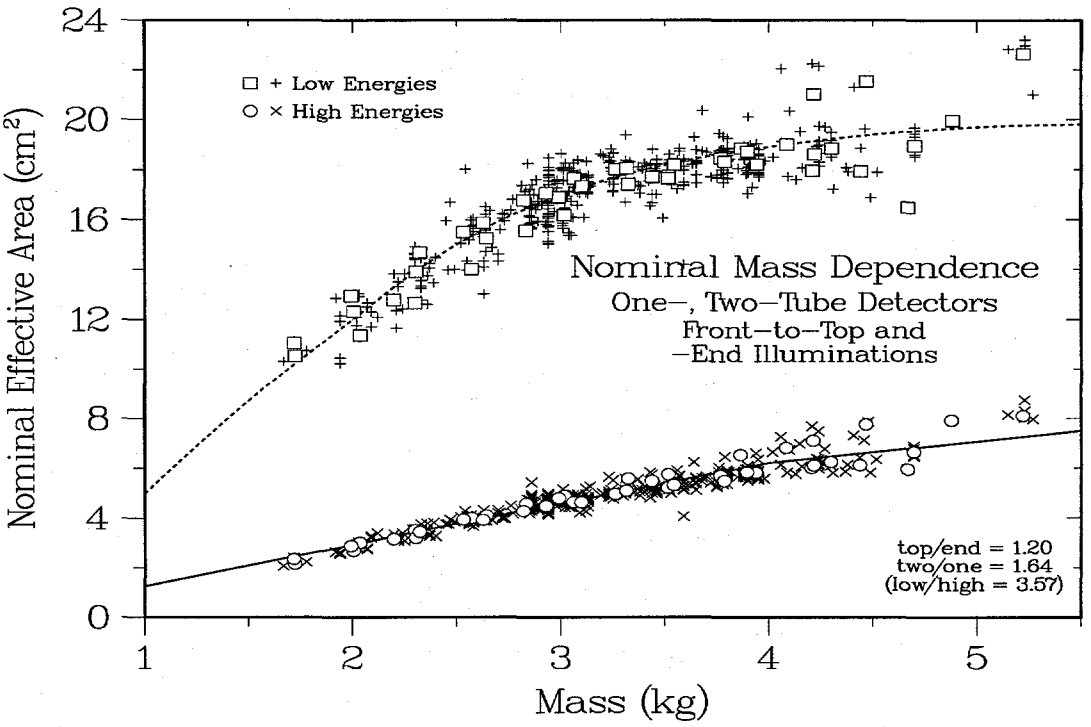

Figure 7.1. Generic mass dependence for front-to-top and front-to-end illumination of one- and two-tube detectors at low and high energies. The results for the front-to-end and one-detector analyses have been re-normalized to match the two-detector front-to-top results at a mass near 3 kg.

Gas Pressure and Tube Radius. The pressure dependences in Figure 5.3, Figure 5.16, Figure 6.3, and Figure 6.12 are already simplified because the low- and high-energy results are the same; **Figure 7.2** shows that variations in detector geometry also have little effect on the pressure dependence. It now appears that the reference 4-atm value represents a good choice, because there is a rapid increase in efficiency at lower pressures and a progressive decrease in the slope at higher values. Next, the radius dependences in Figure 5.4, Figure 5.17, Figure 6.4, and Figure 6.13 are combined in **Figure 7.3**. The previous individual cases all showed slightly different behavior at low and high energies; in the generic analysis the difference becomes apparent only at the highest radii, so it has been ignored for simplicity. A similar situation exists for the combined gas and pressure dependence in **Figure 7.4** (see Figure 5.5, Figure 5.18, Figure 6.5, and Figure 6.14). Although the R^2 scaling increases the scatter in the results at high gas quantities, when plotted logarithmically the average gas dependence has a particularly simple behavior: $q(Q) \propto \log(Q^{0.865})$.

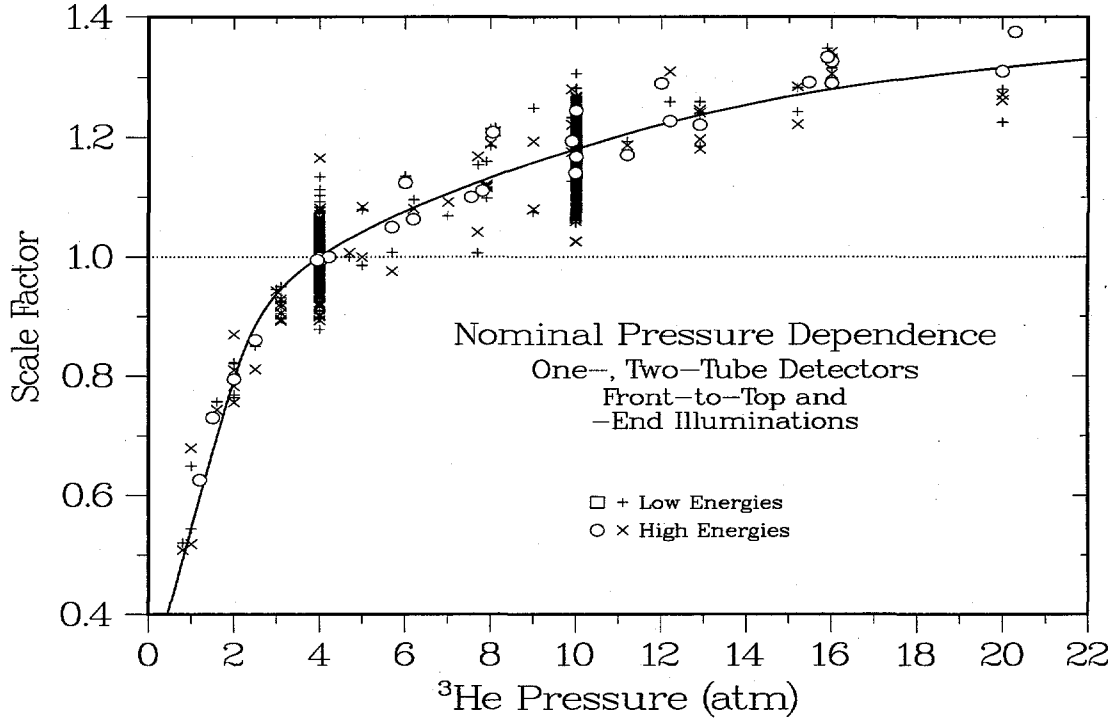

Figure 7.2. Combined average pressure dependence for all detector types.

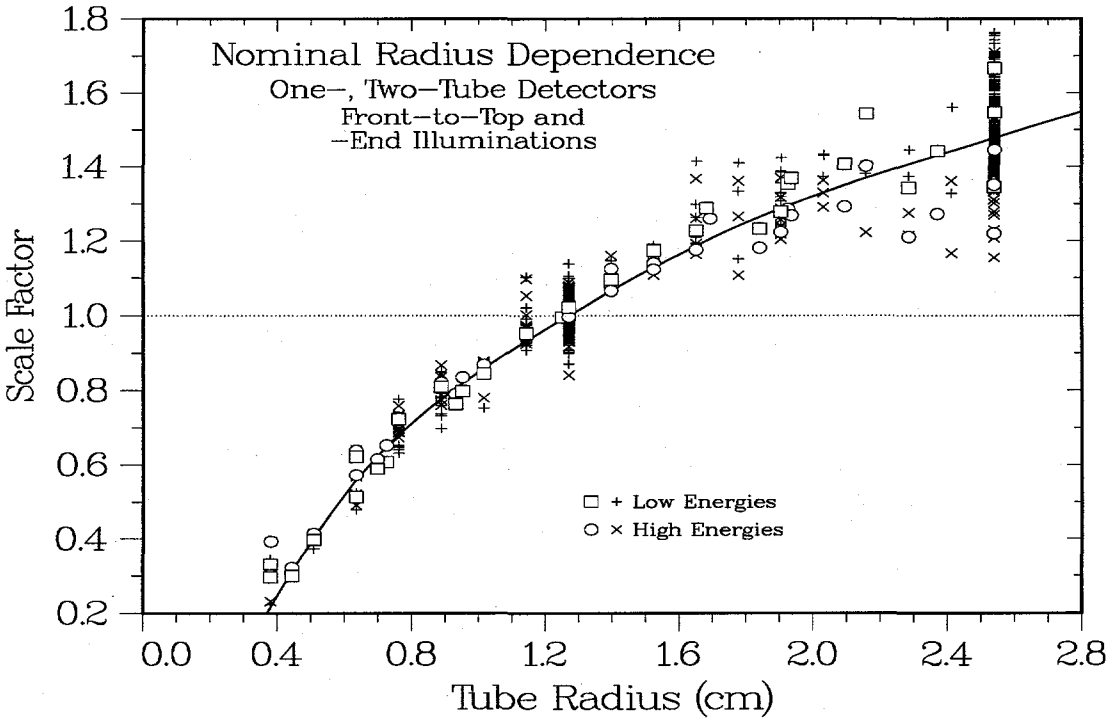

Figure 7.3. Combined radius dependence for all detector types.

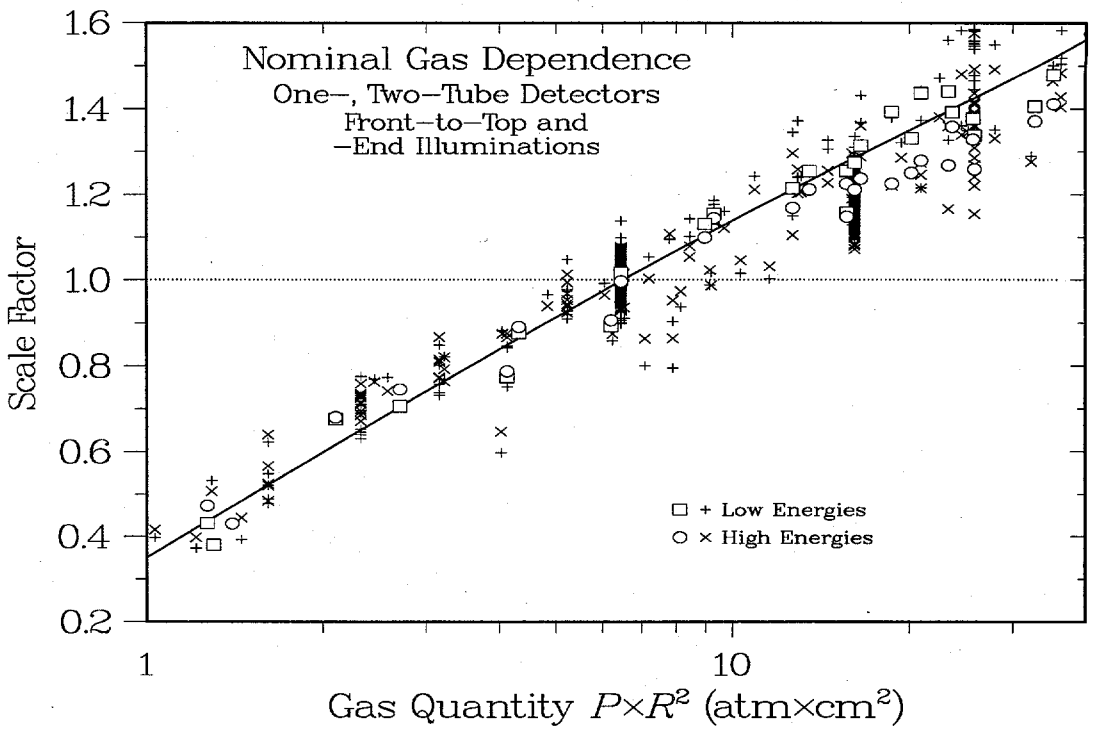

Figure 7.4. Combined gas dependence for all detector types.

Tube Positions. Combining the position dependences from the four different geometry options makes it easier to identify the generic patterns. **Figure 7.5** combines the front/back offset data from Figure 5.6, Figure 5.19, Figure 6.6, and Figure 6.15; **Figure 7.6** combines the tube separation results from the front-to-top scan in Figure 5.7 with the corresponding front-to-end data not shown previously in Sec. 5.2. For the front/back offset, the difference between the data for the front side of the detector at low and high energies was ignored in the averaging, but the clearer separation dependence has provided a clear decrease in the efficiency for tubes whose centers are either more or less than 5.5 cm apart.

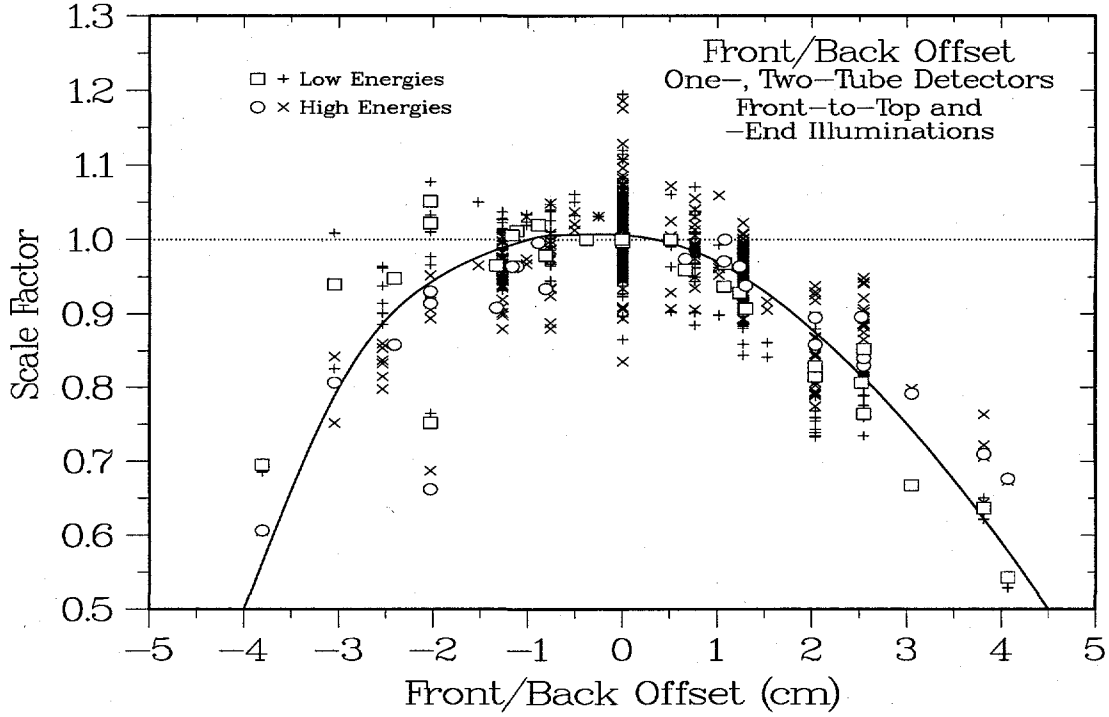

Figure 7.5. Combined dependence on tube offset for all detector types.

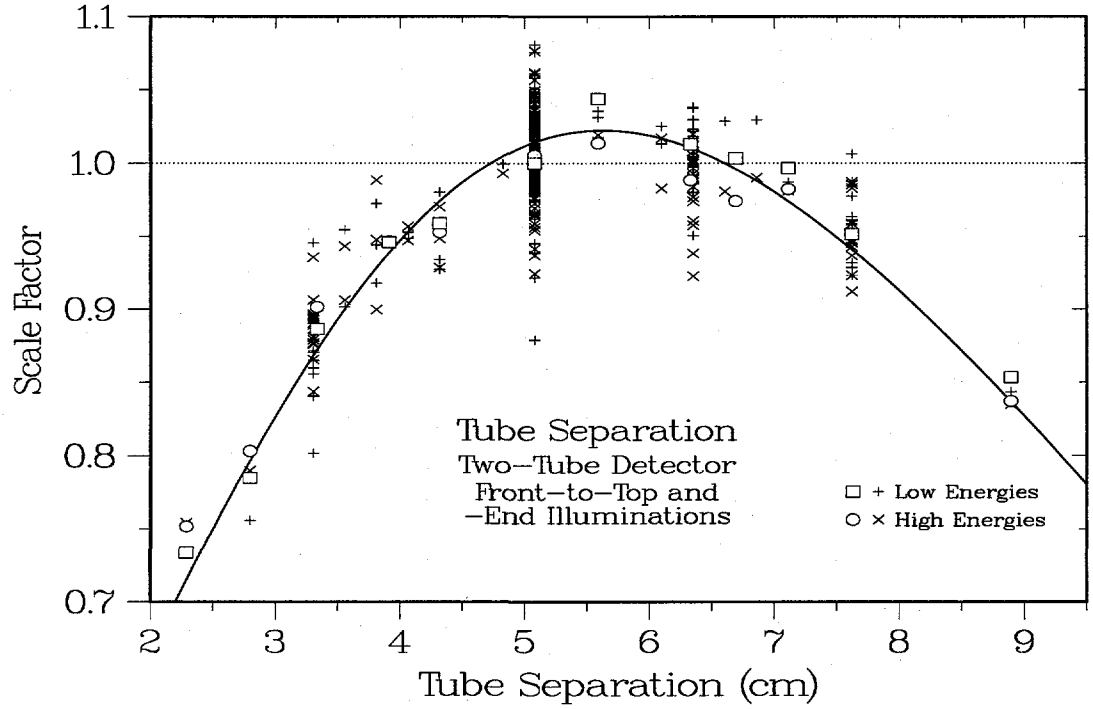

Figure 7.6. Combined dependence on tube separation for all two-tube detector types.

Slope Dependence. The combined results for the aspect dependence in **Figure 7.7** make it clear that all detector geometries show similar behavior at both low and high energies.

In cases where the detector's height or length exceeds its thickness, the aspect ratio is positive and the distribution slope is negative; that is, the additional material in the 90° direction reduces the effective area at back angles. In the few runs with thicknesses that exceed the 90° dimension, the distribution slope switches to slightly positive. For the offset dependence in **Figure 7.8**, however, there is a clear effect only for the low-energy data. Moving the tubes toward the front of the detector raises the forward-angle effective areas, which causes the slope to turn more negative. Moving the tubes toward the rear decreases the forward-angle results and has the opposite effect on the slope.

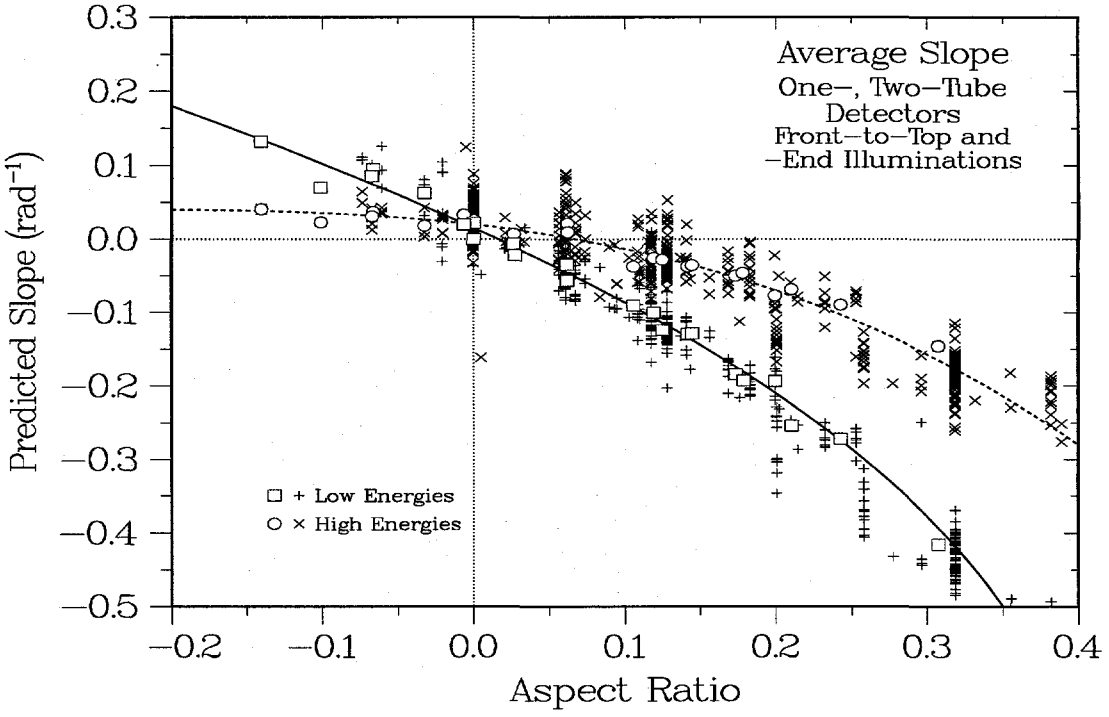

Figure 7.7. Average dependence of the predicted slope on the asymmetry of the detector about the front-to-top and front-to-end axes.

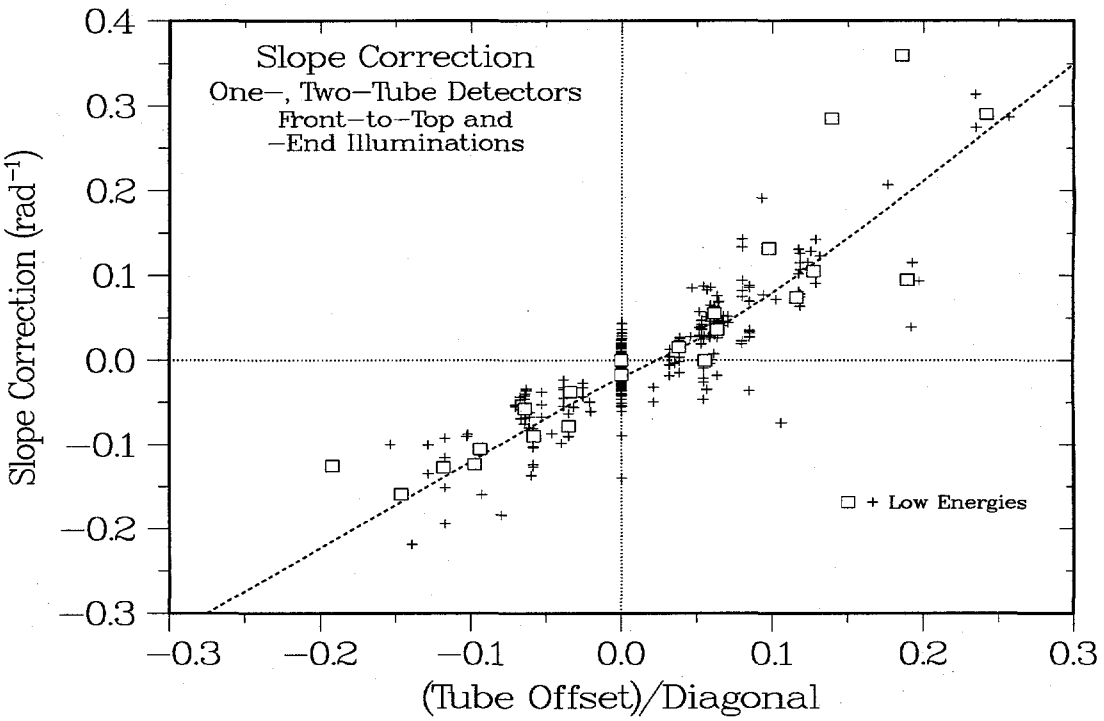

Figure 7.8. Dependence of the low-energy slopes on the ratio between the horizontal tube offset and the relevant detector diagonal.

Generic Model Predictions. Next, the parameter dependences in Figure 7.1 through Figure 7.6 were used to predict the effective areas and distribution slopes for each of the four geometry databases. The results for the effective areas are shown in **Figure 7.9**, and those for the slopes are given in **Figure 7.10**. In both cases the agreement between the actual and predicted values is quite good. To illustrate the quality of agreement, in **Figure 7.11** we show the results of an end-to-end test of the generic model. The data points are the original MCNP results from two extreme cases, one for an almost symmetric detector and the other for a highly asymmetric one. The × symbols are the average effective areas predicted by the generic model; the lines are the angular distributions resulting from the slope information. Clearly, our simple model does a good job of reproducing both the magnitudes and the slopes of the distributions at the two energies. Accordingly, we can assert that the simple formalism described here appears to be sufficient to describe the magnitudes and shapes of the effective areas for one- and two-tube detectors over a wide range of illumination angles and detector geometries.

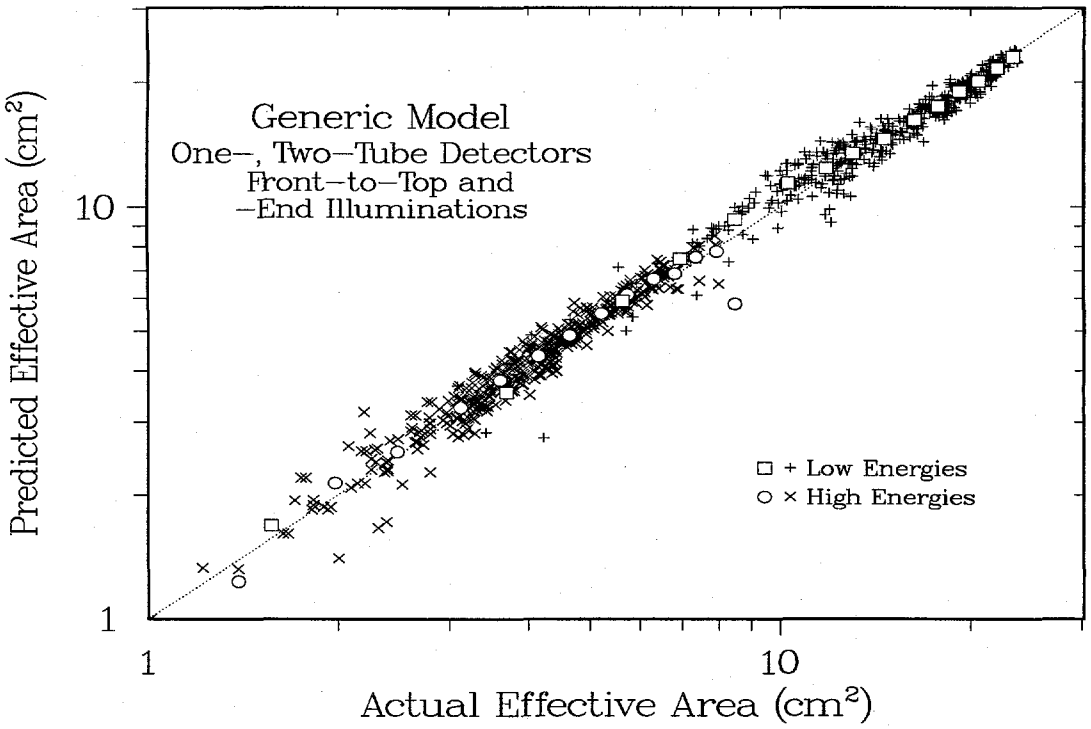

Figure 7.9. Ability of the generic model to reproduce the effective areas at low and high energies for all detectors.

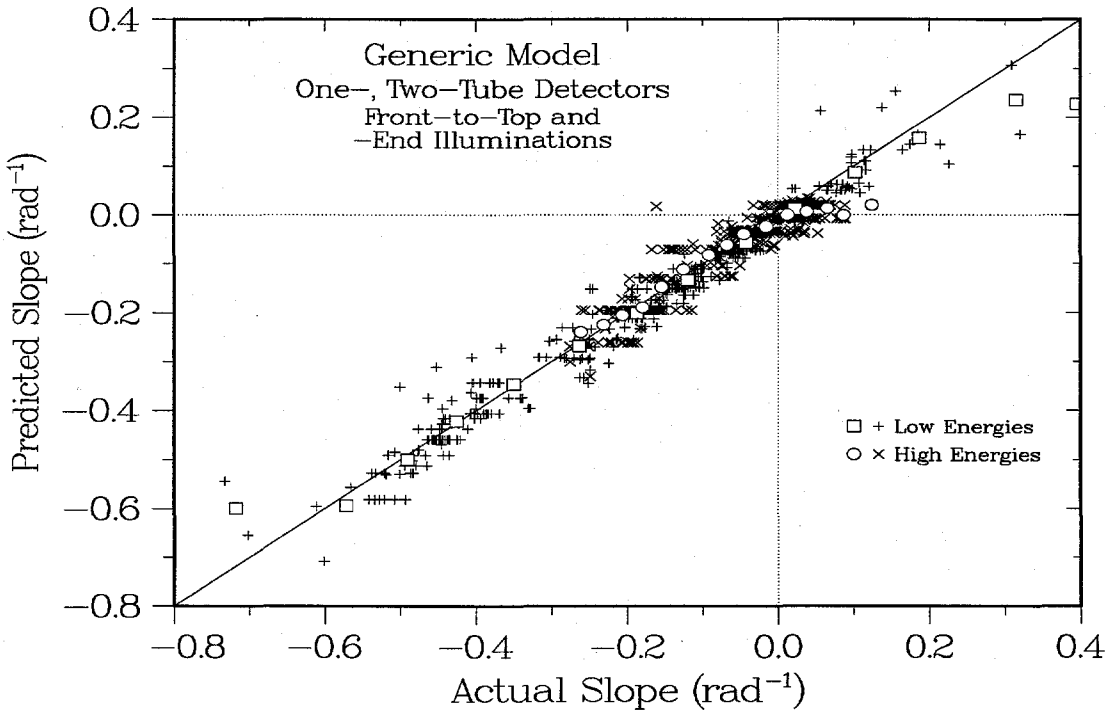

Figure 7.10. Ability of the generic model to reproduce the slopes for all detectors at low and high energies.

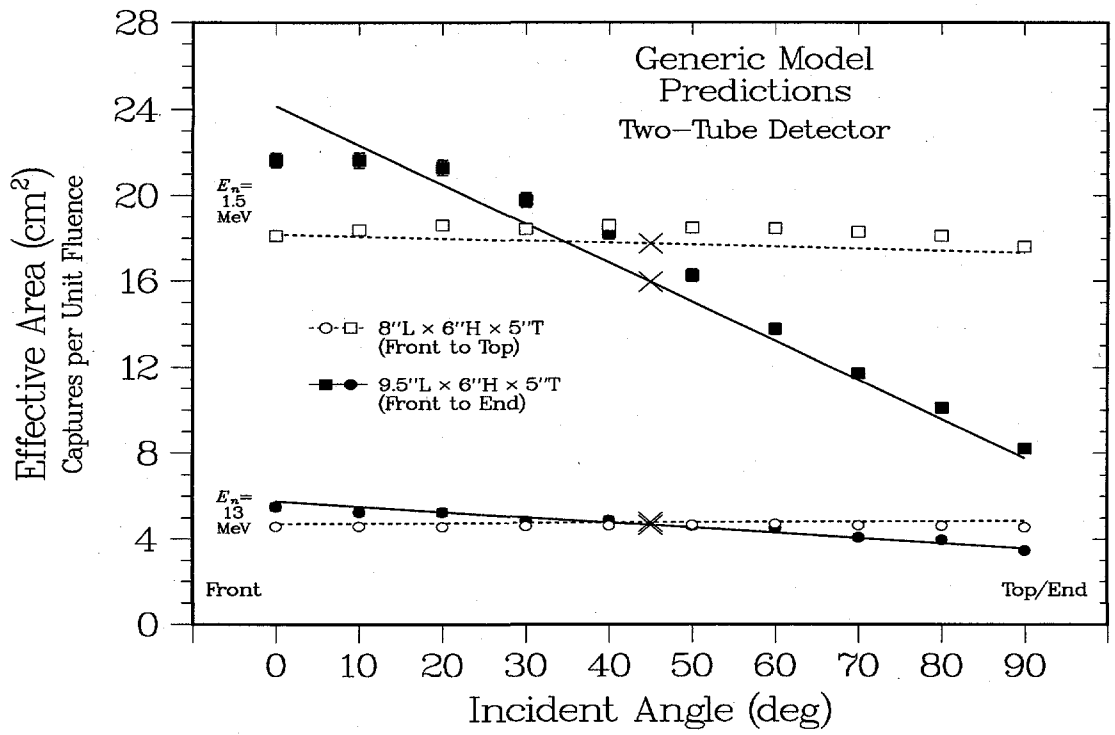

Figure 7.11. End-to-end consistency check to illustrate the generic model's ability to reproduce the original MCNP results.

7.2. Energy Dependence

Model. Thus far, the discussions in this report have emphasized the angular dependence of the effective area, not its energy dependence. Instead of focusing on the slopes of the angular distributions, we could have carried out a corresponding analysis for the slopes of the energy dependences. In our situation, however, the detector response probably involves a wide range of angles but only a few selected energies, which we have represented by the two energy ranges 1–2 and 12–14 MeV. In retrospect, however, we can use our large database to provide some information about the effect of geometry changes at these two representative energies. Only three parameters in the effective-area models in Chaps. 5 and 6 are noticeably energy dependent: the plastic mass, the tube radius, and the front/back offset. In **Figure 7.12** we show the mass dependence of the ratios between the areas at low and high energies. As the mass increases, the areas at both low and high energies also increase, as shown in Figure 5.2 and Figure 5.15. However, the rate of increase is greater at high energies, which causes the ratios in Figure 7.12 to decrease with increasing detector mass. **Figure 7.13** shows the corresponding analysis for the radius dependence. As the radius increases, the efficiency increases more rapidly at low than at high energies (see Figure 5.4), so the ratio between the low- and high-energy values increases with increasing radius, just as shown here. Physically, increasing the tube radius decreases the amount of moderator, which decreases the efficiency. Although most of this effect is captured in the mass dependence, there remains a small residual radius effect. Next, **Figure 7.14** shows the offset results. At high energies the dependence is determined mainly by diffusion out of the moderator, which is almost front-to-back symmetric. Moving the tubes toward the front of the detector is therefore more affected by the low-energy dependence, which is enhanced toward the source side of the detector (see Figure 5.6). The result is a low-to-high ratio that increases toward the front of the detector, just as

seen in the figure here. Thus, improving the high-energy efficiency (lowering the ratio) requires increasing the mass, decreasing the tube radius, or moving the tubes toward the back of the detector. Because the last two changes would decrease the overall effective area, they would also require an increase in the detector mass in order to maintain the same efficiency.

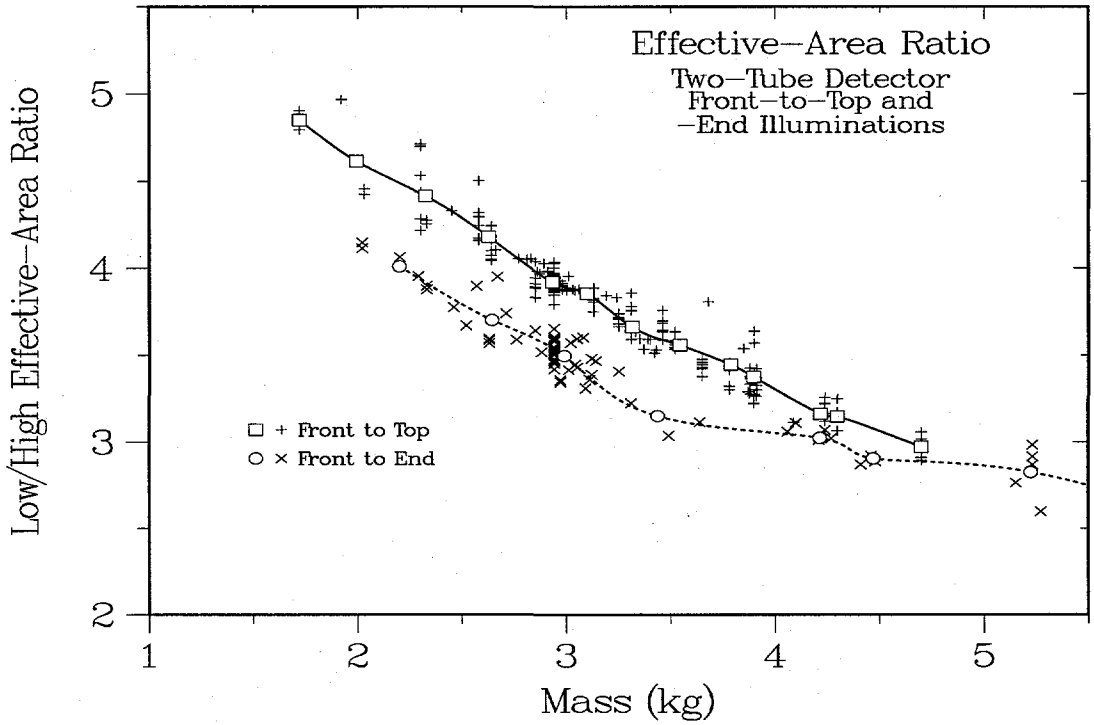

Figure 7.12. Ratio between the low-energy and high-energy effective areas for two-tube detectors as a function of mass.

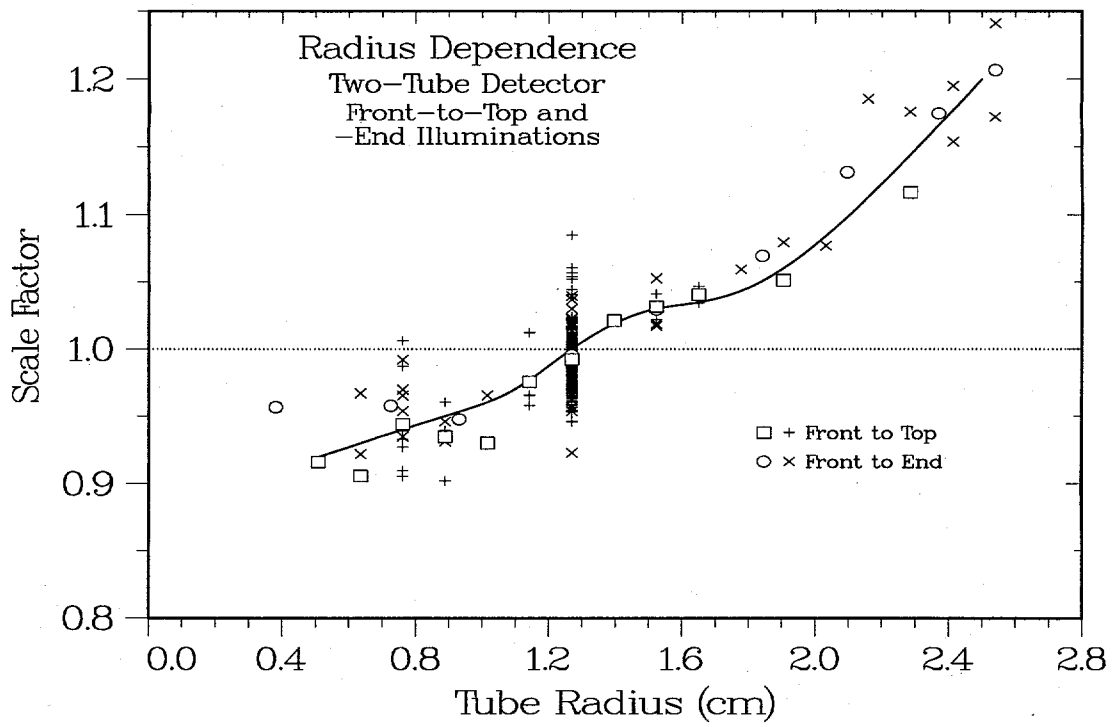

Figure 7.13. Radius-dependent correction to the ratio between the effective areas at low and high energies.

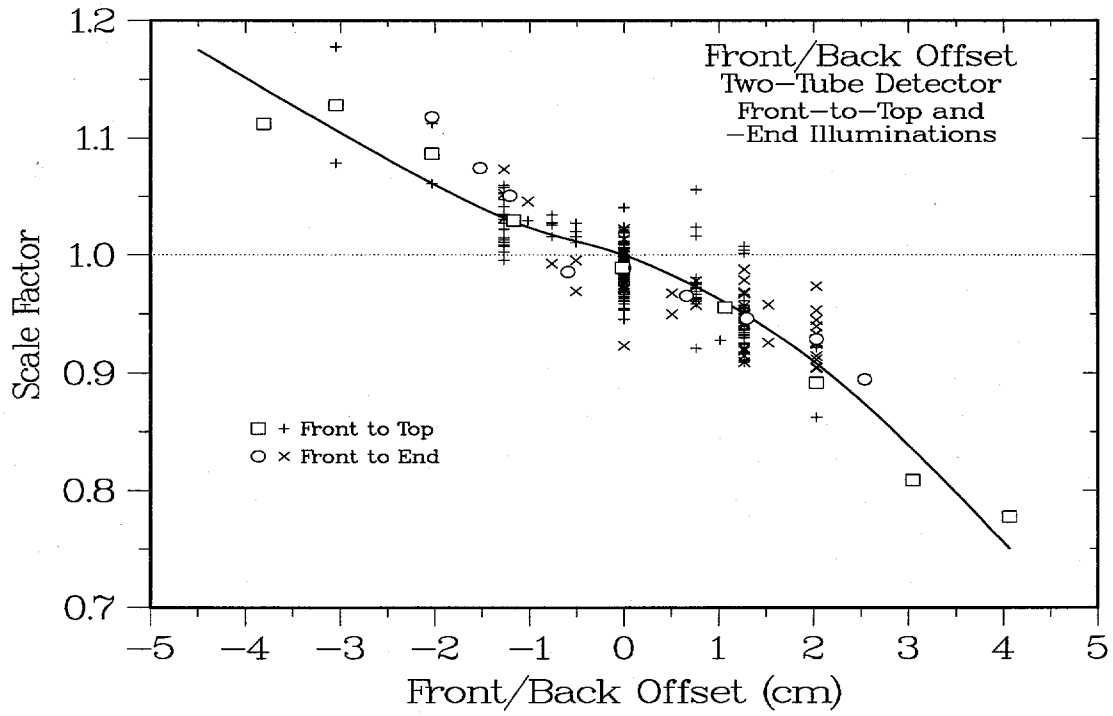

Figure 7.14. Offset dependence in the ratio between the effective areas at low and high energies.

7.3. Discussion

Results. As stated at the outset, all data points for the averages and individual runs shown in this chapter are the same as those from earlier chapters; only the interpolation curves have been changed. Except for the slightly different energies for the onset of saturation in the mass dependence, it appears that the two-tube and one-tube analyses can be described quite well by a single common model. In fact, the additional data has made it easier to draw smooth spline curves through the parameters, which has made it simpler to identify the most important trends. Although our focus in this report has been on the angular dependence of the effective area, our results show that the energy dependence could also be described by a simple analytical model. When combined with the analyzing-power results in Sec. 5.3, we can state that such models can provide simple descriptions of essentially all the important characteristics of moderated ^{3}He detectors over a wide range of energies and angles.

8. OPTIMIZATION

Overview. As stated in Chap. 1, the major criteria for a field instrument are usually high reliability and maximum efficiency per unit mass. The first issue typically means using a conservative design, which provides little guidance for choosing optimum parameter values in the proposed case. For obtaining maximum efficiency per unit mass, however, we can identify four classes of parameters:

(1) Some parameters change the effective area but not the detector mass. In our analyses an obvious case is the gas pressure, but other examples are the tubes' front/back offset and the two-tube separation. Raising the gas pressure will affect the detector resolution, the timing and pileup characteristics, and the specifications for the high-voltage supplies, all topics that are beyond the scope of this report. The other geometrical issues are addressed in Sec. 8.1.

(2) Other parameters have no effect on the effective area but may change its angular dependence, such as the detector dimensions. Within the constraints imposed by the available space, we would generally choose a more uniform response and hence a more symmetric geometry, so these issues need no further consideration.

(3) Finally, there is the explicit mass dependence itself. Because there are slightly different mass dependences for low versus high energies, front-to-top versus front-to-end source rotations, and one- versus two-tube detectors, some decision must be made about the relative importance of different situations. We have chosen to combine the results for both source rotations with equal weighting and the results for high and low energies with a 2:1 weighting. The resulting mass dependences are discussed in Sec. 8.2.

A summary and the final energy-dependent effective areas are given in Sec. 8.3.

8.1. Geometry Factors

Tube Positions. The spline curves for the two source rotations do not behave very differently for the front/back offsets (in Figure 5.6, Figure 5.19, Figure 6.6, Figure 6.15, and Figure 7.5) or the tube separations (in Figure 5.7 and Figure 7.6). However, inspection of the offset results in Figure 5.6 and Figure 6.6 shows a clear difference between the values at high and low energies, with the latter being consistently shifted toward the front of the detector. As shown in **Figure 8.1**, this shift survives in the energy-averaged values, despite the considerable straggling created by the combination of data from different geometries. Within these uncertainties, we can only recommend that the optimum tube position should be shifted very slightly (0.5 cm) toward the front of the detector. Similar straggling exists for the two-tube separations in **Figure 8.2**; here we suggest that an optimum center-to-center distance might be about 5.5 cm. Clearly, however, changes in either of these positions by about ±1 cm correspond to a change in efficiency of 5% or less, so neither of these recommendations is critical for maximizing the count rate. Similarly, Figure 7.8 shows that 10% shifts in the tube offset have an almost negligible effect on the slope of the angular distribution, and Figure 7.14 shows that there is little effect on the energy dependence over the MeV range of interest.

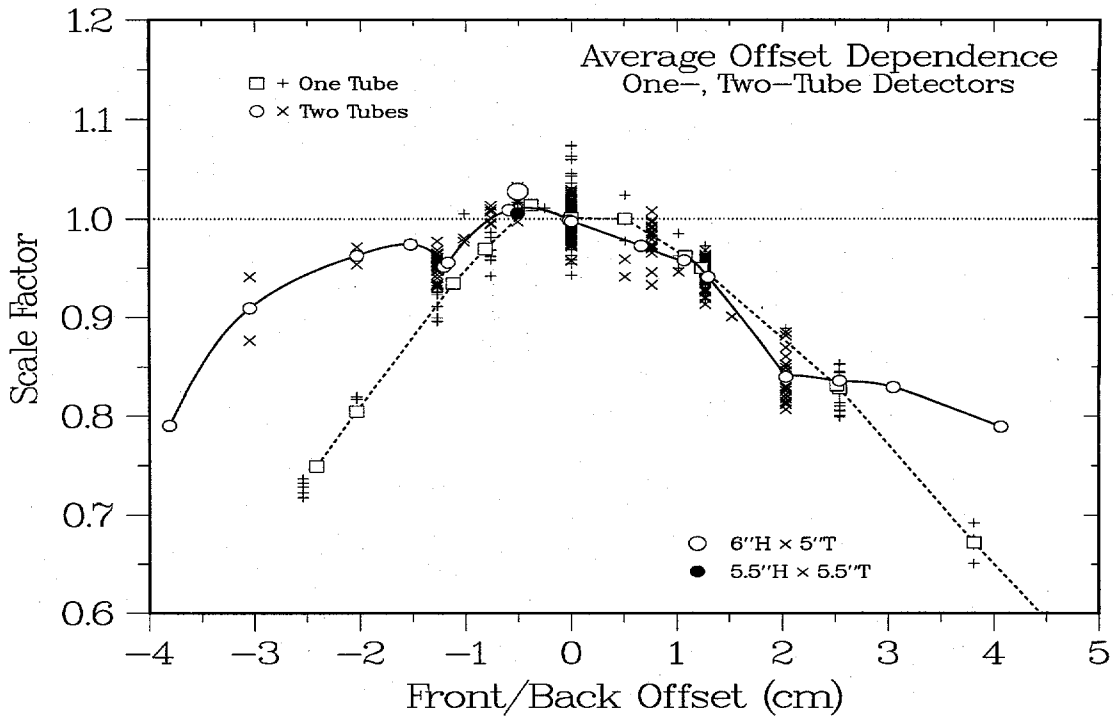

Figure 8.1. One- and two-tube results of averaging the front/back tube offsets over incident direction and energy.

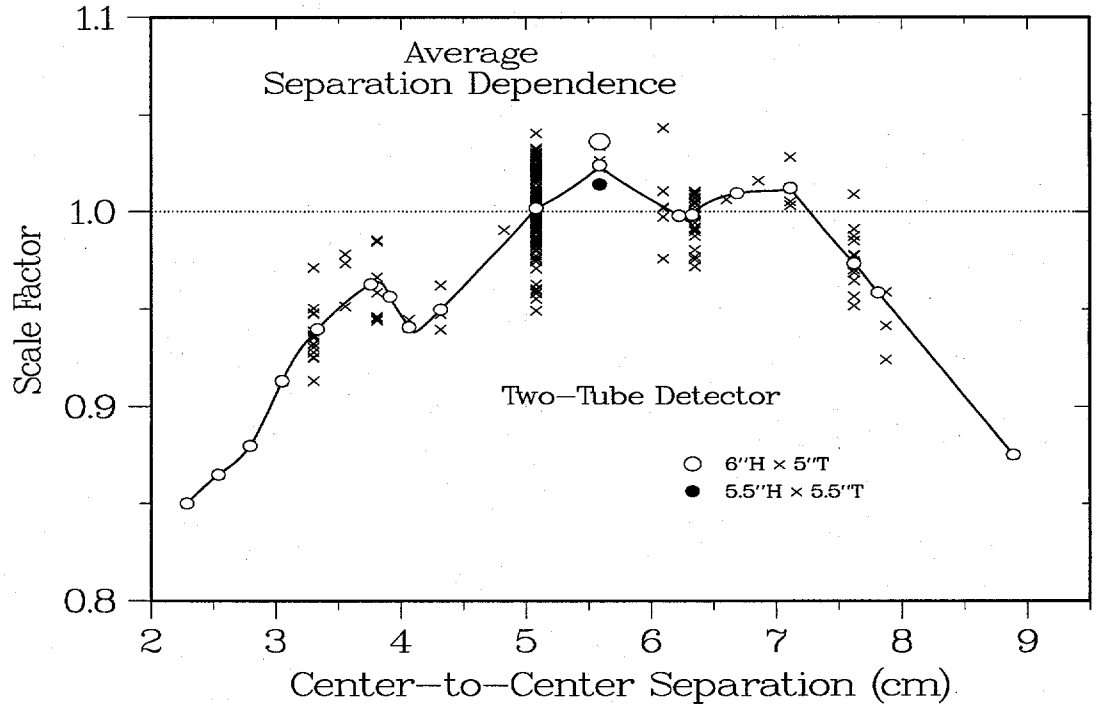

Figure 8.2. As in Figure 8.1, average results for the optimum tube separation in a two-tube detector.

8.2. Mass Dependence

Effective Area versus Mass. We have developed two approaches to determining the optimum plastic (polyethylene+scintillator) detector mass. As stated in Chap. 2, the proposed detector should have an effective area at least as large as that of the existing detector (see Table 2.1.) The present values for the effective areas of all possible detector configurations are shown in Figure 7.1; the weighted averages for one- and two-tube detectors are shown in **Figure 8.3** and listed in **Table 8.1**. Because the one-tube data must be increased by 64% to match the two-tube results, it is clear that the added capture probability for the two-tube arrangement is more efficient. Further, although some of the increased effective area of our proposed detector is associated with its 10% greater mass, the improvement in effective area is closer to 20%, which implies that some of the improvement results from better mass utilization.

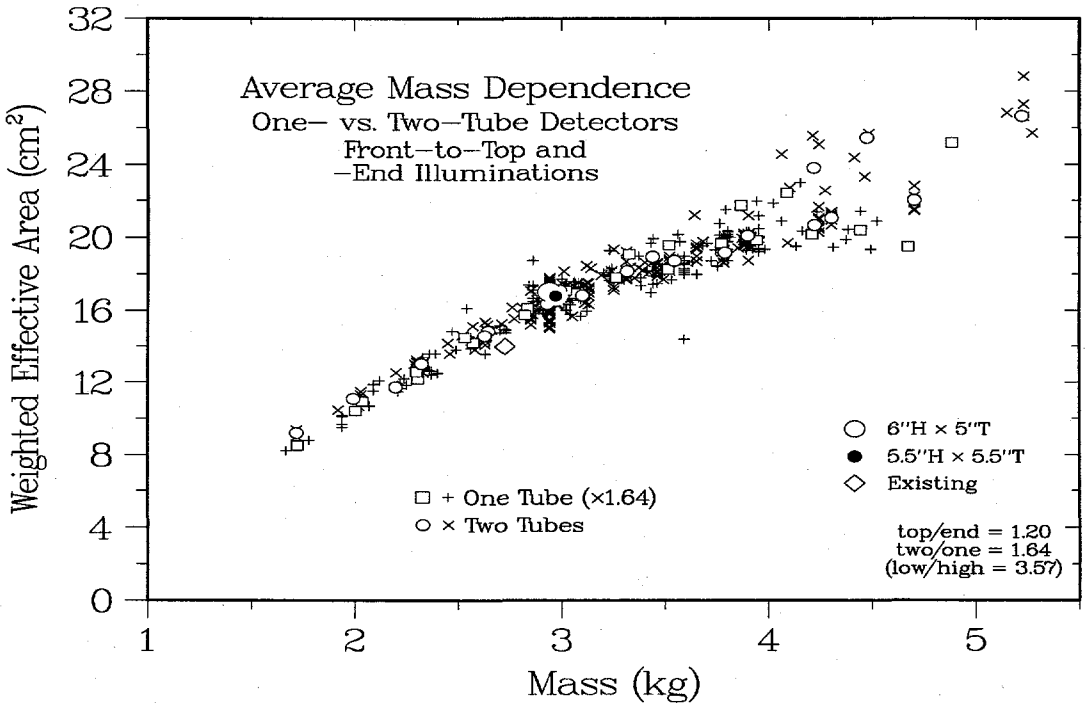

Figure 8.3. Effective-area calculations for one- and two-tube detectors obtained from a weighted average of the values in Figure 7.1.

Table 8.1. Mean Effective Areas

2-Tube		1-Tube	
Mass (kg)	Area (cm^2)	Mass (kg)	Area (cm^2)
1.72	9.19	1.73	5.18
1.99	11.10	2.01	6.35
2.20	11.74	2.04	6.67
2.32	13.02	2.30	7.66
2.63	14.58	2.31	7.42
2.64	14.84	2.53	8.83
2.93	16.34	2.57	8.66
2.99	17.08	2.82	9.60
3.10	16.81	2.83	9.82
3.31	18.15	3.02	10.41
3.44	18.93	3.06	10.30
3.54	18.72	3.26	10.85
3.79	19.15	3.32	11.62
3.90	20.09	3.51	11.13
4.22	23.81	3.52	11.92
4.22	20.67	3.77	11.97
4.30	21.07	3.87	13.24
4.47	25.45	3.94	12.09
4.70	22.02	4.09	13.66
5.22	26.64	4.28	12.29
		4.44	12.43
		4.67	11.87
		4.88	15.35

Figure-of-Merit Values. The performance data in Figure 8.3 tell us whether the proposed detector meets the performance goals set by the existing instrument, but they do not tell us how efficiently we are using the available plastic mass. Apparently, this efficiency is higher for the proposed detector than the existing one, but what determines the optimum value? We can address this question by calculating the effective area per unit mass, which provides a figure of merit (FOM) for comparing different detector configurations. The results for two- and one-tube detectors are given in **Figure 8.4** and **Figure 8.5**, respectively. As expected, low-energy FOM values are larger than those at high energies; two-tube results are higher than those for one-tube detectors; and front-to-top rotations are higher than front-to-end cases. The low-energy FOM values peak at masses of 2–3 kg, while the high-energy values peak at 3–5 kg; the front-to-top values also peak at lower energies than the front-to-end results. Remember that the proposed energy averaging includes 2:1 weighting for high versus low energies, and note that the front-to-top and front-to-end averaging effectively counts forward angles twice as heavily as the top or end cases. As shown by the results in **Table 8.2** and **Figure 8.6**, many of the differences within the separate one- and two-tube data sets cancel out in the averaged results. For both detector designs, there is a clear maximum at 3.0±0.5 kg. Thus, for most efficient use of the available plastic, the mass should be within this range.

Note that the FOM values for the proposed detector are 10% higher than those for the existing one, which accounts for the overall 20% gain in effective area.

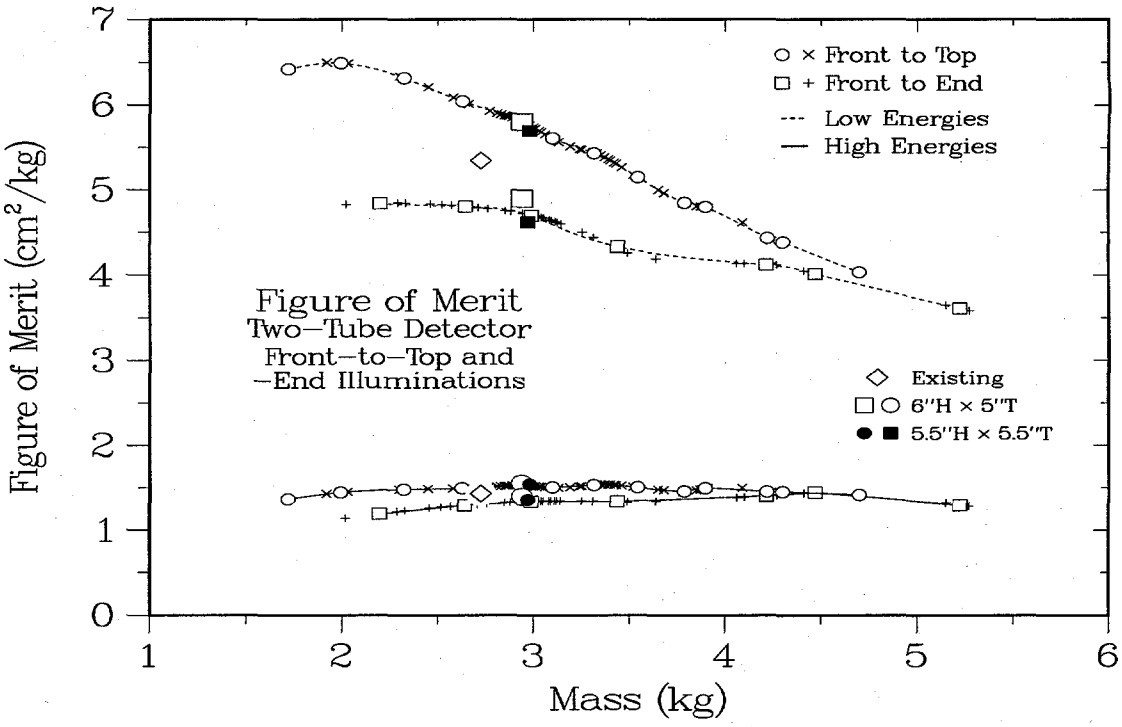

Figure 8.4. Figure-of-merit (FOM) calculations for each of the four sets of runs for the two-tube detector.

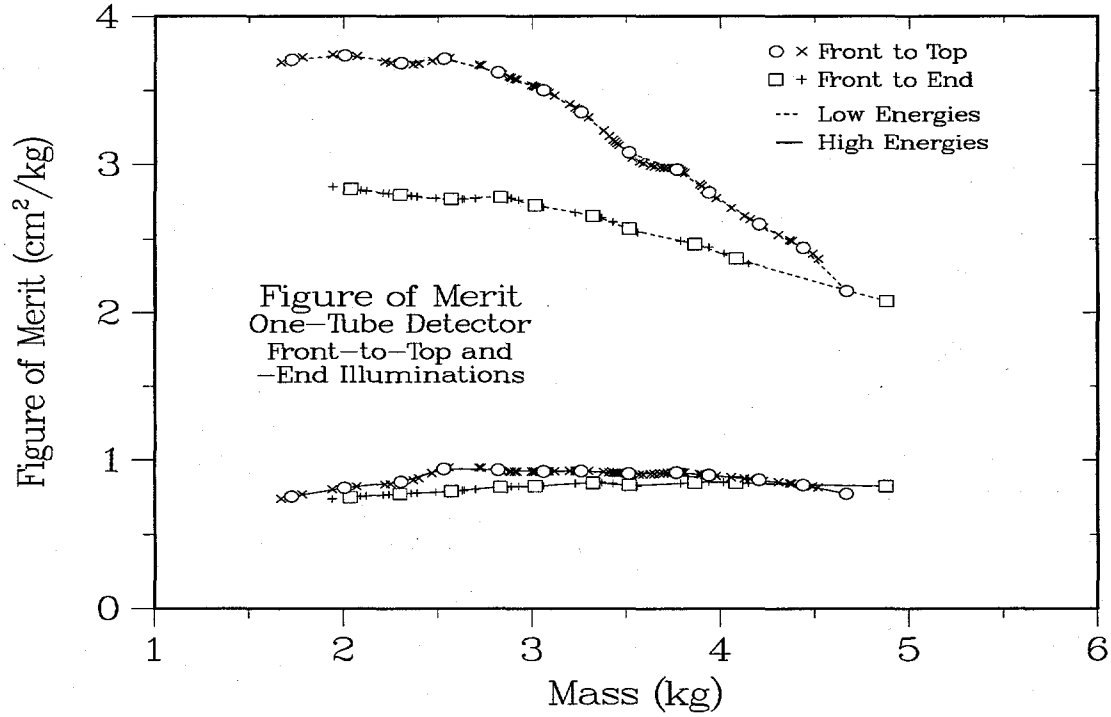

Figure 8.5. FOM calculations as in Figure 8.4, but for the one-tube detector.

Table 8.2. Figure-of-Merit Values

2-Tube		1-Tube	
Mass (kg)	FOM (cm^2/kg)	Mass (kg)	FOM (cm^2/kg)
1.72	1.88	1.73	1.13
1.99	1.96	2.01	1.17
2.20	1.98	2.04	1.17
2.32	2.00	2.30	1.20
2.63	2.03	2.31	1.20
2.64	2.03	2.57	1.24
2.93	2.05	2.53	1.24
2.99	2.04	2.82	1.25
3.10	2.02	2.83	1.25
3.31	2.01	3.02	1.24
3.44	1.99	3.06	1.24
3.54	1.97	3.26	1.24
3.79	1.94	3.32	1.23
3.90	1.96	3.51	1.20
4.22	1.92	3.52	1.20
4.22	1.92	3.77	1.20
4.30	1.92	3.87	1.19
4.47	1.91	3.94	1.17
4.70	1.85	4.09	1.15
5.22	1.73	4.21	1.13
		4.44	1.10
		4.67	1.04
		4.88	0.98

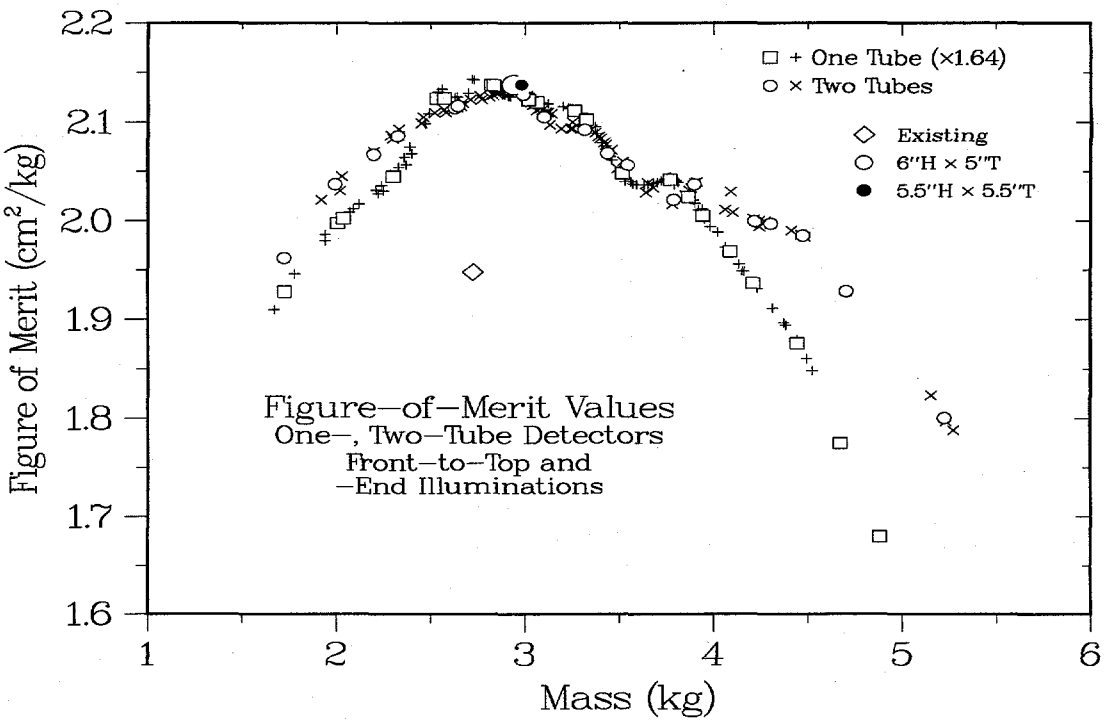

Figure 8.6. FOM summaries obtained from a weighted combination of low- and high-energy values for the one- and two-tube detectors in Figure 8.4 and Figure 8.5.

8.3. Final Results

Energy Distribution. One of the clearest ways to compare the performances of the existing and proposed systems is to overlay the energy profiles of the effective areas. Accordingly, in **Figure 8.7** and **Figure 8.8** we show the results of calculations that average the proposed detector's effective area over all incident directions by providing uniform illumination with a unit fluence of 1 n/cm^2. Three sets of calculations are shown. First, the solid circles are values from the MCNP4A code, which was used throughout this report to ensure consistency with the previous analysis discussed in Chap. 2. These data are also tabulated in **Table 8.3**. Next, the open circles show the corresponding results calculated with the current MCNP4B code and the libraries obtained from the Radiation Safety Information Computational Center (RSICC).* In our application there appears to be no significant difference between the two sets of results. Finally, when compared with the intermediate values for the existing detector (Figure 2.7, Figure 2.8, and Table 2.1), the results at MeV energies are completely consistent if the previous calculations are increased by 20%. There are differences for the shorter mean free paths at lower energies, but these effects are associated mainly with unimportant differences in geometry.

* RSICC, P.O. Box 2008, Oak Ridge, TN 37831-6362.

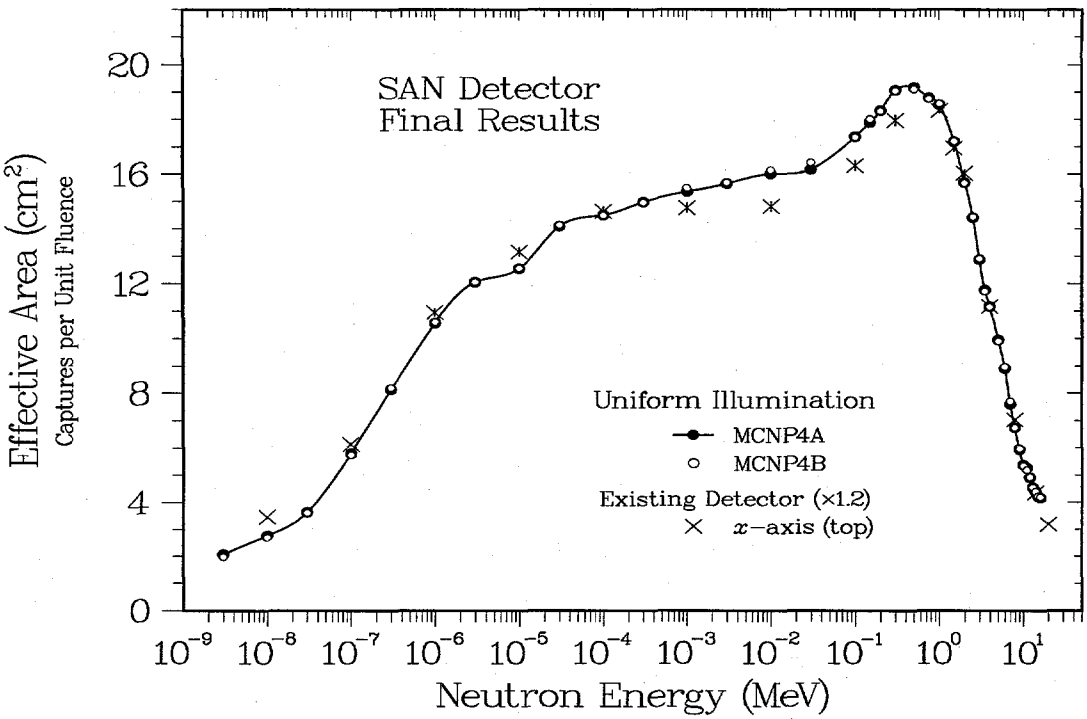

Figure 8.7. Energy-dependent effective areas for the final detector design, averaged over all incident directions. See Figure 2.7 for the corresponding values for the existing detector.

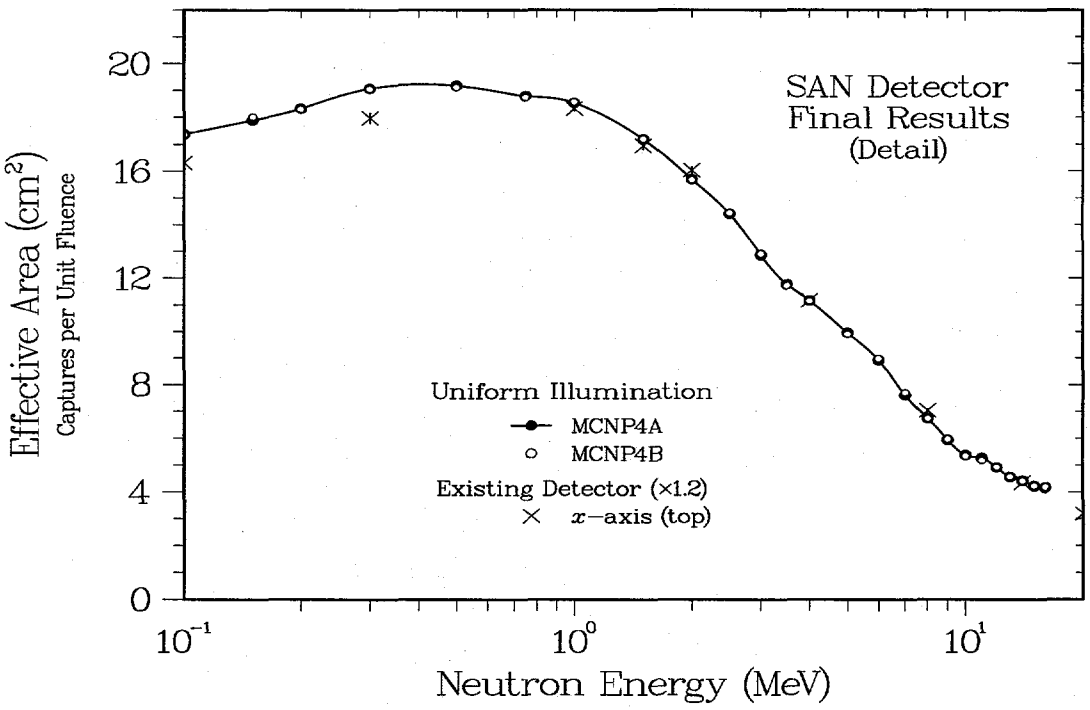

Figure 8.8. Detail of Figure 8.7 for the energy range of greatest interest. See Figure 2.8 for comparison with the existing detector.

Table 8.3. Final Effective Areas for Uniform Illumination

Energy (MeV)	A_{eff} (cm^2)	Uncertainty (percent)
16.0	4.19	0.55
15.0	4.22	0.55
14.0	4.40	0.54
13.0	4.55	0.53
12.0	4.93	0.51
11.0	5.19	0.49
10.0	5.34	0.48
9.00	5.96	0.46
8.00	6.74	0.44
7.00	7.71	0.41
6.00	8.97	0.38
5.00	9.90	0.36
4.00	11.16	0.34
3.50	11.73	0.33
3.00	12.91	0.32
2.50	14.44	0.30
2.00	15.67	0.29
1.50	17.20	0.27
1.00	18.57	0.26
0.75	18.75	0.26
0.50	19.11	0.26
0.30	19.05	0.26
0.20	18.30	0.26
0.15	18.01	0.27
0.10	17.35	0.27
0.03	16.42	0.37
0.01	16.14	0.39
3E–3	15.70	0.40
1E–3	15.49	0.40
3E–4	14.96	0.40
1E–4	14.49	0.41
3E–5	14.13	0.41
1E–5	12.56	0.43
3E–6	12.05	0.44
1E–6	10.60	0.46
3E–7	8.19	0.52
1E–7	5.76	0.61
3E–8	3.61	0.75
1E–8	2.70	0.86
3E–9	1.98	0.99

8.4. Discussion

Results. With the background provided by the analyses in previous chapters, evaluating the effects of tradeoffs in detector geometry and mass is relatively straightforward.

- *Averaging.* The only additional analysis required in this chapter was constructing the weighted averages for the different source directions and energies and for the one- and two-tube geometries. For the source direction, this averaging gives approximately equal 2:1 weighting to the front and end responses. For the source energies, the 2:1 weighting of high and low energies approximately compensates for the unavoidable decrease in efficiency toward higher energies.
- *Tube Positions.* For the tube offsets and separations, the averaging over geometry creates some irregular structure in the results, but the conclusions are essentially the same as those for the separate analyses. For high energies, the symmetry of neutron diffusion out of the moderator favors placing the tubes in the center of the detector; at lower energies, attenuation shifts the optimum offset toward the front of the detector. The weighted distribution is therefore shifted about 0.5 cm toward the incident surface. For the two-tube separation distance, the consensus for different source and detector parameters gives a center-to-center distance of about 5.5 cm; note that this analysis includes several different tube radii.
- *Mass Dependence.* Most of our discussion, however, concerns the mass optimization. We presented two types of information as functions of increasing mass: the energy- and

angle-averaged effective area and the derivative of this function, the effective area per unit mass. The latter quantity indicates that the most efficient use of plastic mass occurs for polyethylene-plus-scintillator values at 3.0±0.5 kg and that the proposed designs are about 10% more efficient than the existing detector, which has a mass of about 2.7 kg. As a result, our proposed design, with a plastic mass just below 3.0 kg, should have an effective area about 20% greater than that of the existing system at the MeV-range energies of interest. Finally, comparisons of effective areas calculated using the MCNP4A code, our previous standard, and MCNP4B, the current version, indicate that there are no significant differences for our application.

9. SUMMARY AND CONCLUSIONS

Objectives and Previous Work. Despite the obvious importance of optimizing the performance of fast-neutron detectors for applications in arms control or space exploration, few such studies exist in the literature, and those that are available are not generally useful for other applications. For example, our previous studies focused on a specific satellite-based polyethylene-moderated ^{3}He detector, yet the results are scarcely applicable to the present problem of designing a possible replacement. Nevertheless, several of the concepts from our previous reports have been very useful in organizing the present study. In particular, the replacement of detection efficiency and projected area with the area-efficiency product, or effective area, has been absolutely central to the analyses in this report. To a lesser degree, it was also useful to recognize the division of source directionality into separate topics. On one hand, there exist angle-dependent changes in the overall effective area because of changes in the incident angle; on the other, there are differences between the responses of multiple active elements because of attenuation across the detector. In general, differences in overall angular response are an undesirable feature; however, estimates of the source direction from internal attenuation can provide useful source information.

Monte Carlo Techniques. As a transition between the review of our earlier work and the development of a new analysis approach, we have summarized the energy and angle dependence of the effective areas for several examples of the proposed detector. When combined with the previous studies, these examples reiterate the need for a comprehensive model to connect changes in detector parameters with changes in the resulting effective area. Our approach has two major components: (1) the construction of an extensive database that includes the effects of changes in all relevant detector parameters, and (2) the development of an analytical model that allows us to understand the effect of each parameter separately. The model's crucial assumption, that the effective area and its angular dependence can be simply related to geometry aspects such as detector size and shape, is a direct result of our emphasis on effective area as the central determinant of detector performance.

Modeling Results for Different Detectors. Carrying out the analyses for different detector configurations occupies several chapters in our report. The initial divisions were between two-tube and one-tube detectors, between the magnitude and slope of the effective area, and between front-to-top and front-to-end source illumination. The parameters to be varied were the total plastic (polyethylene+scintillator) mass; the detector height, thickness, and length; and the tube radius, pressure, and position. Some of these parameters are deliberately redundant, as with the mass and the detector volume; others can be combined to give fewer parameters, as in replacing the tube radius and pressure with the quantity of ^{3}He gas. Once these databases were complete and their general behavior was understood, we combined the results of the separate analyses to provide a global view of the parameter dependences. This synthesis culminated in a generic detector model with explicitly separable parameters, that is, a product function for the magnitude of the effective area and a sum function for the slope, which are capable of reproducing the energy and angular dependences for all proposed detector configurations. Most of the configurations could be described by using only the detector mass, the gas quantity, the offset of the tubes from the detector center, and the fractional asymmetry in the dimensions of the moderator.

Optimization Results. On the basis of the separable effective-area functions, we were able to quickly determine the few parameters whose values could be varied to optimize the detector response. Because effective area is a geometrical quantity, the principal parameters are also mainly geometrical: detector size (or mass), detector symmetry, gas quantity, and tube position. Although there are slight differences in the behavior of these parameters for different detector configurations, the average dependences are fairly simple. In particular, evaluating the effect of different detector sizes is straightforward when the size effects are expressed as the mass dependence of the effective area and the effective area per unit mass. For our final choice of parameters, the proposed design provides about 20% greater performance than does the existing detector. Half of this increase comes from an increase in mass; the other half comes from improved efficiency.

Related Work. The present report concerns only the neutron response of the SAN instrument. Starting with the final geometry obtained here, a companion report[6] covers the gamma-ray responses of the SAN and SPG detectors. The SAN response to individual gamma rays is particularly linked to the present neutron results, because a proposal exists to use anode-current measurements to extend the SAN dynamic range beyond the rates at which dead-time effects make it inadvisable to rely on pulse counting only. Pulse counting, however, has the advantage of generally providing excellent gamma-ray rejection, because the p+t reaction products from the ^{3}He+n capture reaction produce pulses in the gas that are much larger than those produced by the electrons from Compton scattering. Current measurements, unfortunately, include contributions from both neutrons and gamma rays, which must therefore be properly normalized in order to establish their relative signal levels.

ACKNOWLEDGEMENTS

This work has benefited from discussions with Bruce Barraclough on the performance of the existing detector and with David Lawrence on differences between the results from the MCNP4A and MCNP4B codes. Bill Feldman also provided a critical reading of the first draft of the manuscript.

REFERENCES

1. L. V. East and R. B. Walton, "Polyethylene Moderated ^{3}He Neutron Detectors," Nuclear Instruments and Methods **72** (1969) 161–166.
2. A. A. O'Dell, "Calculated and Measured Efficiency of a Man-Portable ^{3}He Neutron Detector," IEEE Transactions on Nuclear Science **NS-24** (1997) 645–646.
3. M. G. Millett and M. E. Nelson, "Weight and Counting Efficiency Optimization in a Moderated Neutron Detection System," Nuclear Instruments and Methods in Physics Research **A417** (1998) 332–341.
4. R. C. Byrd, B. A. Barraclough, W. C. Feldman, and S. J. Bame, "Measurements and Calculations of the Characteristics of a Space-Based Neutron Sensor," Los Alamos National Laboratory report LA-12340-MS (October 1992).
5. R. C. Byrd, J. D. Drabanski, and B. L. Barraclough, "Monte Carlo Calculations of the Effective Area and Directional Response of a Polyethylene-Moderated Neutron Counter," Los Alamos National Laboratory report LA-12850-MS (January 1995).

6. R. C. Byrd, "Calculations of the Response of Shielded Detectors to Gamma Rays at MeV-Range Energies," Los Alamos National Laboratory report LA-13688-MS (March 2000).

7. R. E. Prael and H. Lichtenstein, "User Guide to LCS: the LAHET Code System," Los Alamos National Laboratory document LA-UR-89-3014 (1989).

8. J. F. Briesmeister, Ed., "MCNP—A General Monte Carlo N-Particle Transport Code, Version 4A," Los Alamos National Laboratory report LA-12127-M (August 1991).

9. Y. Uwamino, T. Nakamura, and A. Hara, "Two Types of Multi-Moderator Neutron Spectrometers: Gamma-Ray Insensitive Type and High-Efficiency Type," Nuclear Instruments and Methods **A239** (1985) 299–309.

10. R. C. Byrd and P. A. Russo, "Experimental Tests of a Radiation Direction Finder," Los Alamos National Laboratory report LA-13212-MS (November 1996).